QUANTITATIVE LABEL-FREE INFRARED MICROSCOPY OF LUNG TISSUES FROM RABBIT MODELS OF BRONCHOPULMONARY DYSPLASIA

Ph.D. in Nanoscience

Scuola Normale Superiore Pisa

Academic year 2024/2025

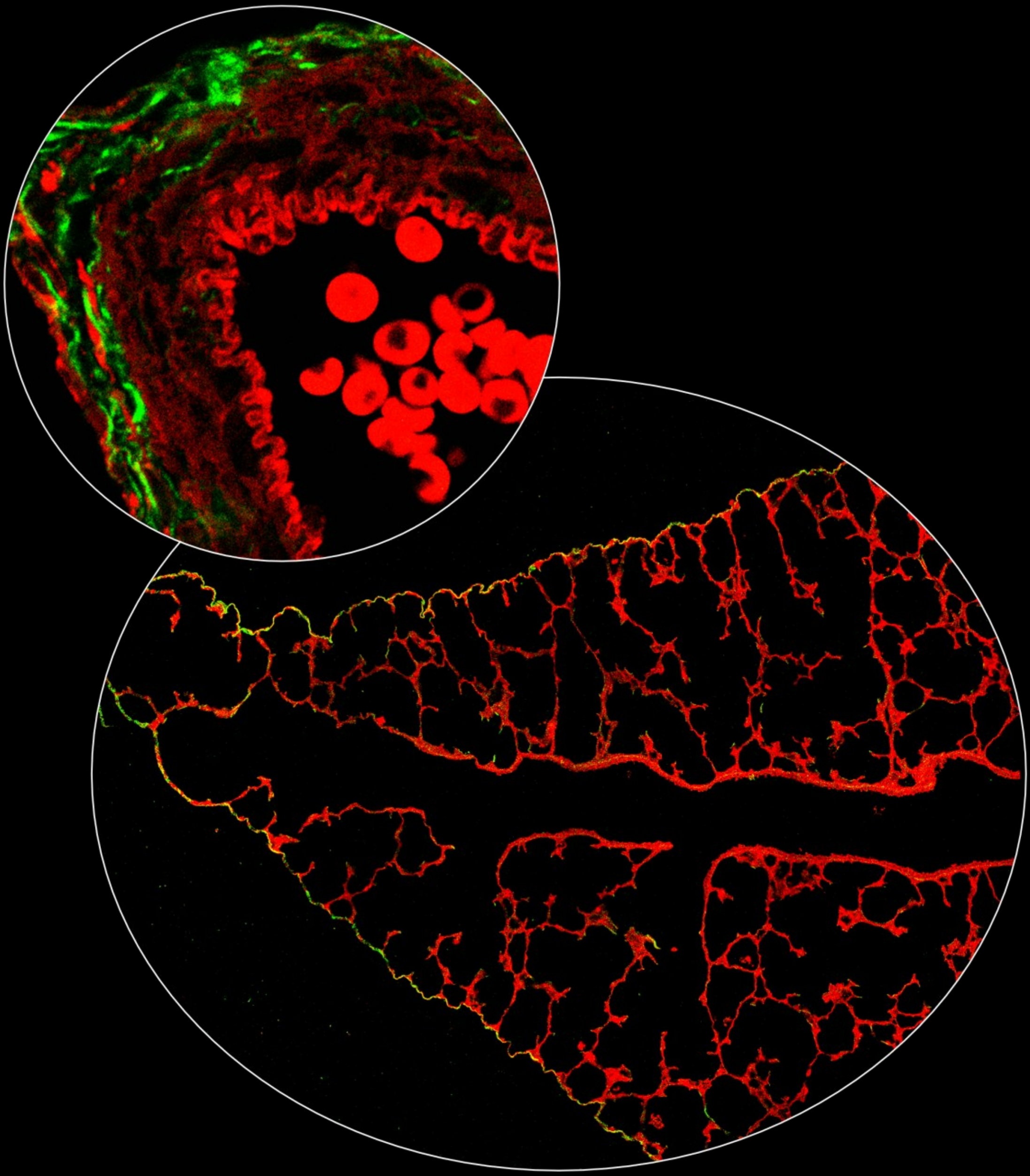

MARGHERITA MARAZZINI

SCUOLA
NORMALE
SUPERIORE

Classe di Scienze

Corso di perfezionamento in
Nanoscienze

XXXVII ciclo

Quantitative label-free infrared microscopy of lung tissues from rabbit models of bronchopulmonary dysplasia

Settore Scientifico Disciplinare **FIS/07**

Candidata
dr.ssa Margherita MARAZZINI

Supervisore interno e relatore	Supervisore Aziendale
Prof. Francesco Cardarelli	Dr.ssa Enrica Scalera

Anno accademico 2024/2025

LIST OF ARTICLES:

Articles included in this thesis:

1. Marazzini, M., Scalera, E., De Meo, S., Ricci, F., Villetti, G., Murgia, X., Zoboli, M., Gazza, F., Ferri, G., Cardarelli, F., Label-free optical fingerprints of hyperoxia-induced lung alterations in preterm rabbits. *Currently under peer review at Respiratory Research.*
2. Marazzini, M., Ferri., G, Dell'Anno MT., Cardarelli, F., A matter of time: a critical re-evaluation of NAD(P)H Metabolic Imaging. *Currently in preparation.*

Articles not included in this thesis:

1. Gómez-Álvarez EM., Marazzini M., Caproni L., Magnani L., Cardarelli F., Dell'Acqua M., Perata P., Pucciariello C., The impact of rainfall regimes on barley seed development underlies genomic variation for germination after flooding. *Accepted for publication in Plant Physiology.*
2. Castellana S., Fioriti F., Marazzini M., Cardarelli F., Loreti E., Perata P., Triozzi PM. Inferring hypoxia-responsive regulators of cell fate in plant meristems through single-cell transcriptomics. *Currently under peer review at Science of Plants.*

Conference contributions:

1. Marazzini M., Scalera E., Ciccimarra R., Villetti G., Ricci F., Murgia X., Cardarelli F., Label-free imaging and lung features screening (LIFES tool)-based characterization of lung parenchymal structures in preterm rabbits exposed to hyperoxia. *EAPS, 17-20 Oct 2024, Vienna, Austria.*
2. Marazzini M., Scalera E., Ciccimarra R., Villetti G., Ricci F., Murgia X., Cardarelli F., Quantitative and label-free infrared microscopy of lung parenchymal tissues from preterm rabbits exposed to hyperoxia. *EMIM, 11-14 Mar 2025, Bilbao, Spain.*

FOREWORD

This work originates from my research conducted at the National Enterprise for nanoScience and nanoTechnology (NEST) laboratory, as part of the PhD program in Nanoscience at the Scuola Normale Superiore of Pisa. My research was fully funded by Chiesi Farmaceutici S.p.A., with whom I collaborated closely throughout the duration of my PhD. Their support was essential for the successful completion of this project. This experience provided a valuable opportunity to approach research with a strong emphasis on practical and translational applications.

Chiesi Farmaceutici S.p.A. is a leading company in the field of respiratory diseases, including Bronchopulmonary Dysplasia (BPD). BPD is a chronic lung disease that affects extremely premature infants (born before 28 weeks of gestation), often resulting in long-term respiratory complications. It is a multifactorial disease with no effective cure currently available. Due to both increased survival rates among preterm infants and ethical limitations, human samples are scarce, making animal models indispensable for investigating BPD pathophysiology and developing new treatments.

This work emerged from the company's need to better characterize preterm rabbit models that mimic BPD. Rabbits offer a unique combination of advantages: they are small animals with short gestation periods and large litters, while also exhibiting lung development features similar to humans and the possibility to induce prematurity, traits typically found in larger animal models. Notably, the delivery of rabbit pups at gestational day 28 followed by exposure to hyperoxia effectively reproduces the hallmark features of BPD, including alveolar simplification and vascular and extracellular matrix remodeling. However, working with rabbits poses challenges in tissue characterization, due to the limited availability of validated antibodies. This restricts analyses primarily to standard histological methods, which may require multiple staining and sections to highlight BPD-relevant features. Additionally, some stains and antibodies do not always offer optimal specificity or contrast for quantification.

In this context, I proposed a multimodal, label-free optical approach to simultaneously detect BPD-related features in a single section, eliminating the need for dyes or antibodies. With suitable automation, this tool is envisioned as a future asset in preclinical BPD research.

For clarity, all animal procedures described in this work were conducted by accredited personnel at Chiesi Farmaceutici S.p.A., who also provided the lung tissue sections used in the study. The company also offered the support of expert histopathologists for the quantification of standard histological parameters. Most of the results presented here are included in a manuscript currently under peer review.

The thesis is structured as follows: an introductory chapter offering an overview of BPD and available animal models; a materials and methods section outlining the core principles of the technologies used and the key steps of the experimental workflow; and subsequent chapters dedicated to results, discussion, and future perspectives.

NEST SCUOLA NORMALE SUPERIORE

Chiesi
air rare care

TABLE OF CONTENTS

NOMENCLATURE

ACS: Antenatal corticosteroids

ADVT: Adventitia thickness

ALI score: Acute lung injury score

ATI - ATII: Epithelial cells type I and type II

BPD: Bronchopulmonary dysplasia

BR: Breathe rate

BSA: Bovine serum albumin

BW: Birth weight

DAB: 3,3’ diaminobenzidine

CA: Chorioamnionitis

C-sections: Caesarian sections

CD31: Cluster of differentiation 31

CPAP: Continuous positive airway pressure

Cst: Static compliance

ECM: Extracellular matrix

EDTA: Ethylenediaminetetraacetic acid

ELBW: Extremely low birth weight (< 1000g)

ETT: Endotracheal tube

EVs: Extracellular vesicles

FAD: Flavin adenine dinucleotide

FLIM: Fluorescence lifetime imaging microscopy

FRC: Functional residual capacity

G: Tissue damping

GA: Gestational age

H: Tissue elastance

H&E: Hematoxylin and Eosin

HFNC: High-flow nasal cannula

HRP: Horseradish peroxidase

i.m: Intramuscularly

IC: Inspiratory capacity

IGF: Insulin-like growth factor

IHC: Immunohistochemistry

IVH: Intraventricular hemorrhage severe

IMV: Invasive mechanical ventilation

INSURE: INtubation-SURfactant-Extubation

IUGR: Intrauterine growth restriction

LBW: Low birth weight (< 2500g)

Lm: Mean linear intercept

LMA: Laryngeal mask airway

Lmw: Mean wall intersection

Micro-CT: Micro-computed tomography

MSCs: Mesenchymal stromal cells

MT%: Medial thickness %

NAD(P)H: Reduced nicotinamide adenine dinucleotide (phosphate)

NEC: Necrotizing enterocolitis

NICU: Neonatal intensive care unit

NIPPV: Nasal intermitted positive pressure ventilation

NIV: Non-invasive ventilation

ON: Overnight

OXPHOS: Oxidative phosphorylation

PBST: PBS + Triton X

PCA: Principal component analysis

PCLS: Precision cut lung slices

PEEP: Positive end-expiratory pressure

PH: Pulmonary hypertension

PMA: Postmenstrual age

PND: Postnatal day

PSR: Picrosirius red

RAC: Radial alveolar count

RBC: Red blood cells

RCT: Randomized controlled trial

RDS: Respiratory distress syndrome

ROP: Retinopathy of prematurity

ROS: Reactive oxygen species

RT: Room temperature

RV: Residual volume

SDS: Sodium dodecyl sulfate

SNR: Signal to noise ratio

SRT: Surfactant replacement therapy

SHG: Second harmonic generation

TD: Tissue density

TEM: Transmission electron microscopy

TPEF / 2PE: Two-photon excitation fluorescence / Two-photon excitation

TRIS-HCL: Tris(hydroxymethyl)aminomethane hydrochloride

VEGF: Vascular endothelial growth factor

VILI: Ventilator-induced lung injury

VLBW: Very low birth weight (< 1500g)

V_T: Tidal Volume

WHO: World Health Organization

αSMA: Alfa smooth muscle actin

ABSTRACT

Bronchopulmonary dysplasia (BPD) is a chronic lung disease affecting extremely preterm neonates, causing significant long-term respiratory consequences. While hyperoxia-exposed preterm rabbits have been proposed as BPD models in pharmacological studies, lung alterations are conventionally assessed using classical histology and immunolabelling. Although fundamental in preclinical research, these methods often require multiple stains and tissue sections to reveal key BPD features. Additionally, the limited availability of validated antibodies for rabbits demands time-consuming optimization.

This study introduces a label-free, multi-modal imaging platform combining two-photon excitation fluorescence (TPEF), second harmonic generation (SHG), and fluorescence lifetime imaging microscopy (FLIM) to characterize the lung parenchymal alterations induced by a 7-day hyperoxia exposure in preterm rabbits.

Lung sections were obtained from preterm rabbit pups delivered at 28 days of gestational age (GA) (term 31 GA) either exposed for 7 days to normoxia (21% O_2) or hyperoxia (95% O_2), to mimic BPD. Lung sections were scanned with TPEF microscope at 780 nm and tissue intrinsic signals including autofluorescence intensity and lifetime, as well as SHG from collagen were simultaneously collected in the 470-570 nm, 420-460 nm, and 380-410 nm ranges, respectively. BPD-relevant features were extracted from images, validated through traditional staining and immunolabelling and analyzed using an optimized pipeline. The platform's validity was confirmed by correlating label-free features with conventional H&E-derived histomorphological parameters and lung function measurements.

This method simultaneously resolves key BPD-related features, such as tissue density, alveolar exudates, increased collagen deposition, arterial medial thickening, and alveolar simplification, effectively discriminating between hyperoxia and normoxia samples without dyes or antibodies. Quantitative outputs from the label-free pipeline strongly correlate with traditional histology and lung function measurements, confirming its robustness.

This approach holds promise as a powerful tool for preclinical research, enabling simultaneous imaging and quantification of multiple pathological features with a single label-free acquisition. Ultimately, this platform can complement conventional histology and immunolabelling to provide a more comprehensive and detailed assessment of tissue alterations.

Keywords

Bronchopulmonary dysplasia (BPD); preterm rabbit; Hyperoxia; Label-free; Two-photon excitation fluorescence (TPEF); Second harmonic generation (SHG); Fluorescence lifetime imaging microscopy (FLIM).

1 - INTRODUCTION

1.1 Human lung development

Lung development is a steady process that begins in the embryonic period with small foregut endodermal cells and evolves into a more complex structure composed of diverse cell populations in early childhood[1]. It is typically divided into five stages: embryonic, pseudoglandular, canalicular, saccular and alveolar, with the latter being mostly postnatal[2] (**Figure 1.1**). These stages are primarily defined by morphological criteria, and their transitions are not sharply demarcated, as most developmental processes begin proximally and extend toward the lung periphery, leading to overlapping phases[3,4] (**Figure 1.1**). Pulmonary circulation develops in parallel, progressing gradually alongside lung maturation[1].

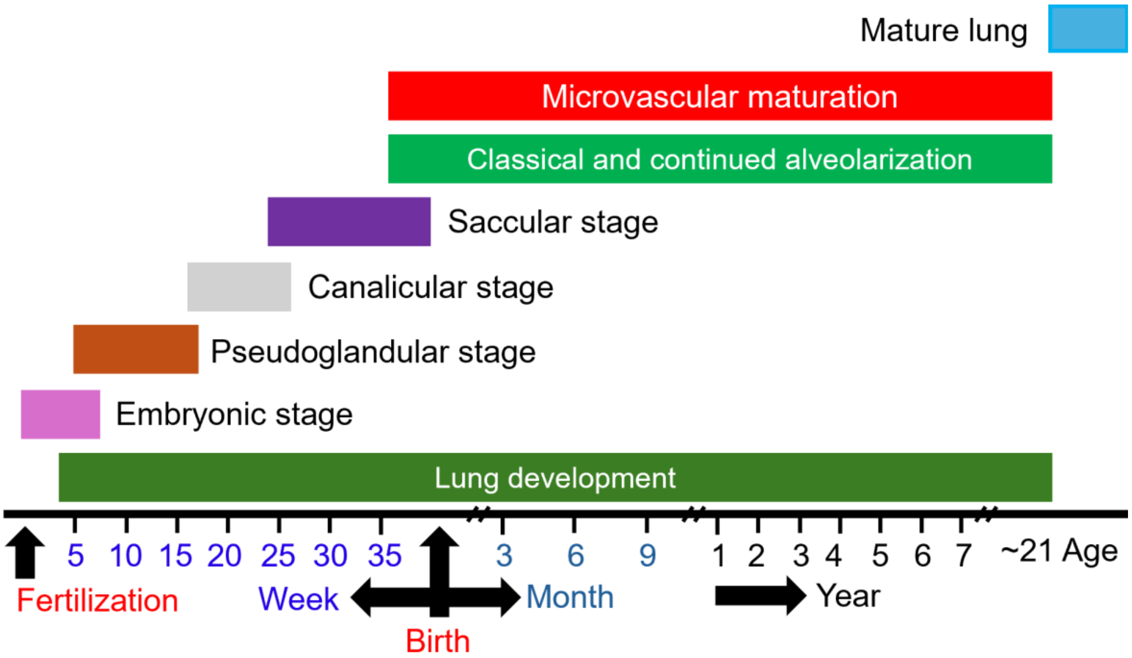

Figure 1.1 Time scale of human lung development. Lung development is typically divided into five stages: embryonic, pseudoglandular, canalicular, saccular and alveolar (alveolarization and microvascular maturation), the latter of which occurs mostly after birth. All stages of lung development overlap, as most developmental processes begin centrally and progress toward the periphery. "Classical" alveolarization is the process that gives rise to the majority of alveoli, but the formation of alveoli continues more slowly into young adulthood, with its precise endpoint still uncertain. Redrawn from Schittny et al.[3]

Embryonic period (4-7 weeks)

This is the period of lung organogenesis[1] (**Figure 1.2**). At day 26 post-conception, the anlage of the right and left lungs appears on the sides of the tracheal anlage[5] as two independent epithelial outpouchings from the primitive endodermal foregut[3]. Both lung buds begin to elongate and initiate a repetitive cycle of growth into the surrounding mesenchyme and branching which give rise to main bronchi, lobar and segmental bronchi[3]. This process, which is called “branching morphogenesis”, is guided by massive crosstalk between epithelial and mesenchymal cells and will originate all the future airways, mainly in pseudoglandur stage[3]. Simultaneously, pulmonary vessels are formed as a plexus in the mesenchyme surrounding the lung bud through vasculogenesis, while new capillary plexuses are formed through angiogenesis, following the bronchial tree of airways as a template[6]. Organogenesis is completed after the formation of the pleura[3].

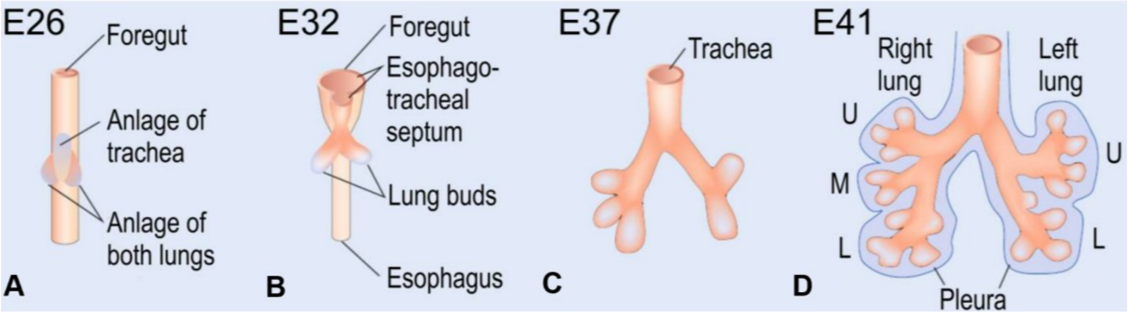

Figure 1.2 Lung organogenesis during embryonic period. (A) At day 26 post-conception (E26), the anlage of the right and left lungs appears on the sides of the tracheal anlage, originating from the primitive endodermal foregut. **(B)** The prospective trachea forms by a distal-to-proximal segregation from the foregut and the two lung anlages give rise to the two future main bronchi. Due to the branching morphogenesis, **(C)** at E37, lobar bronchi are formed and **(D)** at E41 segmental bronchi are formed. Organogenesis results completed after the formation of the pleura. Image adapted from Schittny et al.,[3]

Pseudoglandular period (5-17 weeks)

This is the period of bronchial tree formation, known as the pseudoglandular stage for the lung's resemblance to a tubular gland[3]. At the end of this stage, approximately the first 20 generations of the future airways are formed in humans[7] meaning that all conductive airways are present and the level of acini is reached. Starting proximally, the airways are lined by a high columnar epithelium. The height of the epithelial cells decreases continuously toward the terminal branches where cuboidal epithelium is found[3]. During the pseudoglandular stage, the first ciliated, goblet and basal cells appear in the proximal airways, and a continuous layer of α-smooth muscle actin-positive cell starts to form around the most proximal future airways[3]. By the end of this stage, vascular development is complete: arteries branch alongside airways, while veins run through connective tissue septa, forming a pre-acinar pattern similar to that of the adult lung[1].

Canalicular period (16-26 weeks)

In this period respiratory units become recognizable. The epithelial cuboidal cells differentiate into alveolar type II (ATII) and type I cells (ATI), allowing the morphological distinction between conducting and respiratory airways[3]. Furthermore, the ATI cells come into close contact with the mesenchymal capillary network, which, at this stage, is massively increased around the airspaces, and form the first air–blood barriers[3]. In this stage, the ATII cells of the lung start the production of pulmonary surfactant. Surfactant lines the alveoli and its role is to decrease surface tension at the air-liquid interface and so facilitate expansion of the lungs[1].

Saccular period (24-38 weeks)

During this period, acinar airways grow longer and wider, creating larger airspaces called sacculi, from which this stage takes its name. Primary septa develop where two airspaces meet, with capillary networks closely adhering to the septal surfaces, separated by condensed mesenchyme forming a connective tissue core. As a result, primary septa contain a double-layered capillary network[3]. The vascular system expands alongside the growth of respiratory tissue through increased vessel length and diameter[1]. Smooth muscle precursors begin to establish a fibrous network of elastin and collagen, which is essential for alveolarization. Additionally, the secretory activity of ATII cells increases, producing more surfactant[1].

Alveolar period (36 weeks to early childhood / young adulthood)

At term, human lung development is in the early alveolar stage[8], indicating that alveolarization occurs primarily after birth. By the end of the saccular stage, the lung parenchyma consists of thick, immature septa containing a double-layered capillary network (**Figure 1.3**), which is crucial for the formation of secondary septa[9]. During alveolarization, secondary septa are lifted from preexisting ones, leading to the subdivision of airspaces. These folds form where smooth muscle cell precursors have deposited elastic fibers and collagen fibrils[10,11]. Once formed, the septum rises to its full height and originates alveoli. As the new septa mature, their double-layered capillary network fuses into a single-layered structure (**Figure 1.3**) through a process known as microvascular maturation, thereby optimizing gas exchange[3]. During this phase, the alveolar surface area increases nearly 20-fold. Additionally, this stage is marked by an increase in surfactant secretion within the alveoli[1]. The end of the alveolar phase is still a subject of debate. It is widely accepted that the majority of the alveolar surface area is established by approximately 2-3 years of age. This is considered the "classic" phase of alveolarization. However, some evidence from both animal models and humans has suggested that the ability to form new alveoli, although at a much slower rate, may continue into early adulthood (phase of "continuous alveolarization")[12–15].

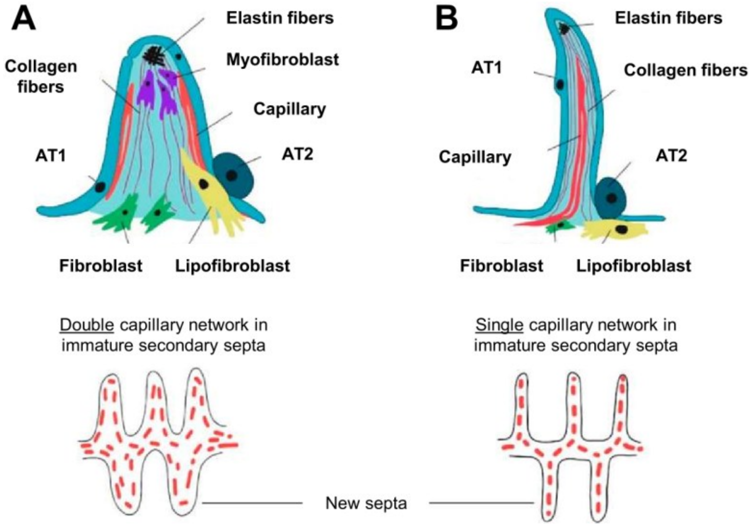

Figure 1.3 Secondary septa. **(A)** Immature structure with double layer capillary. **(B)** Mature structure with single layer capillary. Secondary septa lay down where smooth muscle cell precursors have deposited elastic fibers and collagen fibrils[10,11]. Image adapted from Rippa et al.[16]

1.2 Prematurity and current interventions

According to the World Health Organization (WHO), a birth is considered premature if it occurs before the 37th week of gestation and premature infants are generally classified based on gestational age (GA) or birth weight (BW)[17]:

Depending on GA, they are classified as:

- **Extremely preterm** (less than 28 weeks of gestation)
- **Very preterm** (28 to less than 32 weeks of gestation)
- **Moderate preterm** (32 to 34 weeks of gestation)
- **Late preterm** (34 to 37 weeks of gestation)

Depending on BW they are classified as:

- **Extremely low birth weight (ELBW)** (< 1000g)
- **Very low birth weight (VLBW) (**< 1500g**)**
- **Low birth weight (LBW)** (< 2500g)

Prematurity is an urgent public health issue, representing the leading cause of mortality and morbidity in infants. As reported by the WHO, an estimated 15 million babies are born prematurely each year, with approximately 1 million dying from related complications. Indeed, premature infants remain at risk of a range of both short- and long-term complications[18], whose incidence and severity increase as GA and BW decrease.

The exact cause of prematurity is often unclear, but certain factors can increase the risk. These include[18]:

- Pregnancy history and characteristics (previous preterm delivery or miscarriages, multiple gestations, assisted reproduction)
- Maternal health conditions (infections, diabetes, high blood pressure, thyroid disorders, stress, depression, low body max index)
- Maternal lifestyle choices (smoking, alcohol and drug use)
- Maternal ethnicity and genetic influences

The lungs are particularly vulnerable to preterm birth, as premature delivery disrupts their normal development, often leading to postnatal respiratory complications[19]. In infants born between the late canalicular and saccular stages of lung development, alveolarization and microvascular maturation have not yet occurred[1], and the surfactant system is still immature[1]. This surfactant deficiency is a major cause of the respiratory distress syndrome (RDS)[1], one of the leading reasons for admission of preterm infants to the Neonatal Intensive Care Unit (NICU)[20] where they receive life-saving postnatal interventions, including mechanical ventilation, supplemental oxygen, and surfactant replacement therapy.

Invasive mechanical ventilation (IMV) via an endotracheal tube has long been considered the standard treatment for infants with RDS[21], but its association with lung injury (inflammation, volutrauma, barotrauma etc.) and BPD[22–24] has led to the adoption of less harmful, non-invasive ventilation (NIV) strategies in spontaneously breathing infants. Among these, the use of continuous positive airway pressure (CPAP), rather than intubation, is recommended as the first choice for primary respiratory support [25] and has been shown to reduce lung injury and BPD[26]. However, CPAP failure remains common in the first week (~ 50% of cases)[27,28], leading neonatologists to investigate more effective NIV strategies such as nasal intermittent positive pressure ventilation (NIPPV) and high-flow nasal cannula (HFNC). NIPPV, compared to CPAP, has been associated with reduced rates of respiratory failure and intubation, with variable effects on BPD or mortality, ranging from no effect to a slight reduction[29–31]. HFNC, although favored for improved patient comfort and ease of use, appears less effective than CPAP[32]. Alongside ventilation, oxygen supplementation is a key intervention to support breathing, with current European guidelines recommending oxygen saturation levels between 90% and 94%[25]. However, oxygen supplementation and ventilation alone are not often enough to support preterm infants' recovery with surfactant deficiency.

To solve this issue, Fujiwara administered the first surfactant replacement therapy (SRT) in 1980[33]. Initially, surfactant administration was strictly associated with intubation and mechanical ventilation. However, when CPAP became the preferred respiratory support, less invasive surfactant delivery strategies were investigated to be coupled with this method[34,35]. These strategies involve the administration of surfactant through a narrow, non-ventilable tube, usually a feeding or vascular catheter or a dedicated one of similar diameter, instead of an endotracheal tube (ETT)[36]. Different variants and acronyms for this procedure have been described, with LISA being the most common[35]. A meta-analysis showed that LISA methods significantly reduce the risk of BPD, death during first hospitalization, early intubation and severe intraventricular hemorrhage (IVH), compared to surfactant administration via ETT with immediate (INSURE) or delayed extubation[37]. LISA has also shown superiority in preventing BPD over nasal CPAP alone[38]. However, deeper investigation into the pathophysiology and greater attention to the design of the studies are important to avoid bias and overestimation of beneficial effects of LISA techniques[36,39]. Other methods for non-invasive surfactant administration, such as nebulization[40] and delivery via the pharynx or laryngeal mask airway (LMA)[41], show promise but require further evaluation before they can be widely implemented[17].

In addition to postnatal interventions, antenatal corticosteroids (ACS) are routinely administered to reduce respiratory morbidity in pregnancies at risk of preterm delivery between 24 and 34 weeks of gestation[42]. The optimal interval between treatment and delivery is more than 24 hours and less than 7 days[25]. ACS accelerate fetal lung maturation by increasing the activity of enzymes involved in surfactant biosynthesis, leading to improved survival rates and a reduced incidence of RDS[43,44]. However, risks of ACS remain a topic of debate, particularly when there is no effective preterm delivery[45].

The aforementioned advancements in neonatal care, have significantly improved survival in extremely preterm infants; however, long-term complications remain common, with BPD being the most prevalent chronic condition affecting lung development[46,47].

1.3 Bronchopulmonary dysplasia (BPD)

1.3.1 From "old" to "new" BPD: definition and incidence

In 1967, Dr Northway and colleagues first described BPD as a chronic pulmonary disorder occurring in preterm infants with severe RDS who had been exposed to aggressive mechanical ventilation and high concentrations of inspired oxygen for at least 7 days[48]. Infants exhibited persistently abnormal lung fields on chest radiographs, while autopsy findings revealed airway disease, distal lung inflammation, diffuse fibroproliferative changes, and hypertensive remodelling of the pulmonary vasculature[48]. By today's standards, the preterm population described by Dr. Northway would be considered relatively mature. At the time of its study, mortality rates were high, and the surviving infants, who were potentially at risk for BPD, had a mean GA of 34 weeks and an average BW of 2,311 grams[49]. As discussed in the previous paragraph, recent advancements in neonatal support techniques, have substantially increased the survival rates of infants born at extremely preterm GA[46], thereby reshaping the profile of at-risk neonates. However, the incidence of BPD has remained unchanged[49,50]. A recent publication provides a global estimate of BPD prevalence in VLBW and/or low GA neonates over the period 1990-2019, reporting rates of approximately 35% or 21%, depending on whether the definition at 28 days or at 36 weeks postmenstrual age (PMA) is applied[50] (definitions in **Figure 1.4**). Notably, the current BPD pathophysiology (called the "new" BPD) differs significantly from the "old", originally described by Northway. The "new" BPD is primarily associated with extreme prematurity, where disrupted alveolarization leads to both alveolar and vascular impairments, with less evidence of emphysema, fibrosis, and airway changes compared to the original phenotype[51]. The definition of BPD, as well as the criteria for assessing its severity, have also evolved over time, adapting to changes in the at-risk population and to new treatment strategies. A list of definitions is shown in **Figure 1.4**.

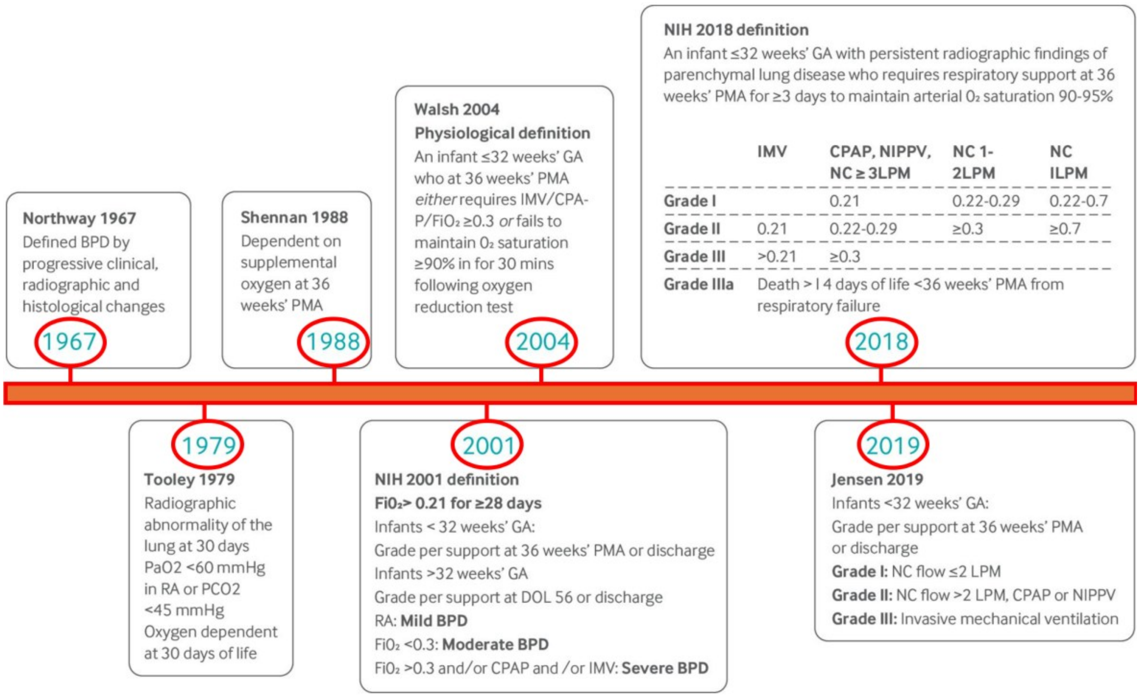

Northway 1967
Defined BPD by progressive clinical, radiographic and histological changes

Tooley 1979
Radiographic abnormality of the lung at 30 days
PaO2 <60 mmHg in RA or PCO2 <45 mmHg
Oxygen dependent at 30 days of life

Shennan 1988
Dependent on supplemental oxygen at 36 weeks' PMA

NIH 2001 definition
FiO_2> 0.21 for ≥28 days
Infants < 32 weeks' GA:
Grade per support at 36 weeks' PMA or discharge
Infants >32 weeks' GA
Grade per support at DOL 56 or discharge
RA: **Mild BPD**
FiO_2 <0.3: **Moderate BPD**
FiO_2 >0.3 and/or CPAP and /or IMV: **Severe BPD**

Walsh 2004
Physiological definition
An infant ≤32 weeks' GA who at 36 weeks' PMA *either* requires IMV/CPAP/FiO_2 ≥0.3 *or* fails to maintain O_2 saturation ≥90% in for 30 mins following oxygen reduction test

NIH 2018 definition
An infant ≤32 weeks' GA with persistent radiographic findings of parenchymal lung disease who requires respiratory support at 36 weeks' PMA for ≥3 days to maintain arterial O_2 saturation 90-95%

	IMV	CPAP, NIPPV, NC ≥ 3LPM	NC 1-2LPM	NC ILPM
Grade I		0.21	0.22-0.29	0.22-0.7
Grade II	0.21	0.22-0.29	≥0.3	≥0.7
Grade III	>0.21	≥0.3		
Grade IIIa	Death > l 4 days of life <36 weeks' PMA from respiratory failure			

Jensen 2019
Infants <32 weeks' GA:
Grade per support at 36 weeks' PMA or discharge
Grade I: NC flow ≤2 LPM
Grade II: NC flow >2 LPM, CPAP or NIPPV
Grade III: Invasive mechanical ventilation

Figure 1.4 Evolution of the definition of BPD over time. Image adapted from Gilfillan et al.[52]

1.3.2 BPD risk factors

While the traditional view held that BPD was primarily caused by oxidant- and ventilation-mediated injuries[48], it is now well established that multiple factors contribute to its pathogenesis, likely acting additively or synergistically to promote lung damage[53]. Factors that contribute to BPD may be antenatal, natal, or postnatal in origin[54] (**Figure 1.5**).

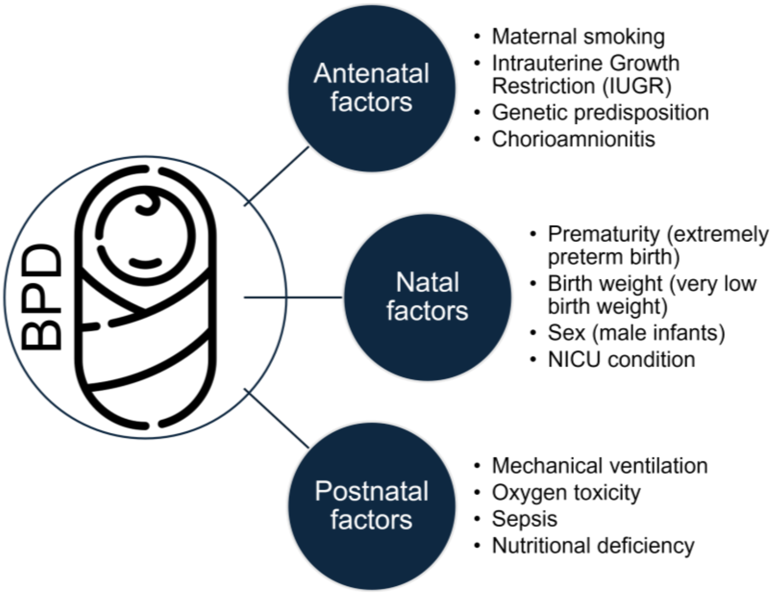

Figure 1.5 Main risk factors in the pathogenesis of BPD.

1.3.2.1 Prenatal risk factors

Maternal smoking

Preterm infants born from mothers who smoked during pregnancy have an increased risk of developing BPD[55,56]. Epigenetic changes, placental dysfunction, altered ATII metabolism and dysregulated angiogenesis are some of the postulated mechanisms through which cigarette smoke disrupts normal lung development and function[54].

Intrauterine Growth Restriction (IUGR)

IUGR has been defined as the rate of fetal growth that is below normal considering the growth potential of a specific infant as per the race and gender of the fetus[57]. It has been demonstrated that IUGR increases the risk of developing BPD[58,59]. The biological mechanisms underlying IUGR, including placental dysfunction and deficiencies in insulin-like growth factor (IGF), vascular endothelial growth factor (VEGF), and VEGF receptors, are also believed to contribute to restricted fetal lung development, impaired formation of terminal airways and gas exchange units, reduced expression of surfactant proteins and their mRNA, and potentially to an exaggerated inflammatory response[59].

Genetic predisposition

There is growing evidence that BPD has a significant genetic component, although the precise mechanisms remain incompletely understood[54]. Twin studies have shown higher concordance rates of BPD among monozygotic twins compared to dizygotic twins, particularly in cases of moderate to severe disease[60,61]. Despite these findings, no single gene has been definitively linked to BPD[62].

Chorioamnionitis (CA)

CA, an inflammation of the fetal membranes primarily caused by bacterial infection[54,63], has been proposed as a risk factor for BPD due to its ability to elevate proinflammatory cytokines in the amniotic fluid, potentially leading to fetal lung damage and inflammation even before birth[64]. However, the association between CA and BPD remains controversial. While a meta-analysis of 158 studies supports CA as a significant risk factor[65], a large 25-year cohort study of VLBW infants suggests its effect is indirect, mediated by preterm birth and neonatal sepsis[66]. Some studies even report a protective effect[67,68]. These discrepancies suggest CA may have dual effects: certain exposures may trigger a harmful inflammatory response that increases the risk of BPD whereas others might promote lung maturation and reduce the severity of RDS[69].

1.3.2.2 Natal risk factors

Prematurity and low BW are among the strongest predictors of BPD, with the risk increasing proportionally with both factors[54]. A notable sex bias has also been observed, with preterm males exhibiting a higher risk and more severe symptoms compared to females of the same GA[70,71]. NICU conditions can also have an impact[72].

1.3.2.3 Postnatal risk factors

Mechanical ventilation

Many surviving extremely preterm infants require mechanical ventilation. Although it is a life-saving intervention, mechanical ventilation can cause ventilator-induced lung injury (VILI), which interferes with lung development in preterm infants. To minimize this risk, whenever possible, less invasive ventilation strategies are now preferred (for details, see paragraph 1.2). The major determinants of VILI include barotrauma (from excessive airway pressure), volutrauma (resulting from lung overdistension), atelectrauma (due to ventilation of inadequately recruited lungs regions), and biotrauma (triggered by the release of inflammatory mediators, often as a consequence of the aforementioned injuries)[54]. All these factors, interacting with patient-specific conditions, result in an inflammatory cascade that disrupts signalling pathways involved in lung development and repair, thereby contributing to the onset of BPD[54,73].

Oxygen toxicity

While supplemental oxygen is a life-saving intervention for preterm infants with hypoxic respiratory failure, excessive or prolonged oxygen exposure is recognized as a major contributor to the pathogenesis of BPD[54,74]. Hyperoxia promotes the production of reactive oxygen species (ROS) and upregulation of proinflammatory cytokines, leading to lung injury and impairing reparative processes in the developing lung, which may result in the development of BPD[54]. The increased levels of ROS, further exacerbated by the immature antioxidant defenses of premature infants[75,76], trigger inflammatory response, changes in gene expression and mitochondrial function, along with disruptions in both alveolar and vascular development[77] **(Figure 1.6)**.

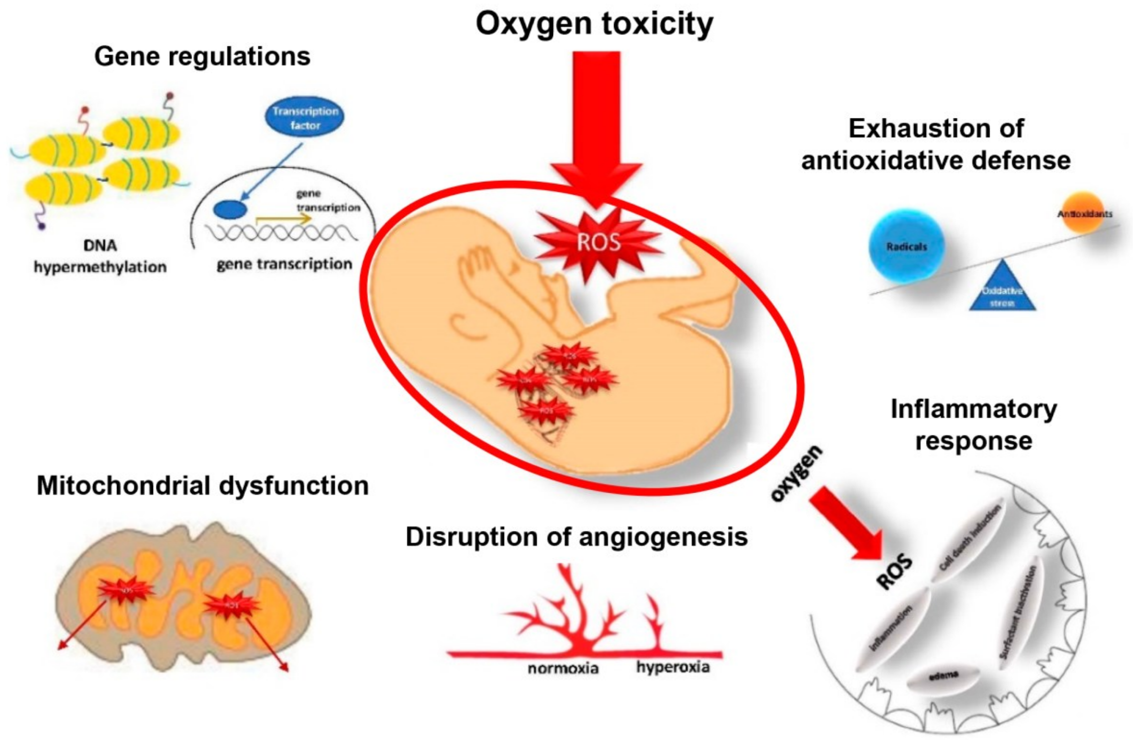

Figure 1.6 Effect of oxygen toxicity on immature lungs. Image adapted from Choi *et al*. 2021[77]

Sepsis

Preterm infants are more susceptible to infections since their immune defenses are not fully developed[73,78]. Multiple observational studies implicate postnatal sepsis as an independent risk factor for BPD[68,79]. Sepsis interrupts lung development and leads to BPD by mechanisms that entail inflammation, oxidative stress, and endothelial injury in the lungs[54].

Nutritional deficiency

Adequate nutritional support is essential for preventing BPD in preterm infants, as malnutrition can impair lung development by disrupting alveolarization, collagen deposition, and affecting the bronchiolar epithelium as shown in animal models[80–82]. Malnutrition is common in premature infants due to challenges with oral feeding and immature gastrointestinal function[83].

1.3.3 Pathophysiology of BPD

The pathophysiology of BPD has evolved significantly over the past two decades and remains an active area of research[54]. The "new" BPD is recognized as a chronic lung disease with a multifactorial pathogenesis, in which inflammation plays a central role[17].

Both pre- and postnatal risk factors, such as CA, oxygen toxicity, mechanical ventilation, and infections, can trigger and sustain a complex inflammatory response in the airways and lung tissue of very premature infants **(Figure 1.7)**. This process involves the accumulation of neutrophils and macrophages and the release of pro-inflammatory mediators, including cytokines, oxygen radicals, lipid mediators, and proteases, which affect the alveolar-capillary unit and compromise tissue integrity[84]. This pro-inflammatory mechanism is not adequately counterbalanced by anti-inflammatory responses, and increasing evidence indicates that BPD results, at least in part, from this persistent imbalance favoring pro-inflammatory pathways[84]. Inflammation onset and subsequent lung injury are further aggravated by oxidative stress driven by ROS[84].

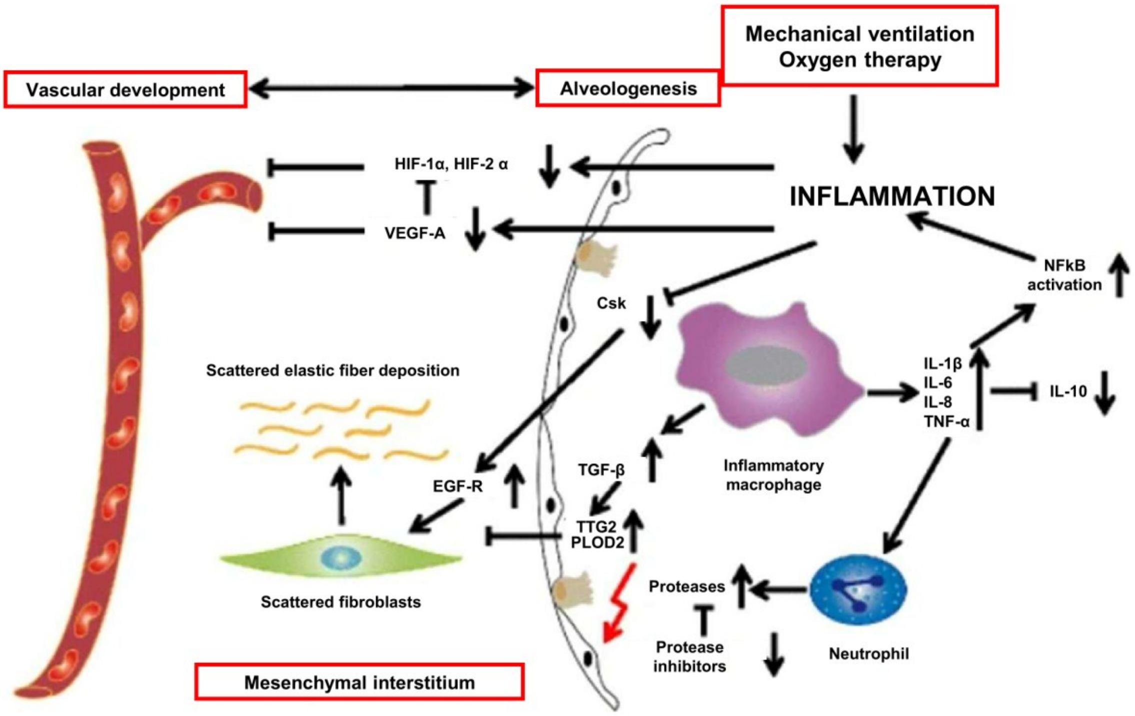

Figure 1.7 Impact of pulmonary inflammatory response on the premature lung. Image adapted from Shahzad et al.[85]

Inflammation is crucial in the translation of different injury mechanisms into structural and functional changes[86]. Although BPD can present with a range of clinical manifestations and phenotypes, lung parenchymal abnormalities **(Figure 1.8)**, pulmonary vascular disease **(Figure 1.8)**, and functional alterations often coexist in affected patients[54,87]. Airway and vascular lesions are more commonly observed in infants who go on to develop more severe forms of the disease over time[88].

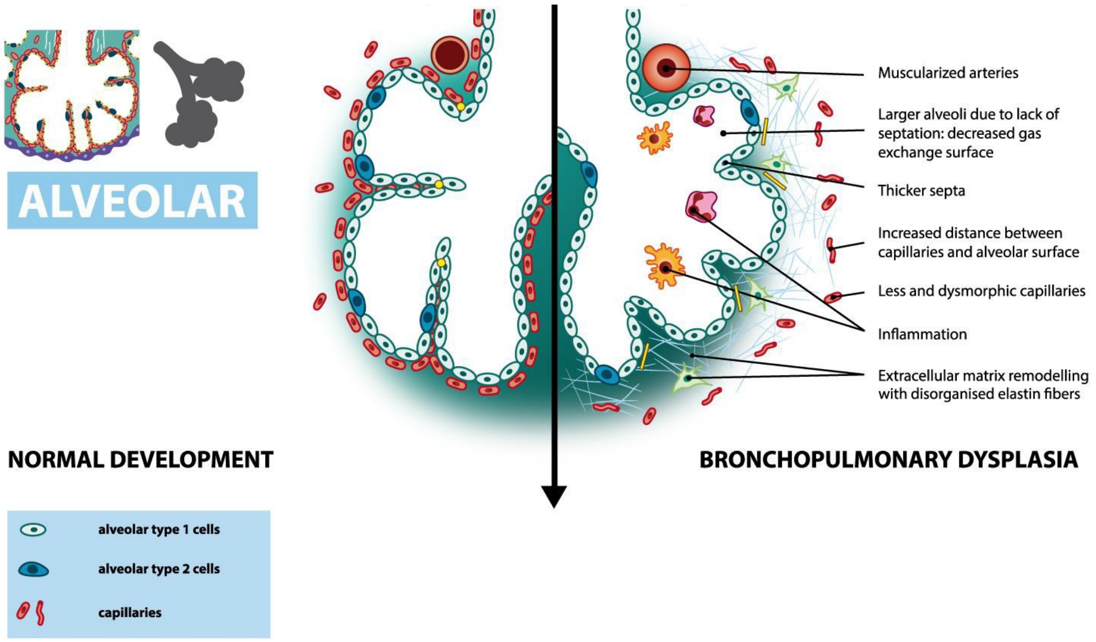

Figure 1.8 Histomorphological alterations of lung parenchyma and pulmonary vessels in human BPD. Image adapted from Salaets et al.,[87]

1.3.3.1 Lung parenchymal alteration

To date, our understanding of histological changes in the lung parenchyma of neonates with the “new” BPD is based on a limited number of relatively dated human tissue studies[87]. The increased survival rate of preterm infants due to advances in perinatal care, coupled with ethical restriction, has resulted in a scarcity of human samples. The most comprehensive histological evaluation in the post-surfactant era was conducted by Husain et al.,[89] who examined autopsy samples from 14 surfactant-treated infants (not exposed to antenatal steroids), 8 untreated infants, and 15 age-matched healthy controls. This study revealed impaired alveolar development, characterized by a reduced radial alveolar count (RAC) and an increased mean linear intercept (Lm), indicating fewer but larger alveoli. These findings were consistent with earlier autopsy studies of extremely premature infants who had not received surfactant[90–92]. Similar patterns of alveolar impairment, specifically alveolar simplification, enlarged airspaces, and poor secondary crest formation, were also observed in biopsies from BPD survivors who had not received surfactant or antenatal steroids[88]. The study further reported variable degrees of alveolar wall cellularity and fibrosis in these biopsies. In addition, altered elastin fiber deposition has been noted in pre-surfactant era autopsy specimens, with increased but disorganized elastin content[91,92]. Since the upfoldings that give rise to secondary septa in the developing lung occur where smooth muscle cell precursors deposit strings of elastic fibers and collagen fibrils[3,4,11], disorganization of the extracellular matrix (ECM) may further hinder alveolar development[93].

1.3.3.2 Pulmonary vascular disease

There is a strong interplay between pulmonary vasculature development and alveolar formation[3,94]. In BPD, this tightly regulated relationship is disrupted. Alongside alveolar simplification, autopsy and biopsy specimens from BPD also demonstrated significant vascular and microvascular impairment[88,95,96] which led to a reduced and inefficient alveolar-capillary interface and, consequently, suboptimal pulmonary gas exchange[54]. The structural configuration of the distal microvasculature is abnormal, appearing dysmorphic, showing an irregular distribution of alveolar capillaries containing vessels positioned farther from the air surface, or displaying immaturity by retaining a saccular architectural pattern[88,95–97]. Moreover, smooth muscle proliferation leads to increased medial thickness in the walls of small pulmonary arteries[86,98,99]. The combination of dysmorphic vasculature and impaired angiogenesis in BPD significantly increases the risk of elevated pulmonary arterial pressures and the development of BPD-associated pulmonary hypertension (PH)[100]. The incidence of PH among patients with BPD, regardless of disease severity, has been reported to be 17% and up to 24% in those with moderate to severe disease[101]. PH contributes significantly to morbidity and mortality in this population[101].

1.3.3.3 Lung function

A variety of functional tests using different techniques have been performed in both short- and long-term studies to investigate lung function abnormalities in neonates who develop BPD[102]. Infants with BPD exhibit features consistent with obstructive airway disease[54,87,103,104]. While functional residual capacity (FRC) tends to be lower during the neonatal period in preterm infants who go on to develop BPD[105], in evolving BPD, both FRC and residual volume (RV) are found increased, indicating hyperinflation and air trapping[54,87]. Besides airway disease, preterm infants developing BPD also have lower lung compliance[103,105], and decreased gas exchange efficiency[87].

1.3.4 Long term outcomes

Long-term outcomes of the “new” BPD remain poorly characterized, as many neonates who developed BPD under modern treatment protocols are only now reaching childhood or early adulthood[34]. However, available follow-up studies of BPD survivors indicate an increased frequency of rehospitalization (up to 49% during the first year of life[106]) and persistent pulmonary dysfunction, including airway obstruction, asthma-like symptoms, exercise intolerance, elevated risk of PH and greater susceptibility to infections[34,100,107,108]. Beyond respiratory health, BPD survivors also show an elevated risk of long-term neurodevelopmental disorders[109–111].

1.3.5 Preventive and therapeutic strategies

Despite advances in neonatal care, no breakthrough therapies have reached routine use in recent decades, and BPD remains without a definitive cure[112]. Its multifactorial nature demands for a comprehensive, multi-faceted approach to both prevention and treatment[113]. In addition to previously mentioned strategies (NIV, controlled oxygen therapy, SRT, and ACS), other interventions have already been integrated into standard care or are currently under evaluation.

1.3.5.1 Caffeine

Caffeine, a methylxanthine compound, functions as a non-specific inhibitor of adenosine receptors[114] and is widely used in the treatment of apnea in preterm infants[34]. The Caffeine for Apnea of Prematurity (CAP) study showed a significant reduction in the number of days of respiratory support, the incidence of BPD and improvements in neurodevelopmental outcomes at 18 months of age[115,116]. Subgroup analysis from the CAP trial showed that earlier administration (within the first three days of life) resulted in a larger reduction in days of respiratory support compared to later initiation[117]. Questions remain regarding the optimal dosage and timing of caffeine initiation to prevent or mitigate BPD[25,52].

1.3.5.2 Vitamin A

Preterm infants often lack vitamin A, which is essential for lung development and the structural integrity of the respiratory tract[34]. A Randomized Controlled Trial (RCT) in ELBW infants found that early intramuscular administration of vitamin A modestly reduced the risk of death or BPD by 36 weeks PMA[118]. However, due to the modest benefit and the discomfort of repeated injections, routine use was not widely adopted. Trials using enteral vitamin A showed no conclusive benefit in preventing BPD[119,120]. Current recommendations suggest that vitamin A supplementation in preterm infants should be carefully considered, balancing potential benefits with its limitations and risks[34].

1.3.5.3 Postnatal corticosteroids

Corticosteroids (e.g., dexamethasone, hydrocortisone, budesonide) have been proposed to reduce the inflammation involved in the pathogenesis of BPD[113,121]. Early systemic administration of dexamethasone has been shown to lower the incidence of BPD and reduce mechanical ventilation duration[122]. However, when given within the first week of life, it is also associated with an increased risk of adverse neurodevelopmental outcomes[122], discouraging its adoption[52]. A low-dose (0,89 mg/kg over 10 days) administration after one week of life, may facilitate extubation without worsening outcomes, though it does not appear to reduce the overall incidence of BPD[123]. Recent systematic reviews and metanalyses indicate that moderate use of dexamethasone between 7 and 21 days of life reduces the risk for both BPD and the combined outcome of BPD and mortality[124,125]. However, further investigation is needed to determine the optimal dose, as well as clarify long-term effects[124,126]. European Consensus guidelines recommend considering a short, tapering course of low-dose dexamethasone to facilitate extubation in infants who remain on mechanical ventilation after 1–2 weeks[25]. In contrast, low-dose hydrocortisone administered within the first week of life has been associated with a modest but significant reduction in BPD risk, without increasing the likelihood of neurosensory impairment[52]. In certain preterm subgroups associations with possible adverse effect such as late-onset sepsis, gastrointestinal perforation and IVH have been reported[126].

To minimize systemic side effects, inhaled corticosteroids have also been investigated, showing an association with reduced BPD incidence at 36 weeks PMA[127]. However, studies by Bassler et al. reported a potential increase in mortality with inhaled budesonide[128,129], highlighting the need for further research to define the optimal dosing, timing, and safety of inhaled corticosteroids. Furthermore, although the combination of budesonide and surfactant initially showed promise, recent trial in infants at a mean GA of 25.6 weeks receiving surfactant suggests that early intratracheal budesonide may have little to no effect on survival free of BPD[130].

1.3.5.4 Mesenchymal stromal cells (MSCs) and Extracellular vesicles-derived MSCs

MSCs are multipotent cells with immunomodulatory and regenerative properties, capable of differentiating into various cell types, including those of lung[131]. Isolated from sources such as adipose tissue, umbilical cord blood, and placenta, MSCs exhibit anti-inflammatory, antifibrotic, proangiogenic, and antiapoptotic effects, making them promising candidates for treating BPD[131,132]. A phase II RCT confirmed their therapeutic potential by decreasing severe BPD incidence in infants born at 23–24 weeks compared to placebo[133]. However, key aspects remain unresolved, including large scale production, optimal cell source and administration protocol, and long-term safety[34,134.] Growing evidence suggests that MSCs exert their therapeutic effects primarily through paracrine mechanisms, particularly via extracellular vesicles (EVs), rather than through cell replacement[131]. MSC-derived EVs have demonstrated several potential benefits for BPD[131] and, as a cell-free therapy, offer low immunogenicity, no tumorigenic risk, and the ability to enable targeted delivery or therapeutic cargo loading[135]. Despite promising preclinical results, their clinical application remains unrealized[135]. Key obstacles include EV heterogeneity, the lack of standardized production and quality control protocols, and an incomplete understanding of their mechanisms of action[135].

1.3.5.5 Insulin like growth factor I (IGF-1)

IGF-1 is an important regulator of fetal growth, lung angiogenesis and development[136]. Preterm neonates displayed lower serum of IGF-1, and deficiencies have been linked to the pathogenesis of BPD[137]. A phase IIa clinical trial designed to evaluate the safety and efficacy of recombinant human IGF- 1 complexed with its binding protein (rhIGF-1/ rhIGFBP-3) in the prevention of ROP noted a statistically significant decrease in the incidence of BPD[138].

Notably, there are other compounds in clinical development for BPD, including Anakinra (interleukin 1 receptor antagonist)[139] and recombinant human surfactant protein D[140].

1.4 Translation of BPD phenotype in animal models

Despite advances since Dr. Northway's initial description, significant gaps remain in our understanding of BPD's pathogenesis, pathology, and clinical management, highlighting the urgent need for deeper insight and novel therapies[141]. Increased survival and ethical constraints have limited access to pathological human samples, and when available are often from severe cases and thus not fully representative[93]. In this context, animals models play a crucial role for studying BPD mechanisms and testing therapies.

To date, no standardized preclinical model of BPD has been established. Instead, various animal models, exposed to different external insults such as hyperoxia, mechanical ventilation, or perinatal inflammation, have been used to investigate the pathophysiology of BPD[87]. This lack of standardization stems both from the heterogeneous nature of the disease, which is challenging to fully recapitulate in animal models, and from the unique set of translational and practical advantages and limitations inherent to each model. Choosing the appropriate model requires balancing factors such as lung development stage (**Figure 1.9**), manipulability, reagent availability, animal size, cost, gestation, and ethics[142].

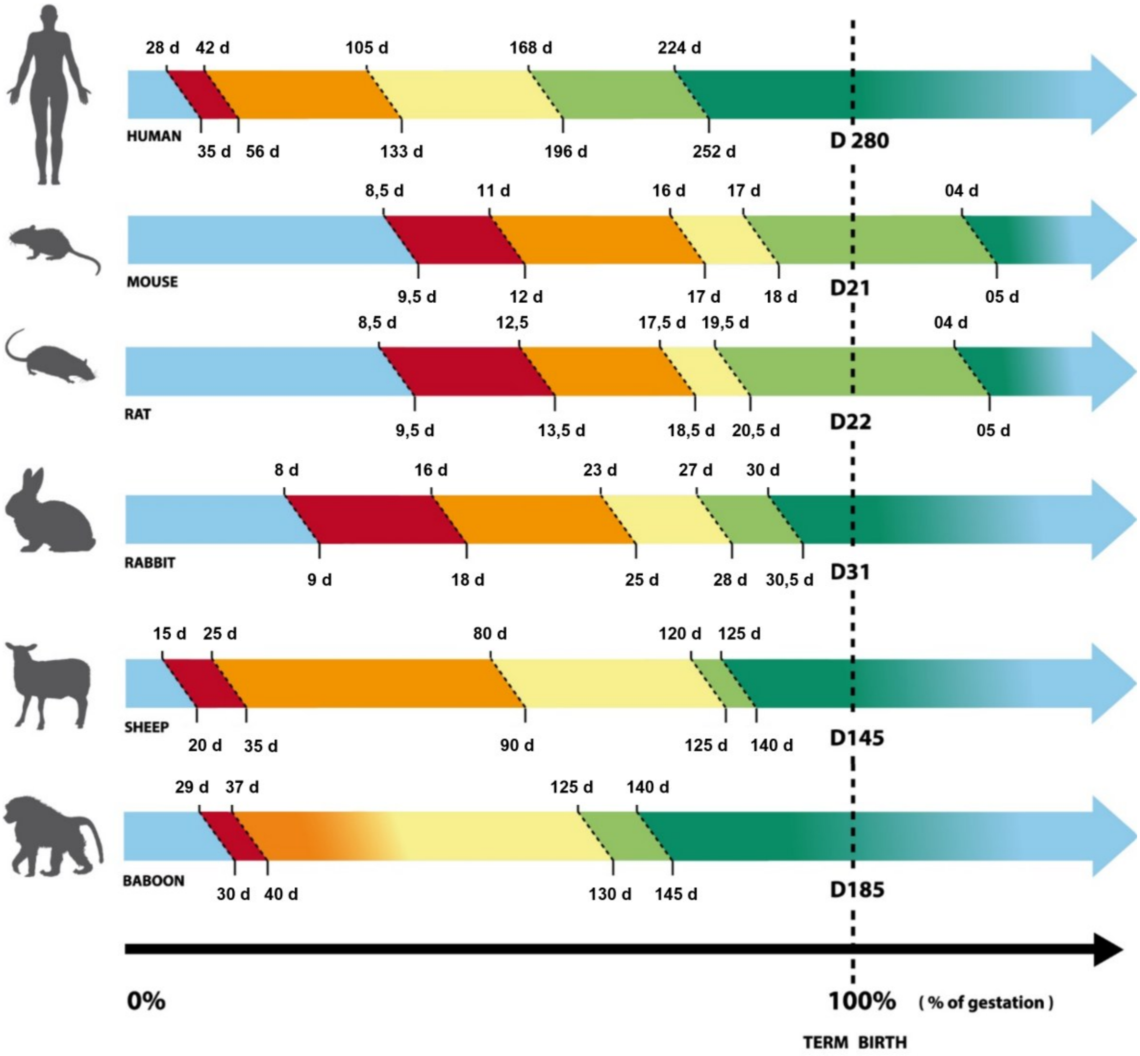

Figure 1.9 Comparative mammalian lung development. Image adapted from Salaets et al.[87]

1.4.1 Small animal models: Rats and mice

Term mice and rats have been widely used in BPD research. At term both mice and rats are in the saccular phase of lung development (**Figure 1.9**), which is morphologically like human premature infants at 28-30 weeks of gestation[87], and start alveolarization only at postnatal day 5 (PND5)[143]. Lung injury in these animals was induced trough hyperoxia, hypoxia, prenatal inflammation, transgenesis, or short-term mechanical ventilation[87]. Among these, the hyperoxia model is the most employed. Varying the concentration and duration of oxygen exposure has been shown to reproduce different severity of histopathological features of BPD[143,144]. In mice, the optimal window for modeling the new BPD corresponds to the first 4-5 PND[143]. Some protocols have also incorporated brief periods of invasive ventilation starting on PND 5–6. However, technical limitations hinder earlier ventilation exposure and make it difficult to replicate the less invasive respiratory support commonly used in human neonates[87,143]. For practical reasons, rodents are well-suited models: they are small, have short gestation (21 days for mice, 22 days for rats) with large litter size, are low cost and have a short lifespan, which enable the investigation of “long-term” consequences[143,144]. Moreover, a major advantage of the mouse models (and to a lesser extent, rats) is the availability of reagents and technologies for detailed pathway analysis, including gene knockout strains, validated antibodies, omics approaches, and advanced microscopic techniques[87]. While term rodents remain valuable for basic research and pathway analysis in BPD, concerns persist about the translatability of findings to human disease[87]. For example, although term rodents born with lungs structurally similar to those of preterm human infants, they do not face the same gas exchange limitations or oxygen-related injuries, as their lungs are functionally mature at birth and have sufficient surfactant and antioxidant enzyme levels[87,143,144]. To date, truly preterm mouse and rat models have not been described[87].

1.4.2 Large animal models: Baboons and lambs

In BPD research, commonly used large animal models include the preterm lamb and the preterm baboon. Lung development in these species, particularly in baboons, closely mirrors that of humans, as alveolarization begins before birth and the duration of each developmental stage is proportionate to that observed in humans **(Figure 1.9)**. These animals can be delivered prematurely and exhibit respiratory failure similar to that of preterm infants, requiring mechanical ventilation or non-invasive respiratory support[87,142,145]. This makes it possible to create BPD models that combine extreme lung immaturity with ventilation injuries[145–148]. In addition, standard neonatal care interventions such as administration of exogenous surfactants, antenatal steroids, titrated oxygen supplementation, and caffeine, have also been implemented in these models[87].

Other advantages include the possibility to study disease progression or long-term effect of treatments over an extended period[142], as well as to investigate obstructive airway disease, owing to anatomical similarities[145]. While large animals can closely model human physiology and current neonatology practices, their use is limited by long gestation, small litter sizes, high costs, infrastructure needs, and ethical concerns[142,149]. Moreover, there is limited availability in terms of antibodies and reagents that obstacle deepened studies[87].

1.4.3 Preterm rabbit models: a good compromise between large and small animals

Rabbits represent a good compromise between large and small animal models **(Figure 1.10)**. Like baboons and lambs, their lung development closely mirrors that of humans, with alveolarization starting in utero. At the same time, rabbits retain the typical advantages of small animals, such as a short gestation period (31 days) **(Figure 1.9)**, large litter sizes, ease of housing, and relatively low maintenance costs[87,150]. Moreover, they are small, but large enough to permit perturbations, including nebulized treatments, short mechanical ventilation, and pulmonary function testing[150–154]. Although the term model has been used to mimic BPD, primarily through various hyperoxia protocols[155–158], it may not be ideally suited for studying alveolar development in the context of BPD, since this process has already begun in full-term rabbits[142]. Moreover, at term, they have mature surfactant and antioxidative system[150] that do not reflect the lung function immaturity of preterm infants. However, one of the main advantages of rabbits compared to rodents is that they can be delivered prematurely. Preterm rabbits delivered by Cesarean section (C-sections) at 28-29 GA are in the early saccular phase of lung development **(Figure 1.9)** and have structurally and functionally immature lungs, with underdeveloped surfactant and antioxidant systems[87,150,159,160]. This closely mimics the condition of preterm human infants and offers a significant advantage in terms of translational relevance[87]. Additionally, although premature, rabbits appear capable of survive and being instrumented[158].

Based on the technical and functional considerations outlined above, preterm rabbits represent a relevant model for studying BPD. In this model, the lung injury is primarily induced by hyperoxia[87]. In 2009, Mascaretti et al., used preterm rabbit delivered at 28 GA and exposed them to either FiO2 > 95% or room air for 11 days[161]. Lungs from the hyperoxia-exposed group showed a BPD-like phenotype, but mortality was extremely high (89%)[161]. Subsequently, the same group exposed preterm rabbit delivered at 29 GA to 80% FiO2 for 11 days but observed similarly high mortality[162]. Richter et al.,[149] proposed a 7-days exposure protocol using preterm rabbits delivered at 28 GA and exposed to either hyperoxia (>95% FiO_2) or normoxia (21% FiO_2). After 7 days, mortality in the hyperoxia-exposed group was reported at 44%[149]. Since then, 7-days hyperoxia model has been widely used[163–168] and has been shown to reproduce key morphological, functional, and vascular features comparable to those observed in human BPD[87]. This model consistently demonstrates alveolar simplification and developmental arrest[149,164–166,169], increased collagen deposition[149,166,169], both histological and molecular sign of inflammation[149,163–166,169] and oxidative stress[163]. Functionally, lungs from hyperoxia-exposed pups exhibit reduced total lung capacity, decreased compliance, lower inspiratory capacity (IC), and increased tissue resistance (G) and elastance (H)[149,164–166,169]. Vascular alterations are also evident[164–166,168], along with signs of PH (decreased PAAT/PAET ratio)[164,165].

Recently, to better replicate oxygen exposure conditions reflective of current NICU practices and to enable longer-term follow-up, Catozzi et al. developed a preterm rabbit model delivered by C-section at 28 GA and exposed to 70% oxygen for 14 days[170]. After this period, they observed that prematurity alone, without additional BPD-related insults, was associated with impaired lung function and cardiovascular abnormalities. Exposure to 70% oxygen further exacerbated this BPD-like pulmonary phenotype[170].

Despite the reliability of the hyperoxia-exposed preterm rabbit in mimicking BPD, its use remains limited primarily due to the relative scarcity of antibodies, reagents and transgenic models, which hampers in-depth molecular and structural characterization of the model[87,150]. In particular, microstructural analysis of lung parenchyma is crucial to confirm the presence of the characteristic alterations associated with BPD, a key prerequisite for the effective use of this model in preclinical research.

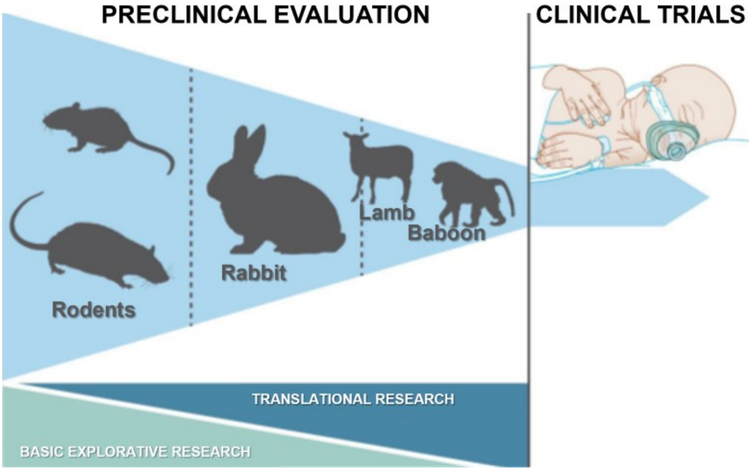

Figure 1.10 The preterm rabbit model represents a compromise between large and small animals. The preterm rabbit is a well-suited model for basic research with high translational potential. Image adapted from Salaets et al.[87]

1.5 Quantitative high-resolution imaging of the lung parenchyma

This paragraph presents a selection of key techniques for microstructural lung analysis, highlighting their application to the preterm rabbit model when available in literature.

1.5.1 Histological staining and immunolabelling: The gold standard

Lung parenchyma alterations are commonly assessed through classical histology, complemented by immunohistochemistry and/or immunofluorescence.

The histological workflow typically includes Hematoxylin and Eosin (H&E) staining, optionally combined with additional staining or immunolabelling of formalin-fixed, paraffin-embedded thin tissue sections. Image acquisition is performed via brightfield microscopy, followed by subsequent histological and stereological analysis. To assess alveolar development, metrics like RAC[171,172], Lm[173,174] and Mean Wall Intersection (Lmw)[173], are measured on H&E-stained sections[149,164,166,169]. In hyperoxia-exposed preterm rabbits, reduced RAC and increased Lm and Lmw indicate fewer, larger alveoli with thicker septa[149,164,166,169].

Vascular alterations are commonly assessed by measuring arterial media thickness (MT%)[173] on Miller or H&E-stained sections[164,166,175,176], and by evaluating vessels muscularization and microcirculation through immunolabeling with smooth muscle actin (αSMA) and cluster of differentiation 31 (CD31), respectively[166]. The hyperoxia-exposed preterm rabbit model exhibits increased arteries MT%, and muscularization, along with immature microcirculation[164,166,175]. Design-based stereological analysis, which estimates three-dimensional parameters from two-dimensional tissue sections, has further confirmed these alveolar and vascular impairments[165,168]. To assess inflammatory status, the Acute Lung Injury (ALI) score[177], is calculated on H&E-stained lung sections, revealing significantly higher values in hyperoxia-exposed rabbits compared to normoxia controls[164,166]. Finally, the content and the organization of collagen and elastin fibers are assessed by using Picrosirius Red (PSR) and Weigert's resorcin or orcein staining, respectively. Hyperoxia-exposed preterm rabbit shows an increased deposition and disorganization of collagen and elastin fibers[149,162,166,169].

For the high-resolution, relatively low-cost and accessible procedure, classical histology remains the gold standard for microstructural tissue analysis. However, it has some limitations: it requires specific samples preparation, multiple staining and it is destructive, requiring additional sections for subsequent procedures such as immunofluorescence[178]. Additionally, it provides only 2D imaging on thin tissue slices and it is not compatible with in-vivo or ex-vivo imaging.

Immunofluorescence is particularly useful for studying specific molecules; however, optimizing the protocols for rabbit models is challenging and time-consuming due to the limited availability and validation of commercial antibodies[87]. This restricts the analysis almost exclusively to the use of stains which may not always offer enough specificity and contrast for accurate quantification. Additionally, like histology, immunofluorescence is destructive and not compatible with in vivo or ex vivo imaging.

1.5.2 Micro-computed tomography (Micro-CT)

For non-destructive 3D structural analysis of the lung, micro-CT has recently been applied in hyperoxia-exposed preterm rabbits[164,170,179]. This non-invasive X-ray-based technique enables accurate 3D imaging and quantitative analysis of lung morphology[170]. Micro-CT systems acquire 2D X-ray projections, reconstruct them into cross-sectional slices, and generate high-resolution 3D models for volumetric and dimensional measurements[180]. Particularly suited for analyzing the bronchiolar tree and vasculature[181], micro-CT can, under certain conditions, also resolve alveolar structures. Applicable both in vivo and ex vivo[181], micro-CT's major advantage lies in its non-destructive nature, preserving specimens for further analyses like histology or molecular testing. Although highly informative, micro-CT lacks the resolution of traditional histology or immunofluorescence, making it insufficient for capturing cellular or subcellular details.

1.5.3 Transmission electron microscopy (TEM)

TEM provides ultrastructural detail far beyond the limits of optical microscopy by using an electron beam to examine fixed or cryo-preserved samples. Although, to the best of my knowledge, it has not been used to study hyperoxia-exposed preterm rabbits, it remains a valuable reference due to its critical contributions to pulmonary research. These include the identification of the continuous epithelial lining of alveolar septa[182], quantitative characterization of the human alveolar septal wall[183], and visualization of individual lipid lamellae within lamellar bodies of ATII cells[184]. TEM has also been applied in rabbits to investigate the ultrastructural development of respiratory acini[185]. Despite its strengths in microstructural analysis, TEM is limited by sample size and thickness constraints, which prevent a comprehensive overview of the lung parenchyma achievable with classical histology. Like histology and immunofluorescence, TEM cannot be used in vivo or ex vivo.

1.5.4 Two-photon excitation fluorescence microscopy

Two-photon excitation fluorescence (TPEF) microscopy, combined with second harmonic generation (SHG), has emerged as a powerful technique to overcome many of the classical histological limitations[186] while preserving the resolution and structural detail typical of standard histological methods[187]. This non-invasive, non-destructive, high-resolution method enables label-free imaging of tissue morphology, cellular components, and ECM structure[188] in vivo[189,190], ex vivo[191], and in fixed tissues[192]. TPEF exploits infrared light for imaging, reducing photodamage and increasing tissue penetration[193], which allows analysis of thick sections. It relies on endogenous fluorophores such as reduced nicotinamide adenine dinucleotide (Phosphate) [NAD(P)H], flavin adenine dinucleotide (FAD), elastin, and collagen[187], eliminating the need for external dyes and time-consuming procedure. SHG further enhances imaging contrast by detecting collagen-specific signals[194]. Additionally, fluorescence lifetime imaging microscopy (FLIM) adds molecular insights by mapping NAD(P)H fluorescence lifetime, a well-established sensitive indicator of cellular metabolic states and redox homeostasis[195–200].

Despite the potential of these optical label-free techniques, no studies have applied them to characterize the lungs of preterm rabbit exposed to hyperoxia condition.

2 - AIM OF THIS WORK

The aim of this work is to develop and validate a label-free, multimodal imaging strategy that combines TPEF, SHG, and FLIM to assess lung parenchyma alterations induced by hyperoxia exposure in preterm rabbits.

By detecting tissue intrinsic signals, including autofluorescence intensity and lifetime as well as SHG of collagen, this approach enables the simultaneous characterization of BPD-relevant features in a single section without the need for exogenous dyes.

This study introduces a non-destructive, high-resolution approach that integrates label-free imaging with conventional histology and immunolabelling in preclinical research, aiming to achieve a more comprehensive assessment of lung tissue.

3 – EXPERIMENTAL APPROACH

This chapter offers a concise overview of the principles underlying the label-free optical imaging modalities integrated into the multimodal tool developed in this work. It also includes experimental workflow, methods and materials.

3.1 Principles of label-free optical microscopy

3.1.1 Two-Photon Excitation Fluorescence microscopy and Second Harmonic Generation

Although the concept of two-photon excitation was first proposed by Maria Goeppert-Mayer in 1931[201], it was not experimentally demonstrated until 1961 by Kaiser and Garrett, following the invention of the laser[202]. The technique was later integrated with microscopy only in 1990, when Denk and colleagues reported for the first time its application to laser scanner fluorescence microscopy to study a biological sample[203]. Two-photon excitation involves the nearly simultaneous absorption (within ~10^{-18} seconds) of two photons, each carrying half the energy, and thus twice the wavelength, required for an electronic transition from the ground state to the excited state[188] **(Figure 3.1)**. Since this nonlinear excitation process is highly localized at the focal point, where the probability of simultaneous photons absorption is greatest, photodamage and phototoxicity to out-of-focus regions are significantly minimized. In addition, the use of infrared light, which undergoes less scattering in biological tissues, enables deeper penetration into samples[188]. The TPEF microscope is intrinsically confocal because fluorescence is generated only at the focal plane. The fluorescence emitted spectrum is identical to that produced under conventional one-photon excitation[204].

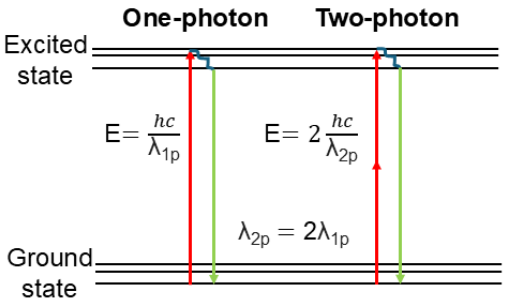

Figure 3.1 One photon vs two-photon excitation and emission principle. In one photon excitation, a fluorophore absorbs a photon to reach an excited state and emits light upon returning to the ground state. In two-photon excitation, two photons, each with half the energy of a corresponding single-photon, are absorbed “simultaneously” in a single event to reach the same excited state. Since photon energy is inversely related to wavelength, the excitation wavelength in two-photon absorption is approximately twice that of one-photon excitation.

TPEF microscopy has been widely employed for high-resolution imaging of cells and tissues. It relies on intensity contrast generated by endogenous auto-fluorescent biomarkers, such NAD(P)H, FAD, retinol, tryptophan, elastin, and collagen[187]. For a more comprehensive list, see **Table 3.1**.

Molecule	Process	λ_{ex} 50% max, nm*	Cross section
Tyrosine	3PE	<700	1×10^{-84}
Tryptophan	3PE	700–740	1×10^{-84}
Serotonin	3PE	700–720	4×10^{-84}
Melatonin	3PE	700–720	7×10^{-84}
5-HIAA	3PE	700–720	2×10^{-84}
5-HTOL	3PE	700–720	5×10^{-84}
Retinol	2PE	700–830	7×10^{-52}
Flavins	2PE	700–730	$1–8 \times 10^{-51}$
NADH	2PE	690–730	9×10^{-52}
Pyridoxine	2PE	690–710	8×10^{-53}
Folic acid	2PE	700–770	7×10^{-53}
Cholecalciferol	2PE	<700	6×10^{-54}
Elastin	2PE	700–740	—
NFTs	2PE	700–780	—
Lipofuscin	2PE	700–850	High‡
Collagen	SHG	700–740	—
Microtubules	SHG	—	—
Skel. muscle	SHG	—	—

Table 3.1 Multiphoton excitation characteristics of intrinsic emitters. Two-photon excitation (2PE)-action cross sections given for 700-nm excitation; units are cm^4s; Three-photon excitation (3PE) cross sections measured at 720 nm; units are cm^6s^2. *The Ti:S wavelength range where the cross section is 50% of the peak value. ‡Varies according to type. Adapted from Zipfel et al.[187]

Collagen can also be imaged with high contrast, specificity and sensitivity through SHG. SHG is a second-order nonlinear phenomenon in which two incident photons that simultaneously interact within a non-centrosymmetric material generate a photon with twice the energy and thus half the wavelength of the incoming photons[194] **(Figure 3.2)**. Since collagen has been shown to possess non-centrosymmetric properties[205], the SHG imaging technique has been widely used in combination with TPEF for collagen quantification in different organs and pathology, including the lung[206,207].

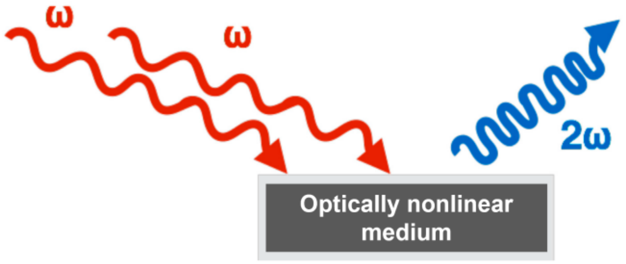

Figure 3.2 Schematic representation of the SHG phenomenon. SHG is a non-linear optical process, in which two incident photons interacting within a non-linear material (non-centrosymmetric) generate a new photon with twice the energy and therefore twice the frequency (2ω), or half the wavelength of the initial photons. Image adapted from Guidolin et al.,[194]

3.1.2 Fluorescence lifetime imaging microscopy

One limitation of endogenous biological fluorophores is the spectral overlap in their excitation and emission profiles, which hinders their discrimination when relying solely on fluorescence intensity (**Figure 3.3**).

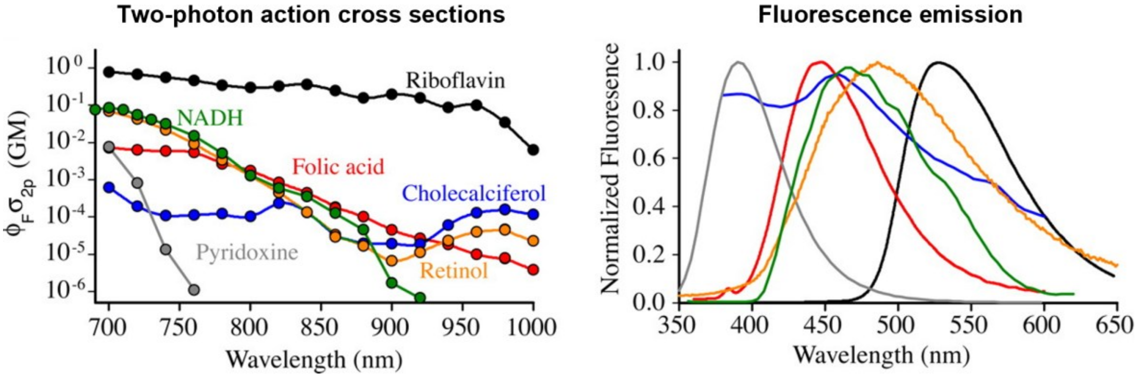

Figure 3.3 Two-photon absorption and emission spectra from a set of biological molecules. (left) Action cross sections (absorption cross section multiplied by the fluorescence quantum yield) of six molecules that contribute significantly to intracellular 2PE-excited intrinsic fluorescence. Units: 1 GM (Goppert-Mayer) equals 10^{-50}cm^4. All compounds were measured in buffered (pH 7.2) saline solution, except for retinol and cholecalciferol (Vit D), which were measured in EtOH. Riboflavin, cholecalciferol, and NADH were measured at 100 µM; retinol, folic acid, phylloquinone, pyridoxine and nicotinamide were measured at 500 µM. **(right)** Emission spectra of the compounds shown in the left image (measured in the same solvent). Image adapted from Zipfel et al.[187]

However, another property of fluorescence can be exploited to distinguish these molecules: the fluorescence lifetime[208] (**Figure 3.4**).

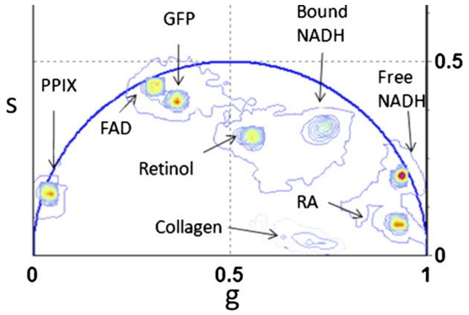

Figure 3.4 Phasor plot of relevant biological molecules. Phasor location of GFP, retinol in DMSO, retinoic acid (RA) in DMSO, FAD, free NADH, bound NADH with lactate dehydrogenase, and protoporphyrin IX (PPIX). Please note that the phasor location also depends on the environment in which the molecule is measured. Image adapted from Stringari et al.[197]

Fluorescence lifetime is defined as the time interval between the absorption of a photon and the subsequent emission of fluorescence[197]. In other words, it measures how long a fluorophore remains in the excited state before returning to the ground state by emitting a photon[208]. This parameter is intrinsic to the molecular structure of the fluorophore and is highly sensitive to its conformation and local microenvironment, including factors such as pH, ion concentration, and molecular interactions. Unlike fluorescence intensity, lifetime is largely independent of the concentration of the fluorophore[208,209].

Following the excitation, the fluorescence emission decays exponentially over time. Depending on the composition and heterogeneity of the fluorophore population, this decay can follow either a mono-exponential profile (for a single fluorescent species) or a multi-exponential profile (for two or more species).

The fluorescence decay is mathematically described by the following equation:

$$\mathrm{I(t)} = \sum_{i=1}^{n} \alpha_i \, e^{-t/\tau_i} \quad \textbf{[Eq. 3.1]}$$

where I(t) is the fluorescence intensity at time t, α_i represents the amplitude (or fractional contribution) of the i-th component, and τ_i is the corresponding fluorescence lifetime. The mean lifetime (τ_m) of a multiexponential mixture of species is the sum of the individual lifetimes (τ_i), weighted by the fractional contribution of each species (α_i)[208] (**Eq. 3.2**).

$$\tau_m = \sum_{i=1}^{n} \alpha_i \, \tau_i \quad \textbf{[Eq. 3.2]}$$

FLIM is an advanced imaging technique that generates contrast based on fluorescence lifetime, rather than fluorescence intensity. It can be integrated both with confocal microscopy and TPEF. FLIM measurements can be performed using two main acquisition approaches: time-domain and frequency-domain. Briefly, in time-domain techniques the sample is excited with a short pulse of light, and then the exponential decay of fluorescence is recorded either directly (i.e., by gated detection or pulse sampling) or using time-resolved electronics (i.e. Time-correlated single photon counting) that bin photons by their arrival times[208]. In contrast, in frequency domain technique, the sample is excited with a continuous light that is sinusoidally modulated at high frequencies. In this configuration, the emission occurs at the same frequency as the incident light, but it experiences a phase delay φ and a change in the amplitude M relative to the excitation light (demodulation) and from this information lifetime can be mathematically extracted.

Conventional FLIM is limited by its reliance on fluorescence decay curve fitting for data analysis. This approach requires assumptions about the number of exponential components, which are often problematic in complex biological samples and prone to bias. The fitting process involves iterative optimization of parameters to minimize the chi-squared (χ^2) goodness-of-fit, aiming for a value close to 1[208]. To address these limitations, Digman et al.[210] introduced the phasor approach, a fit-free method that transforms fluorescence decay profiles into a graphical representation on a phasor plot. This strategy is applicable to both time-domain and frequency-domain approaches[208], and enables intuitive, model-independent analysis of fluorescence lifetimes, minimizing interpretive bias.

3.1.2.1 FLIM phasor approach

Phasor analysis is a fit-free technique in which the fluorescence decay at each image pixel is transformed via Fourier analysis into a point in a two-dimensional space known as the phasor plot[208] (**Figure 3.5**). The coordinates of each point correspond to the real (G) and imaginary (S) components of the normalized Fourier transform of the decay function at that pixel. Consequently, each image pixel maps to a point in the phasor plot, and conversely, each cluster of points in the phasor plot represents a group of image pixels (**Figure 3.5**). A major advantage of the phasor approach is its ability to visually represent the molecular composition of an image without requiring any a priori assumptions. In phasor analysis, it is possible to select clusters of neighboring points, representing pixels with similar fluorescence lifetimes, using a colored cursor, and to map the corresponding pixels in the original image, even if they are spatially distant. These pixels are then highlighted in the image according to the color assigned to the cursor (**Figure 3.5**). In other words, by selecting regions in the phasor plot, one can generate a color-coded image in which different colors represent different fluorescence lifetime decays[211].

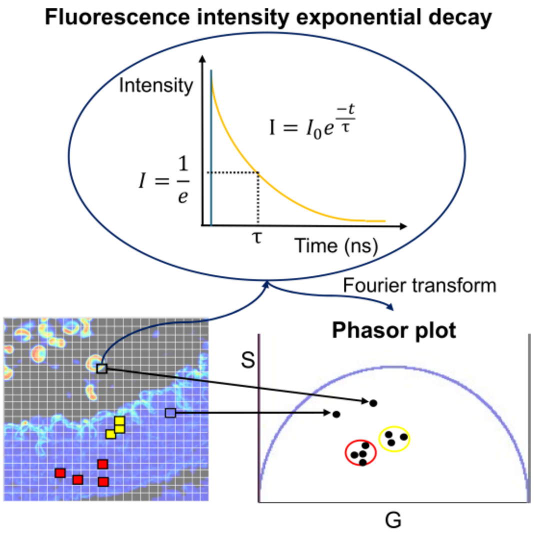

Figure 3.5 Phasor FLIM approach. Each pixel of the image (schematically represented by squares in the grid) is associated with a fluorescence intensity exponential decay, which is used in a Fourier transform to calculate the G and S coordinates of a point in the phasor plot. Each point can also be mapped back to a pixel in the image and highlighted according to the color of the cursor. I = Intensity; t = time; τ = fluorescence lifetime.

In the phasor plot, the coordinates reflect fluorescence lifetime: zero lifetime maps to (G=1, S=0), while infinite lifetime maps to (G=0, S=0) (**Figure 3.6 A**). Points on the left indicate longer lifetimes, and points on the right correspond to shorter lifetimes **(Figure 3.6 A)**. Mono-exponential decays lie on the universal semicircle, whereas multi-exponential decays fall inside it, with position reflecting intensity-weighted averages of individual mono-exponential decays lifetimes (**Figure 3.6 A**). For example, the phasor of a mixture of two species lies on a straight line connecting the phasor positions of the individual species on the universal circle[210] **(Figure 3.6 B**). The exact position along this line is determined by the relative fractional contributions of each species. Similarly, the phasor distribution of a mixture with three exponential components falls within the triangle defined by the phasor locations of the three pure species (**Figure 3.6 C**), and this geometric interpretation extends to higher-order mixtures as well[208].

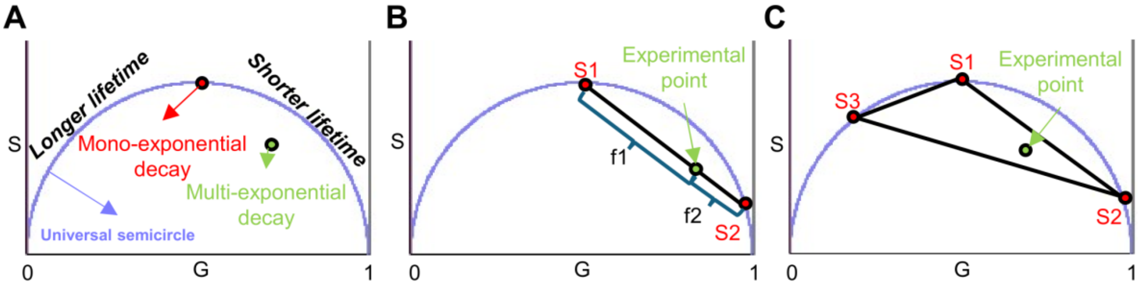

Figure 3.6 Phasor plot interpretation. (A) Points on the left side of the phasor plot correspond to pixels with longer fluorescence lifetimes, while those on the right correspond to shorter lifetimes. Mono-exponential decays generate points lying on the universal semicircle (the blue semicircle), whereas multi-exponential decays fall within it. **(B)** The phasor of a mixture of two species (S1, S2) lies on a straight line connecting the phasor positions of the individual species on the universal circle. The exact position along this line is determined by the relative fractional contributions (f_1, f_2) of each species, weighted by fluorescence intensity. **(C)** The phasor distribution of a mixture with three exponential components falls within the triangle defined by the phasor locations of the three pure species.

3.1.2.2 NAD(P)H autofluorescence lifetime

The redox couples $NAD(P)^+$/NAD(P)H are essential cofactors in cellular metabolism and redox homeostasis[212]. The NAD^+/NADH pair plays a central role in catabolic pathways, acting as an electron acceptor during glycolysis and as an electron donor in oxidative phosphorylation (OXPHOS)[197]. In contrast, the $NADP^+$/NADPH couple is primarily involved in anabolic processes and redox regulation, maintaining antioxidant systems such as glutathione and thioredoxin[213], and serving as a cofactor for NADPH oxidases which are major sources of ROS[214–216].

Unlike their oxidized forms, NADH and NADPH are intrinsically fluorescent, exhibiting similar broad emission spectra that peak near 460–470 nm[187], and are collectively referred to as NAD(P)H. Britton Chance first showed that the non-fluorescent NAD(P)+ allows NAD(P)H fluorescence intensity changes to directly reflect cellular redox state and metabolism[217,218] , leading to widespread use of NAD(P)H autofluorescence intensity to study metabolism and redox homeostasis[219,220]. However, the dependence of NAD(P)H intensity on fluorophore concentration led to growing interest in NAD(P)H fluorescence lifetime, which is independent of this factor and sensitive to molecular interactions and the microenvironment[208,221]. NAD(P)H exists in two forms with distinct lifetimes: free form with a short lifetime (~0.4 ns), and protein-bound form with a longer lifetime that varies depending on the specific binding partners[200]. A decrease in average lifetime and an increase of free/bound ratio have been associated with a more glycolytic metabolism[198], while an increase in lifetime and a decrease in free/bound ratio have been linked to enhance OXPHOS activity[222,223] (**Figure 3.7 A-B**).

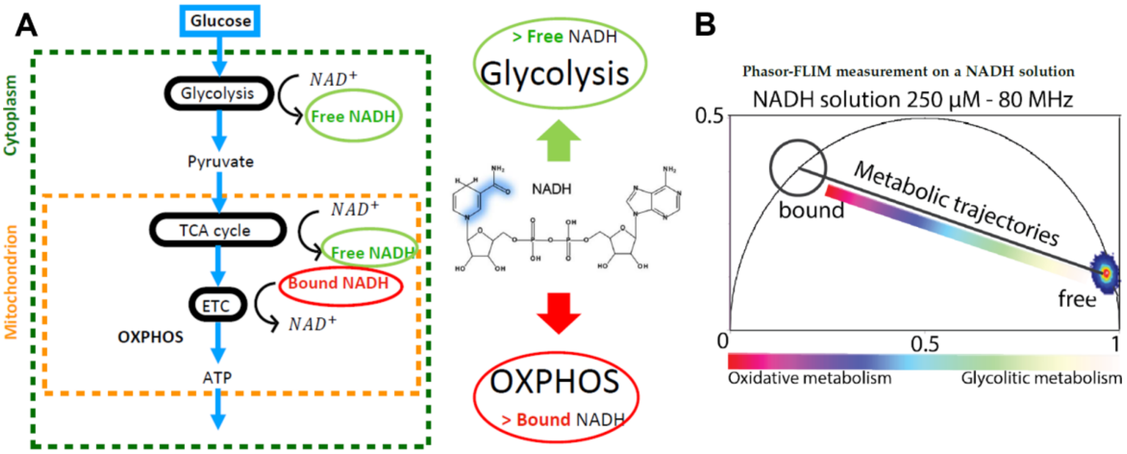

Figure 3.7 Ratio between free and bound NADH as a glucose metabolic indicator. (A) Conventionally, a shift toward free NADH is an indicator of increased glycolysis, while a shift toward bound NADH indicates increased OXPHOS. **(B)** In the phasor plot, the line joining NADH free and NADH bound is called "metabolic trajectory".

Although NAD(P)H FLIM measurements in cells, tissues, and in vivo have effectively revealed distinctive metabolic shifts[195–198,222,223], interpreting changes in NAD(P)H lifetimes solely within the glycolysis/OXPHOS framework can be an oversimplification in complex experimental settings (e.g., tissues, prolonged stimulation), which may require in-depth analysis. Such analysis is important to exclude contributions from ECM fluorescence[224], account for changes in the profile of NAD(P)H-binding enzymes[200], and consider the specific contribution of NADPH. While interpretation may require further biophysical investigation, any observed lifetime difference between conditions (e.g., treatment vs control) represents a powerful intrinsic marker for rapidly and reliably distinguishing them, as it reflects molecular and/or microenvironmental changes.

3.2 Experimental workflow

The experimental workflow, illustrated in **Figure 3.8**, is divided into two main phases: “Tool Development” (**Figure 3.8 a-d)** and “Tool Validation” **(Figure 3.8 e-f**). In the “Tool Development phase”, four key steps were performed:

a. **Sample collection**: Lung sections were collected from a well-established BPD model, specifically the preterm rabbit delivered at 28 GA and exposed either to 21% O_2 (Normoxia) or to 95% O_2 (Hyperoxia) for 7 days (**Figure 3.8 a**).
b. **Acquisition system setup**: A multi-channel acquisition system was set up to enable simultaneous visualization of lung parenchymal features by detecting tissue autofluorescence intensity and lifetime, as well as SHG upon TPEF (**Figure 3.8 b**).
c. **Features validation**: Each feature extracted from the acquired images was validated using conventional histological staining and immunolabeling techniques (**Figure 3.8 c**).
d. **Analysis system setup**: For each validated feature, an optimized protocol for analysis and quantification was established (**Figure 3.8 d**).

In the “Tool Validation phase”, two additional steps were performed:

e. **Comparison of features in BPD model:** The behavior of each feature was compared between normoxic and hyperoxic groups to evaluate the tool’s sensitivity in detecting hyperoxia-induced alterations (**Figure 3.8 e)**.
f. **Correlation analysis:** The reliability of the tool was evaluated by correlating label-free imaging features with corresponding H&E-derived histological parameters, and by further assessing the relationship between the severity of histological alterations and the severity of lung function impairments in individual animals (**Figure 3.8 f)**.

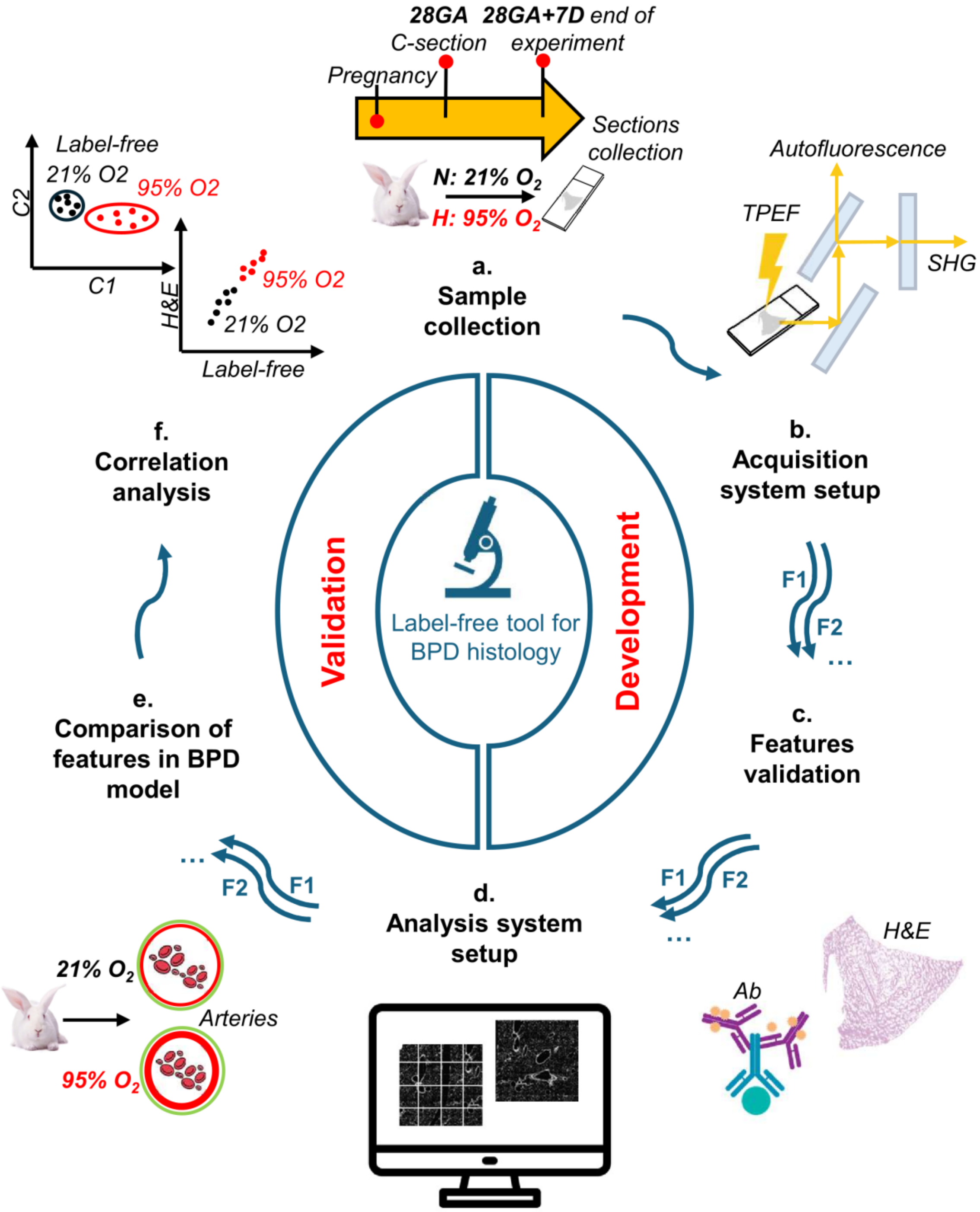

Figure 3.8 Experimental pipeline. The experimental workflow consists of two main phases: **(a-d)** the development of a quantitative, label-free tool for lung parenchyma tissue characterization and **(e-f)** its validation on lung sections from a well-established BPD model, specifically the preterm rabbits exposed for 7 days either to normoxia or hyperoxia. **(a)** Collection of lung sections from rabbits delivered at 28 GA and exposed for 7 days to either normoxia (N: 21% O_2) or hyperoxia (H: 95% O_2). **(b)** Design of a multichannel imaging system to enable the simultaneous visualization of BPD-relevant lung parenchymal features by detecting tissue autofluorescence intensity and lifetime, as well as SHG upon TPEF. **(c)** Validation of each label-free features (e.g., “F1”, “F2”) using standard staining or immunolabelling. “Ab”: antibodies. **(d)** Optimization of the analysis procedure for each feature (e.g., “F1”, “F2”). **(e)** Analysis of individual features (e.g., “F1”, “F2”) to distinguish normoxic from hyperoxic conditions in preterm rabbits. **(f)** Evaluation of the robustness of the tool's analysis and findings by correlating label-free features with corresponding measurements from H&E-stained sections, and by comparing the severity of histological changes with the severity of lung function impairments.

3.2.a Sample collection

The sample collection procedure is schematically summarized in **Figure 3.9**.

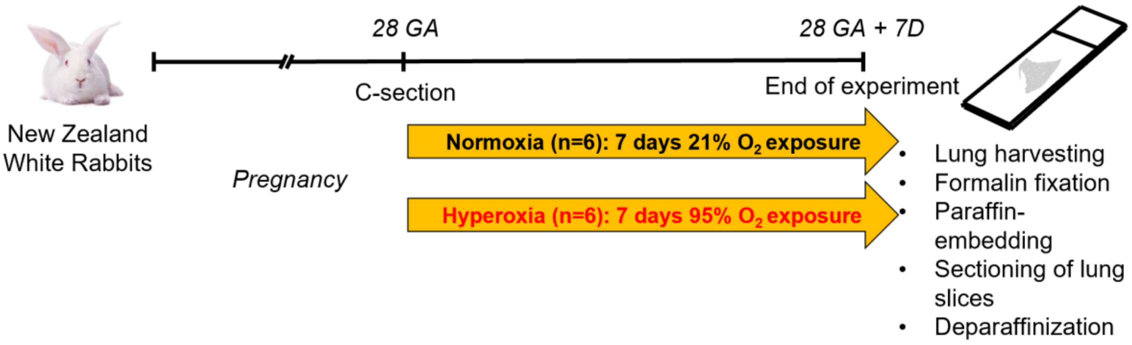

Figure 3.9 Sample collection. Lung sections were obtained from prematurely delivered rabbits at 28 GA (saccular stage) and subsequently exposed to either normoxic (21% O_2, n=6) or hyperoxic (95% O_2, n=6) conditions for 7 days. After the exposure period, lungs were harvested, fixed in formalin, embedded in paraffin, and sectioned. Prior to label-free imaging, paraffin was removed.

Animal care, delivery and experimental group

The experimental procedure was approved by the local animal ethics committee and complied with standard European regulations on animal research (n° 875/2021-PR). All animal procedures were conducted at Chiesi Farmaceutici, an AAALAC-accredited facility, by experienced personnel. Time-mated New Zealand White rabbits were obtained from Charles River Laboratories (Domaine des Oncins, France) and housed in Chiesi's animal facility under controlled conditions (15-21 °C, 55% ± 15% relative humidity, 12:12 h light/dark cycle), with food and water provided ad libitum until C-section. C-sections were performed at 28 GA (term at 31 GA, saccular stage) (**Figure 3.9**). Dams were sedated with intramuscular (i.m.) administration of medetomidine (2 mg/kg; Domitor®, Orion Pharma, Finland), followed after 10 min by ketamine (25 mg/kg; Imalgene 1000®, Merial, France) and xylazine (5 mg/kg; Rompun®, Bayer, Germany). Once adequate sedation was achieved, euthanasia was performed via an overdose of pentothal sodium (100 mg/kg; MSD Animal Health, USA). Immediately thereafter, a midline abdominal incision was made to open the abdominal cavity, the uterus was exposed, and all pups were delivered via hysterotomy.

Preterm pups were randomly assigned to two experimental groups: a normoxia group (n = 6), serving as the control, and exposed to 21% oxygen for seven days, and a hyperoxia group (n = 6), modeling severe BPD, exposed to 95% oxygen for seven days (**Figure 3.9**). Oxygen exposure was carried out in custom-designed incubators (Okolab, Italy) (**Figure 3.10**). Preterm pups remained in the incubator except for the feeding. Pups were fed twice daily via a 3.5 Fr orogastric tube (Vygon, France) with a milk replacer (Day One®, Protein 30%, Fat 50%; FoxValley, Illinois, US) dissolved in water (250 mg/mL). Probiotics (25 mg/mL, Bio-Lapis®; Probiotics International Ltd, UK) were added daily, whereas additional immunoglobulins (15 mg/mL, Col-o-Cat®, SanoBest, Netherlands) were only administered in the first two days. The feeding volume was stepwise increased from a total of 80 mL/kg/day on the day of birth to 200 mL/kg/day from day 3 to day 7. The temperature inside the incubators was maintained at 32 °C.

Figure 3.10 Custom-made incubators by Okolab. To replicate clinical conditions for preterm rabbit care, custom neonatal incubators were designed by Okolab (Naples, Italy). Positioned under a walk-in aspiration hood (Weiss Technik, Germany), each incubator consists of a rigid enclosure equipped with oxygen, nitrogen, and temperature sensors, along with a feedback control system to regulate and maintain internal oxygen concentration and temperature.

Lung section collection

At PND7 (**Figure 3.9**) pups were euthanized by an overdose of sodium pentothal prior to lungs harvesting. The lungs were removed en bloc, and a 14-gauge catheter was secured inside the trachea. The lungs were fixed with 10% buffered formalin (Sigma-Aldrich, Germany) for at least 4 h under constant pressure (25 cmH_2O). After that, the lungs were left in formalin for at least 24 h and then dehydrated in graded alcohol solutions, xylene clarified, and paraffin embedded. Dorsal serial sections 5 µm thick were selected at the same cutting depth for each animal using a rotary microtome.

Tissue deparaffinization

Paraffin was removed by immersing the collected 5µm-thick lung sections in xylene (Cat. 534056-4L, Sigma-Aldrich) for three washes of ten minutes each. Residual xylene was eliminated by sequential immersion of the slides in ethanol (EtOH) solutions: three washes in 100% EtOH, followed by one wash in 95% EtOH and one wash in 70% EtOH, each for five minutes. Ethanol was then removed by multiple washes in PBS. Lung sections were maintained in PBS until imaging.

3.2.b Development of a multimodal optical acquisition system

Lung sections were imaged using an Olympus FVMPE-RS microscope equipped with a two-photon Ti:sapphire laser (MaiTai HP, SpectraPhysics) operating at an 80-MHz repetition rate and an FLIMbox system (ISS, Urbana Champaign). Intrinsic tissue fluorescence and SHG signals from collagen were induced by excitation at 780 nm. Emission signals were collected simultaneously using a ×30 PlanApo silicon immersion objective (NA = 1.0) in the 470-570 nm range for autofluorescence intensity, in the 380-410 nm range for SHG and in the 420-460 nm range for autofluorescence lifetime (**Figure 3.11 A**). These emission ranges were selected to achieve distinct and biologically relevant contrasts: the 470-570 nm band was chosen to broadly capture signals from multiple endogenous fluorophores providing a comprehensive representation of lung parenchyma autofluorescence[187]; the 380-410 nm range, centered at half the excitation wavelength, was optimized to specifically isolate the SHG signal from collagen while minimizing interference from autofluorescence[194]; and the 420-460 nm window was selected to predominantly detect the fluorescence lifetime contribution of NAD(P)H[196,225].

Intensity contrast images (Autofluorescence intensity and SHG) were acquired with 2.0% laser power (2.90 W), using a 450 V detector for autofluorescence and a 720 V detector for SHG. To minimize scanning time, while ensuring representative sampling, ten mosaics (2.7 mm^2 each) were randomly acquired from each lung section (**Figure 3.11 B left**). Each mosaic comprised sixteen 1024×1024-pixel images (scan speed: 10 µs/pixel), which were automatically stitched using the Olympus FV31S-SW FLUOVIEW software. No digital zoom was applied, and the signal-to-noise ratio (SNR) was enhanced by averaging two frames.

The lifetime-based contrast acquisition protocol consisted of acquiring 10 additional randomly distributed regions within the lung parenchyma at 6x magnification (**Figure 3.11 B right**). The ten 512×512-pixel images (scan speed: 12 µs/pixel) were acquired using 0.4%-0.8% laser power (2.90 W) and a detector voltage of 850 V. FLIM data were collected until a minimum of 10^5 counts per pixel were obtained within the region of interest. Calibration of the ISS FLIMbox system was performed using the known mono-exponential lifetime decay of fluorescein at pH 11.0 (4.0 ns upon excitation at 780 nm, collection range: 572-642 nm). Calibration samples were prepared by diluting a 100 mmol/L fluorescein stock solution in EtOH (1:2000) with 0.1 M NaOH (pH 11.0) prior to each session.

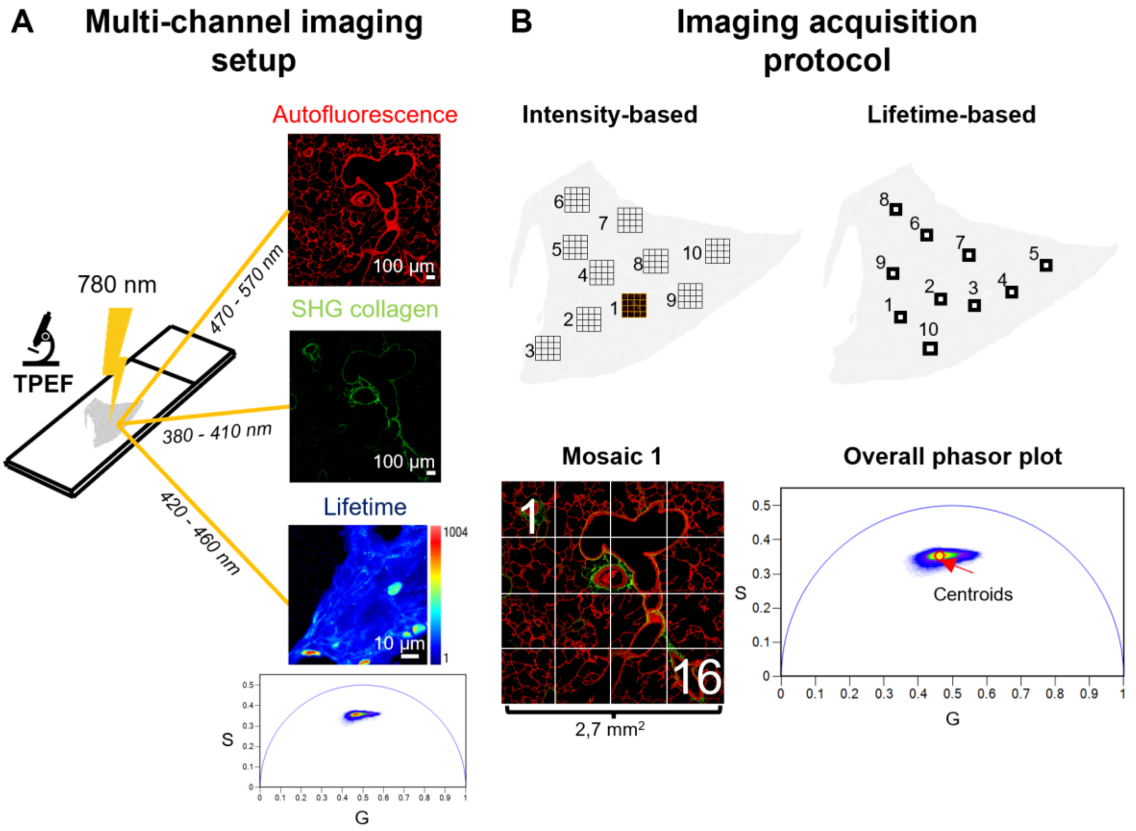

Figure 3.11 Acquisition system setup. (A) TPEF of lung sections was performed at 780 nm, with simultaneous acquisition of autofluorescence intensity in the 470-570 nm range, SHG of collagen in the 380-410 nm range, and autofluorescence lifetime in the 420-460 nm range, using an optimized multichannel acquisition system. **(B left)** The optimized acquisition protocol for autofluorescence intensity and SHG involved random acquisition of 10 mosaics (each covering 2.71 mm²) per lung slice, with 16 frames per mosaic. (**B right**) The optimized acquisition protocol for autofluorescence lifetime consisted of ten randomly distributed regions within each lung section. The centroid (yellow point) of the phasor plot, derived from the pixels of the ten images, represents the sample's lifetime signature in the 420-460 nm range. Please note: the images are from real experiments. SHG images are presented after autofluorescence subtraction as detailed in section 3.2 d "density of total and parenchymal collagen %"

3.2.c Features validation

To characterize the lung parenchyma, both the separate and combined analysis of autofluorescence and SHG signals were exploited. Autofluorescence revealed the morphology of the lung parenchyma, distinctive alveolar architecture and the possible presence of inflammatory alveolar exudates, while SHG selectively detected collagen fibers deposition. The integration of these signals also facilitated the identification of vascular structures and their layers. Additional insights were obtained by analyzing the intensity and lifetime of autofluorescence.

To validate the reliability of the extracted features, the non-destructive nature of label-free optical imaging was exploited. During image acquisition, x, y, and z coordinates were recorded to enable precise re-localization of the same regions. The sections were subsequently stained using conventional histological or immunofluorescence techniques and re-imaged. (**Figure 3.12**). H&E-staining was used to confirm the correspondence between autofluorescence signals and parenchymal structure. Collagen distribution identified via SHG was verified using PSR staining. Vascular features were confirmed through immunolabeling with antibodies against α-SMA and CD31/PECAM-1, targeting smooth muscle cells in the tunica media and endothelial cells in the tunica intima, respectively.

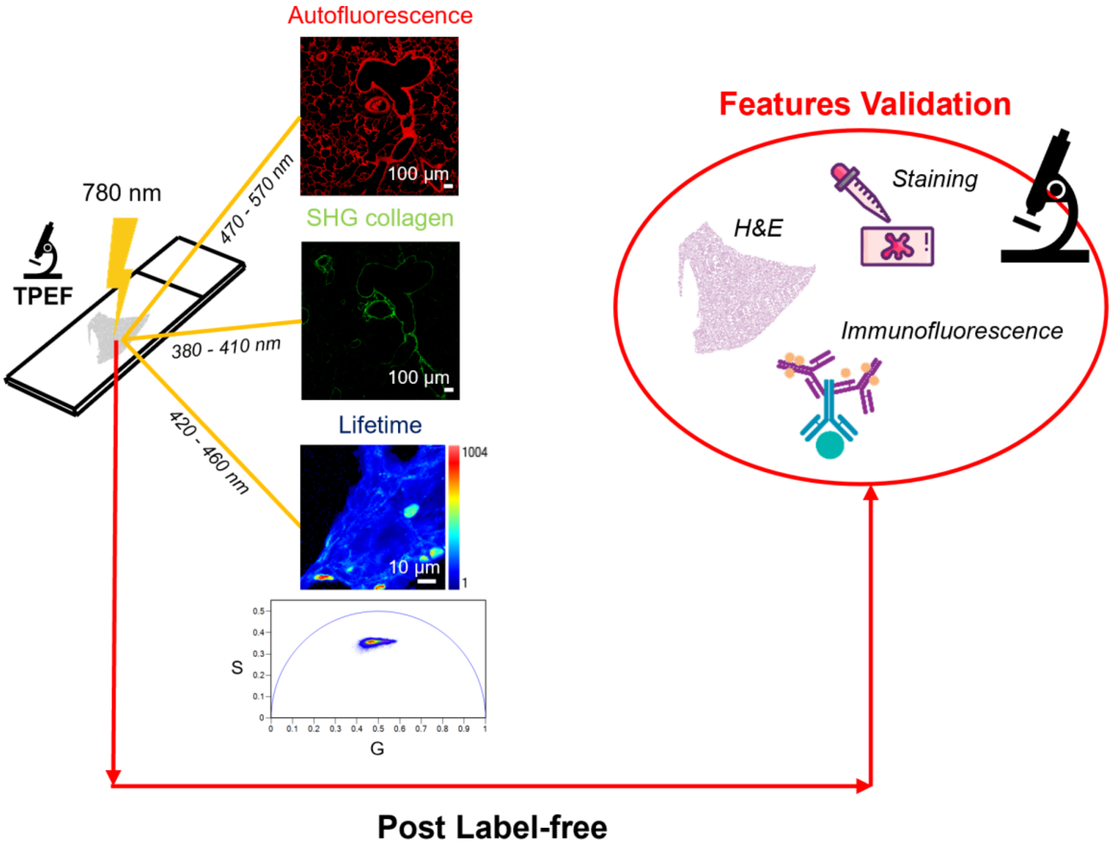

Figure 3.12 Features validation. Label-free acquired sections may be subsequently stained or immunolabeled to validate the observations.

Hematoxylin and eosin staining

Lung sections were stained with H&E according to the manufacturer's specifications (Histo-Line Laboratories). Histological slides were acquired as whole slide images by digital slide scanner (Nanozoomer S-60, Hamamatsu, Japan).

Picrosirius red staining

For collagen evaluation, lung sections were stained with PSR and imaged using either brighfield microscopy or two-photon microscopy for fluorescence detection. Slides were incubated for 1 hour in a PSR staining solution containing 0.5 g of Direct Red 80 (Cat. 2610-10-8, Sigma-Aldrich, St. Louis, MO) dissolved in 500 mL of saturated picric acid (Cat. P6744-1GA, Sigma-Aldrich, St. Louis, MO). Following incubation, slides were washed twice with acidified water (0.5% acetic acid) and then dehydrated through a graded ethanol series (70%, 90%, 95%, and 100%). Residual ethanol was removed by two washes in xylene. Sections were mounted using DPX mounting medium (Thermo Scientific™) and imaged with a TPEF microscope. Excitation was performed at 1000 nm, and PSR signals were collected in the 505-680 nm range.

Immunofluorescence

Optimized staining protocols and acquisition settings were developed for each antibody. For α-SMA (Goat polyclonal alpha smooth muscle actin, Abcam, ab21027) immunofluorescence, antigen retrieval was performed by incubating slides in 25 mM tris(hydroxymethyl)aminomethane hydrochloride (Tris-HCl) buffer (pH 8.5) containing 1 mM ethylenediaminetetraacetic acid (EDTA) and 0.05% sodium dodecyl sulfate (SDS) at 95 °C for 10 min, followed by cooling at room temperature (RT) for 30 min and three washes in distilled water. Samples were permeabilized in 0.1% Triton X-100 in PBS (PBST) for 30-45 min at RT. Slides were then incubated overnight (ON) at 4 °C with the primary antibody diluted 1:200 in PBST. After three 10-min washes in PBST at 37 °C, sections were incubated for 1 h at RT with Alexa Fluor 488-conjugated chicken anti-goat secondary antibody A-21467, Thermo Fisher diluted 1:1000 in PBST. Excess antibody was removed by three final washes. Imaging was performed using TPEF with excitation at 760 nm, and emission was collected between 380–570 nm.

For CD31 (mouse monoclonal anti-CD31/PECAM-1, sc-376764, Santa Cruz), antigen retrieval was carried out using 0.01 M citrate buffer (pH 6.0) with five microwave cycles (5 min each at 750 W), followed by cooling for 30 min. After PBS washes, slides were blocked for 1 h in 3% bovine serum albumin (BSA) in PBS and incubated ON at 4 °C with the primary antibody diluted 1:600 in 3% BSA. The following day, after PBS washes, slides were incubated for 1h at RT with Alexa Fluor 555-conjugated donkey anti-mouse secondary antibody A-322773, Thermo Fisher diluted 1:1000 in 3% BSA. After additional washes and 5 min blocking in H_20, slides were incubated with DAPI for nuclear staining. A final wash was performed before imaging. Imaging was performed using a confocal microscope Stellaris 8 (Leica Microsystems, Germany). DAPI was excited at

405 nm and detected between 425-470 nm; Alexa Fluor 555 was excited at 553 nm and detected between 560-700 nm.

SHG test

SHG signals can be detected exclusively within an emission range corresponding to half the illumination wavelength. To validate SHG specificity, lung slices were excited at 720 nm, 780 nm, and 840 nm. Emission signals were collected in the 380-410 nm range to selectively isolate SHG signals and in the 470-680 nm range to capture autofluorescence signals. True SHG signals were defined as those present in the 380-410 nm range when excited at 780 nm but absent when excited at 720 nm or 840 nm, ensuring the exclusion of autofluorescence artifacts.

3.2.d Analysis system

For each extracted and validated feature listed below, a manual or semi-automated analysis protocol was optimized using ImageJ/Fiji[226]. The optimization was carried out on both normoxic and hyperoxic lung tissues and the analysis was performed on the 10 acquired mosaics for each sample.

Density of alveolar exudates %

Alveolar exudates were measured as a potential histological sign of inflammation. Alveolar exudates were quantified using the autofluorescence channel. Areas of exudates accumulation within the alveolar spaces were manually delineated, and their total area was calculated. This area was subsequently normalized to the total mosaic area according to the following formula:

$$Density\ of\ alveolar\ exudates\ (\%) = \frac{Alveolar\ exudates\ area}{Mosaic\ area} \times 100 \quad \textbf{[Eq. 3.3]}$$

Tissue density (TD) %

Tissue area was quantified by applying a Huang threshold-based mask[227] to the autofluorescence (“AF”) channel for tissue segmentation. To focus exclusively on tissue architecture, areas corresponding to alveolar exudates were excluded from the total autofluorescence-positive area. The resulting tissue area was then normalized to the acquisition area using the following formula:

$$TD\ (\%) = \frac{(AF\ area - Alveolar\ exudates\ area)}{Mosaic\ area} \times 100 \quad \textbf{[Eq. 3.4]}$$

Tissue autofluorescence intensity

Autofluorescence intensity was quantified in tissue segments. Tissue selection was performed using a HUANG threshold-based mask[227] applied to the autofluorescence channel (“AF”). The average tissue intensity was then normalized to the background intensity using the following formula:

$$Tissue\ autofluorescence\ intensity\ = \frac{Tissue\ AF\ intensity}{Background\ AF}\quad [\mathbf{Eq.\ 3.5}]$$

Density of total and parenchymal collagen %

Fibrillar collagen was assessed using the SHG channel. To eliminate background noise caused by autofluorescence bleed-through emitted by spot-like structures and red blood cells (RBCs), the autofluorescence signal was subtracted, ensuring that only pixels exhibiting a true SHG signal were retained for collagen analysis. Quantification was carried out by applying the "Frangi vesselness filter"[228], version "imglib, experimental", available in ImageJ Fiji[226]. Originally designed as a vessel enhancement filter, the Frangi filter has also been successfully employed to detect tubular structures such as collagen fibers[229]. Filter parameters were optimized through iterative testing of multiple settings and evaluating their performance on our images. The final parameters selected were number of scales = 1, minimum scale = 0.9, and maximum scale = 5. Otsu's thresholding method was then applied to segment fiber-occupied areas. Collagen-occupied area was subsequently normalized to the mosaic area using the following formula:

$$Total\ collagen\ (\%) = \frac{Area\ SHG\ collagen}{Mosaic\ area} \times 100\quad [\mathbf{Eq.\ 3.6}]$$

To selectively identify collagen in the alveolar septa and interstitial spaces, four regions of interest (ROIs) of 0.237 mm² were selected within each mosaic using the autofluorescence channel to avoid airways and muscularized vessels, and to minimize selection bias. Frangi filters and Otsu's thresholding method were then applied to the corresponding regions in SHG channels. The collagen-occupied area was subsequently normalized to the ROI area using the following formula:

$$Parenchymal\ collagen\ (\%) = \frac{Area\ SHG\ collagen}{ROI\ area} \times 100\quad [\mathbf{Eq.\ 3.7}]$$

Arterial media thickness (MT) % and arterial adventitia thickness (ADVT) %

MT% and ADVT% were evaluated by combining the SHG and autofluorescence channels. The MT% assessment was performed by adapting a previously described method for H&E-stained sections[176]. For each animal, ten muscularized vessels corresponding to pre- and intracinar arteries, with an external short-side diameter between 50 μm and 100 μm, were selected from the mosaics. MT% was calculated by measuring the external short-side diameter excluding SHG signals (ED), and the internal short-side diameter (ID), which included only the lumen (**Figure 3.13**), using the following formula[173]:

$$MT\ (\%) = \frac{(ED - ID)}{ED} \quad \textbf{[Eq. 3.8]}$$

This proportional parameter nullifies the effect of vasodilation, vasoconstriction, and tissue shrinkage[173].

ADVT% was determined by measuring the external short-side diameter including SHG signals (AED) and using the previously measured ED as the internal diameter, which encompasses both the lumen and internal layers (**Figure 3.13**), applying the following formula:

$$ADVT\ (\%) = \frac{AED - ED}{AED} \times 100 \quad \textbf{[Eq. 3.9]}$$

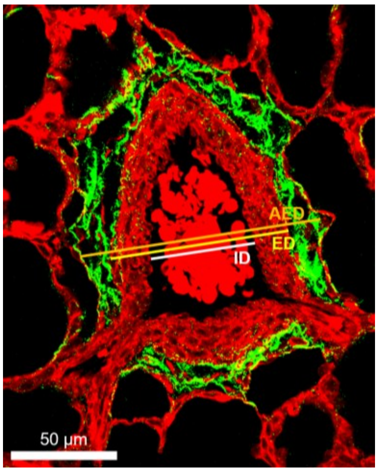

Figure 3.13 Representative image of the diameter tracking method for MT% and ADVT% calculations. The Adventitia External diameter (AED) corresponds with the external short side diameter including SHG (orange line); the ED with the external short side diameter excluding SHG (yellow line); and the ID with the internal short side diameter (white line). Notably, image is from a real experiment and SHG is reported after autofluorescence subtraction as detailed in section 3.2 d "density of total and parenchymal collagen %"

Alveolar density

A region of interest (ROI) of 0.866 mm^2 was selected in a central position of each mosaic to manually count all enclosed surfaces, excluding airways, vessels, and alveolar sacs, while including individual alveoli, thus providing an approximation of the alveolar count (**Figure 3.14**). These excluded structures were recognized based on their morphology and their distinctive SHG collagen signal (**Figure 3.14**). The number of alveoli was then normalized by ROI area and a multiplicative factor of 10^4 was applied to facilitate data interpretation, given the small absolute values resulting from the normalization. The formula was the following:

$$\text{Alveolar density} = \frac{\text{Count of enclosed surfaces}*}{\text{ROI area}} \times 10^4 \quad [\textbf{Eq. 3.10}]$$

*No airways, vessels and alveolar sacs

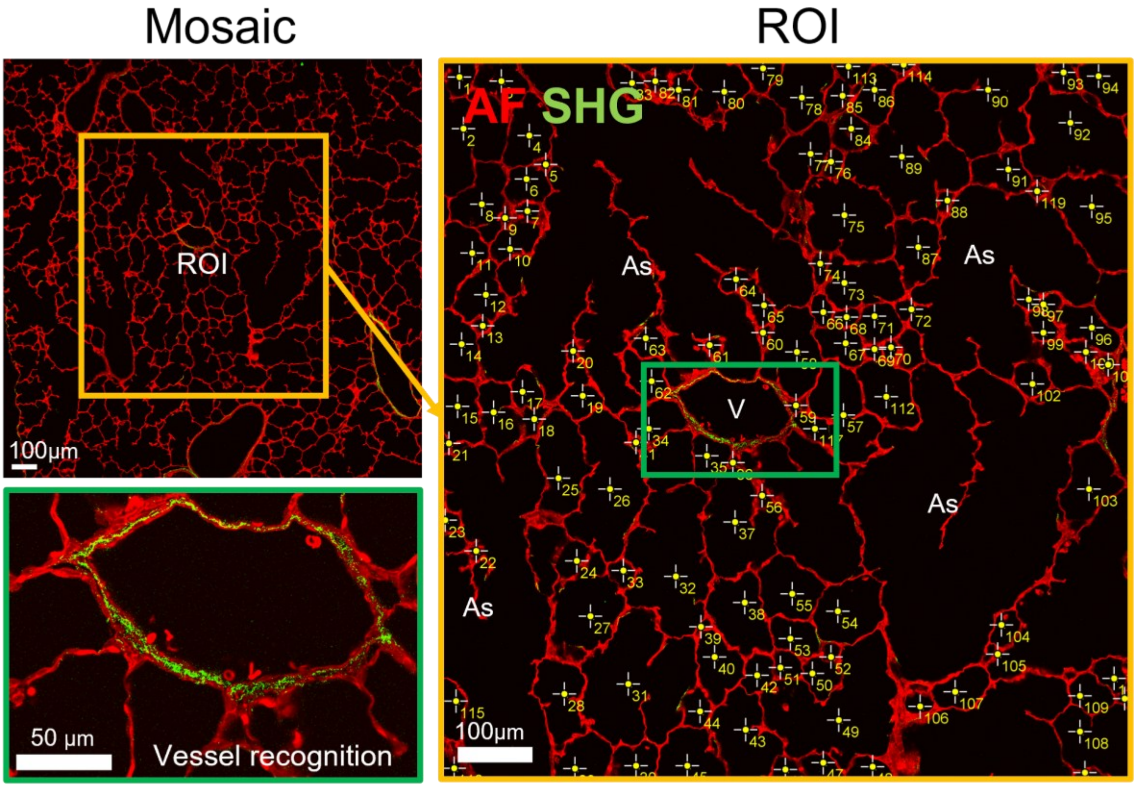

Figure 3.14 Representative image of alveolar density analysis. "As" alveolar sac; "V" Vessel. Notably, the images are from real experiments. SHG images are presented after autofluorescence subtraction as detailed in section 3.2 d "density of total and parenchymal collagen %"

Autofluorescence lifetime

Autofluorescence lifetime analysis was performed using the phasor-FLIM approach (for more details, refer to 3.1.2.1), with the SimFCS v. 4.0 software (Laboratory for Fluorescence Dynamics, University of California, Irvine). A cluster of points in the phasor plot, each corresponding to image pixels, was obtained from all the ten images acquired for each animal. The centroids of these clusters were calculated and averaged to obtain a mean centroid per animal. Only the G coordinates of these centroids were considered because no significant shift in S was detected.

3.2.e-f Comparison of feature behavior in normoxia and hyperoxia and correlation analysis

The behavior of each feature was analyzed in both normoxic and hyperoxic lung sections to investigate hyperoxia-induced alterations. To further validate the proposed imaging approach, its sensitivity was assessed through a series of analyses. First, label-free histomorphological readouts were correlated with established quantitative metrics, including the RAC, ALI score, and the MT% of arteries, measured on H&E-stained sections of the same animals. In addition, SHG-detected fibrillar collagen was qualitatively compared with that revealed by Col1a1 immunohistochemistry (IHC). Subsequently, Principal Component Analysis (PCA) was applied to evaluate the tool's ability to discriminate between hyperoxic and normoxic animals based on the complete set of features extracted from individual image mosaics. These included TD, tissue autofluorescence intensity, alveolar exudates, parenchymal fibrillar collagen content, MT%, alveolar density, and autofluorescence lifetime. Finally, the correlation between the extent of structural damage and functional impairment was investigated. Lung function was assessed in vivo using FlexiVent measurements prior to tissue harvesting, considering the following parameters: inspiratory capacity (IC), tissue damping (G), tissue elastance (H), and static compliance (Cst).

Histomorphometry

Histomorphometrical analyses were conducted on H&E-stained sections, including RAC, arterial MT%, and ALI score.

RAC was determined by drawing a perpendicular line from the lumen of a terminal bronchiole to the nearest connective tissue septum or pleural surface, and counting the number of alveoli or saccules intersected along this line[171,172]. Ten counts were performed per lobe (20 measurements in total) and the average between the right and left lung was considered.

For the evaluation of MT%, 10 random peripheric muscularized vessels with external diameter (ED) <100 µm, corresponding in rabbits to the pre- and intra-acinar arteries, were selected per section. Their external (ED) and internal diameter (ID) along the shortest axis of the vessel were measured at 40x magnification and MT% was calculated by applying the following formula[173]:

$$MT\% = \frac{(ED-ID)}{ED} \quad \textbf{[Eq. 3.11]}$$

This proportional parameter nullifies the effect of vasodilation, vasoconstriction, and tissue shrinkage[173].

The ALI score was evaluated according to the criteria defined by the American Thoracic Society[177]. The assessment method relies on five distinct histological features: neutrophil infiltration in the alveolar spaces, neutrophils in the interstitial spaces, the presence of hyaline membranes, proteinaceous debris within the airspaces, and thickening of the alveolar septa. For each animal, a minimum of 20 randomly selected high-power fields (400× total magnification), ten per lung lobe, were independently evaluated in a blinded manner. Field selection was performed by applying successive random displacements in both the x and y axes from the current position, ensuring a minimum separation of one high-power field between sampled areas and a uniform sampling of the tissue. Only fields with ≥ 50% alveolar structures were included, while those dominated by large airways or vessels were excluded. To calculate the ALI score, the values of the five histological parameters were weighted, summed, and then normalized to the total number of fields assessed[177]. The resulting ALI score was expressed as a continuous variable ranging from 0 to 1. The mean ALI score derived from the right and left lungs was computed and used in the analysis.

Immunohistochemistry

IHC was performed using a fully automated stainer (Leica BOND RX, Leica Biosystems) (**Figure 3.15**) equipped with the BOND Intense R Detection System (DS9263), a peroxidase-based kit designed for immunostaining visualization with this automated platform. This kit includes a peroxide block, streptavidin conjugated to horseradish peroxidase (HRP), 3,3'-diaminobenzidine (DAB) as chromogen and hematoxylin. Lung sections were deparaffinized using BOND Dewax Solution (AR9222) at 72 °C and rehydrated through a graded ethanol series. Heat-induced antigen retrieval was carried out at 95 °C for 20 minutes in citrate buffer (pH 6.0; Epitope Retrieval 1-ER 1, AR9961). Slides were incubated for 10 minutes with peroxide block (Leica Biosystems), followed by 1 hour in 1:10 goat serum diluted in PBST to block endogenous peroxidase and secondary antibody unspecific binding, respectively. Sections were then incubated for 1 hour at RT with a mouse monoclonal anti-Col1a1 antibody (MA1-26671, 1:500 in goat serum). For the detection, lung slices were incubated for 30 min with biotinylated goat anti-mouse BP-9200-500, followed by 30-minute incubation with streptavidin-HRP. The reaction was visualized by using DAB.

Figure 3.15 Leica BOND RX, Leica Biosystems.

Principal component analysis (PCA)

PCA was performed on MATLAB, by means of the built-in function providing the principal components, explained variances, and scores. The results were analyzed to understand variance contributions, and scatterplots were generated for visualization. Confidence ellipsoids were calculated using the eigenvalues and eigenvectors of a covariance matrix in MATLAB. The eigenvalues define the axes' lengths, while the eigenvectors determine their orientation in space. This representation visualizes uncertainty in multivariate data by scaling the ellipsoid according to the confidence level.

Lung function measurements

At PND7 invasive lung function testing was performed on preterm rabbits using the forced oscillation technique with the flexiVent™ apparatus equipped with module 2 (SCIREQ, Canada) (**Figure 3.16)**. Animals were initially anesthetized with ketamine (35 mg/kg) and xylazine (5 mg/kg) i.m. A tracheostomy was then performed with a 14-gauge metal needle, and the pups were connected to the volume-controlled mechanical ventilation of the flexiVent™ (tidal volume [V_T] 10 mL/kg, breath rate [BR] 120 breaths/min, positive end-expiratory pressure [PEEP] of 3 cmH_2O). The lung function parameters IC, G, H and C_{st} were determined. G and H were measured using the Primewave-8 forced oscillation, whereas C_{st} was determined using the pressure-volume curve. All measurements were performed until three consistent measurements were obtained, with a coefficient of determination > 0.95 as the limit to accept the measurement. The average of three measurements was calculated and used in the analysis. The values of IC and Cst were then normalized according to the weight.

Figure 3.16 FlexiVent™

Statistical analysis

Statistical analysis was performed using GraphPad Prism (GraphPad 8.0.1, San Diego, CA, USA). Normality tests were performed with Shapiro-Wilk, variance tests with test F and outliers' identifications with ROUTE method (Q = 1%). Information on the statistical test used is provided in the description of each figure and it was selected based on the data distribution and variance. Correlation tests were performed using Person or Spearman tests depending on whether the variables were normally distributed or not. For linear regression analysis, regression coefficients and goodness of fit (R^2) were reported. Levels of significance used: ns = $p > 0,05$, * $p \leq 0,05$, ** $p \leq 0,01$, *** $p \leq 0,001$, **** $p \leq 0,0001$.

4 - RESULTS

4.1 The multichannel imaging approach allows the simultaneous visualization of lung parenchymal features relevant for BPD

As illustrated in **Figure 4.1**, by detecting autofluorescence intensity (470-570 nm) and lifetime (420-460 nm), as well as SHG signals (380-410 nm), the multichannel imaging tool enabled the simultaneous analysis of multiple features relevant to BPD within a single mosaic, without the need for external dyes. Autofluorescence intensity-based contrast allowed the evaluation of tissue morphology, tissue density and alveolar exudates, the latter representing a potential biomarker of inflammation (**Figure 4.1 A**). Moreover, since autofluorescence reflects tissue molecular composition, changes in its intensity may serve as intrinsic markers of disease state[187] **(Figure 4.1 A)**. SHG, on the other hand, enabled the detection of fibrillar collagen deposition, thus allowing the evaluation of fibrotic changes (**Figure 4.1 A**). Additionally, the combined use of autofluorescence and SHG enabled the assessment of both alveolar and vascular impairments **(Figure 4.1 A).** In parallel, autofluorescence lifetime-based contrast, like intensity, represents another intrinsic marker of disease state and may offer preliminary insights into tissue metabolism and redox homeostasis **(Figure 4.1.B)**. Each of these features will be explored in detail in the following paragraphs.

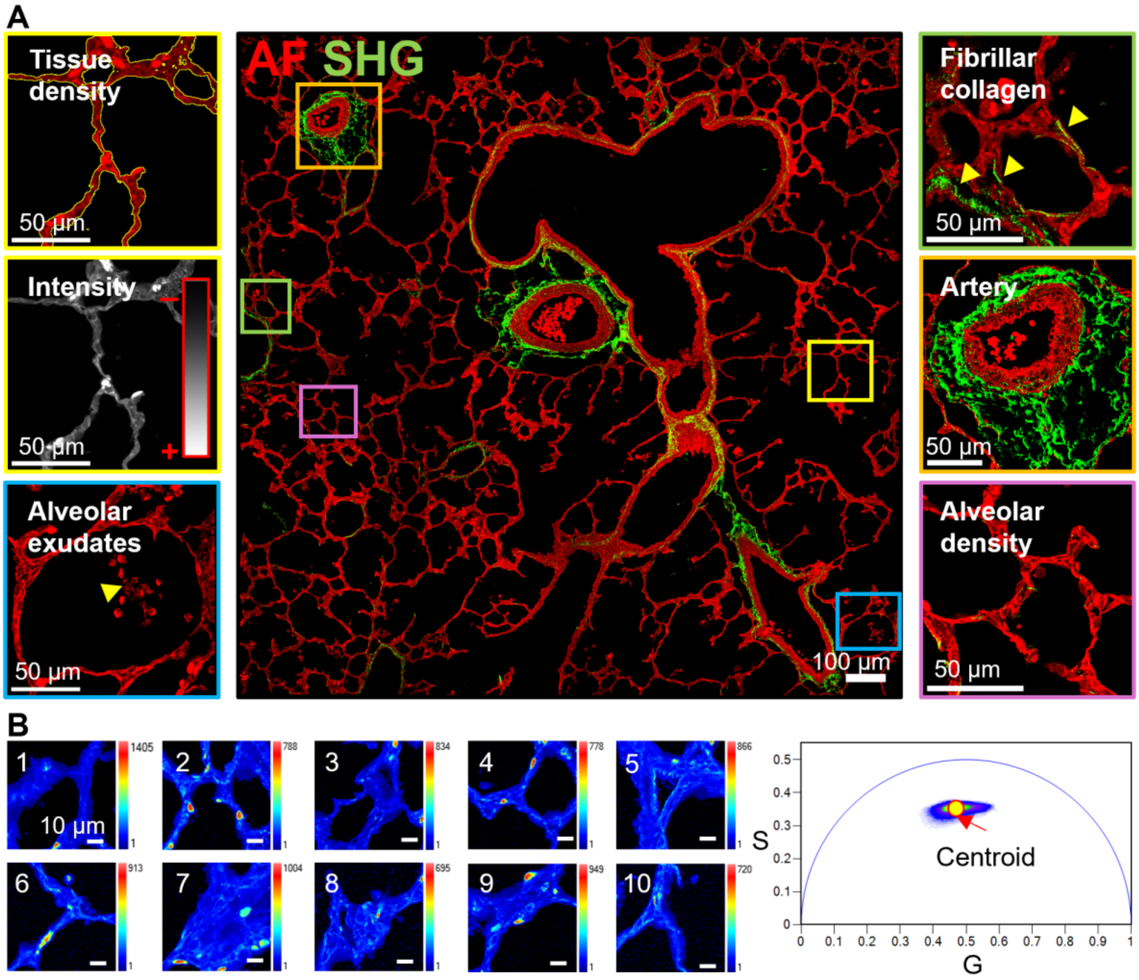

Figure 4.1 Multichannel imaging system allows the simultaneous visualization of lung parenchymal features relevant to BPD in tissue sections from preterm rabbit. (A) Representative image showing all features that can be simultaneously analyzed in each mosaic using autofluorescence (red signal) and SHG imaging (green signal). These signals were collected in the 470-570 nm and in the 380-410 nm ranges, respectively, and originated from TPEF of the tissue at 780 nm. The analyzable features include tissue density and intensity of its autofluorescence (yellow boxes), alveolar exudates (light blue box, indicated by arrowhead), fibrillar collagen (green box, indicated by arrowheads), arteries with their layers (orange box), and alveolar density (pink box). Images of SHG signal were presented after autofluorescence subtraction as detailed in “density of total and parenchymal collagen %, section 3.2 d”. **(B)** Ten additional randomly distributed regions within the same lung sections were selected for autofluorescence lifetime measurement in the 420-460 nm range. Representative FLIM images of the ten regions depicted the distribution of fluorescence intensity **(left)** with each pixel having a corresponding point in their phasor plot **(right)**. The resulting cluster centroid represented the sample's lifetime signature in the 420-460 nm range.

4.2 Features based on autofluorescence intensity contrast: alveolar exudates area, tissue density and autofluorescence intensity modulation

Lung parenchymal development and signs of inflammation are conventionally evaluated using H&E-stained tissue sections[149,164,176], which provide detailed visualization of tissue architecture and cellular components. Autofluorescence imaging within the 470-570 nm range demonstrated lung structures comparable to those observed in H&E-stained sections (**Figure 4.2**).

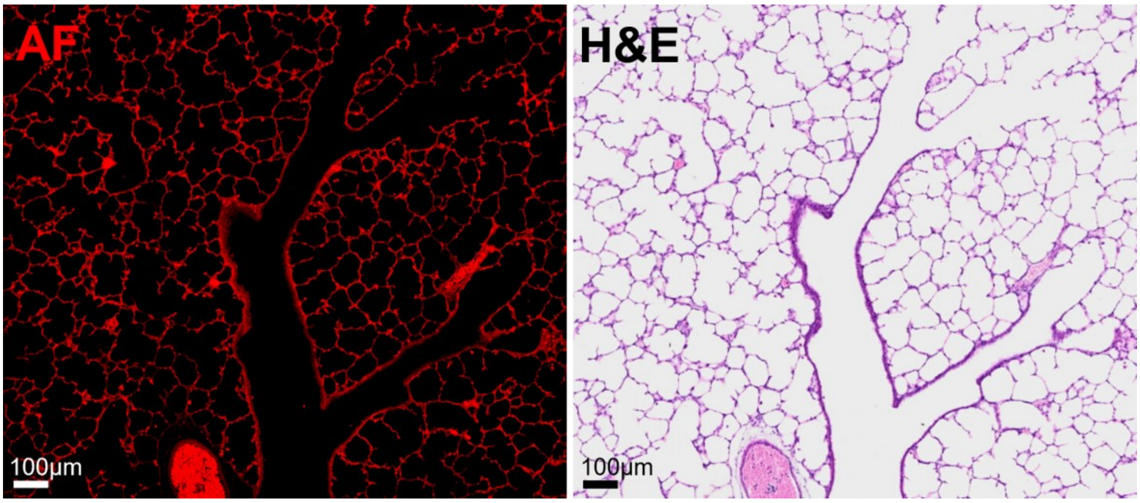

Figure 4.2 Autofluorescence imaging reveals lung parenchymal architecture comparable to that observed with H&E staining. Representative comparison between tissue intrinsic autofluorescence **(left)** and the H&E staining **(right)** of the same lung section.

Moreover, autofluorescence enabled visualization of cellular features, particularly in airways epithelium, vasculature, and alveolar exudates, allowing distinction of cytoplasmic and nuclear components without the need for exogenous staining, as confirmed using DAPI or H&E staining on the same slices (**Figure 4.3 A-C**). This is possible because cellular autofluorescence originates from cytoplasmic and/or mitochondrial components, primarily NADH and FAD, while nuclei remain dark.

Given its strong correspondence with H&E staining and high spatial resolution, tissue autofluorescence has been investigated for studying hyperoxia-induced alterations in lung development, as well as parenchymal signs of inflammation.

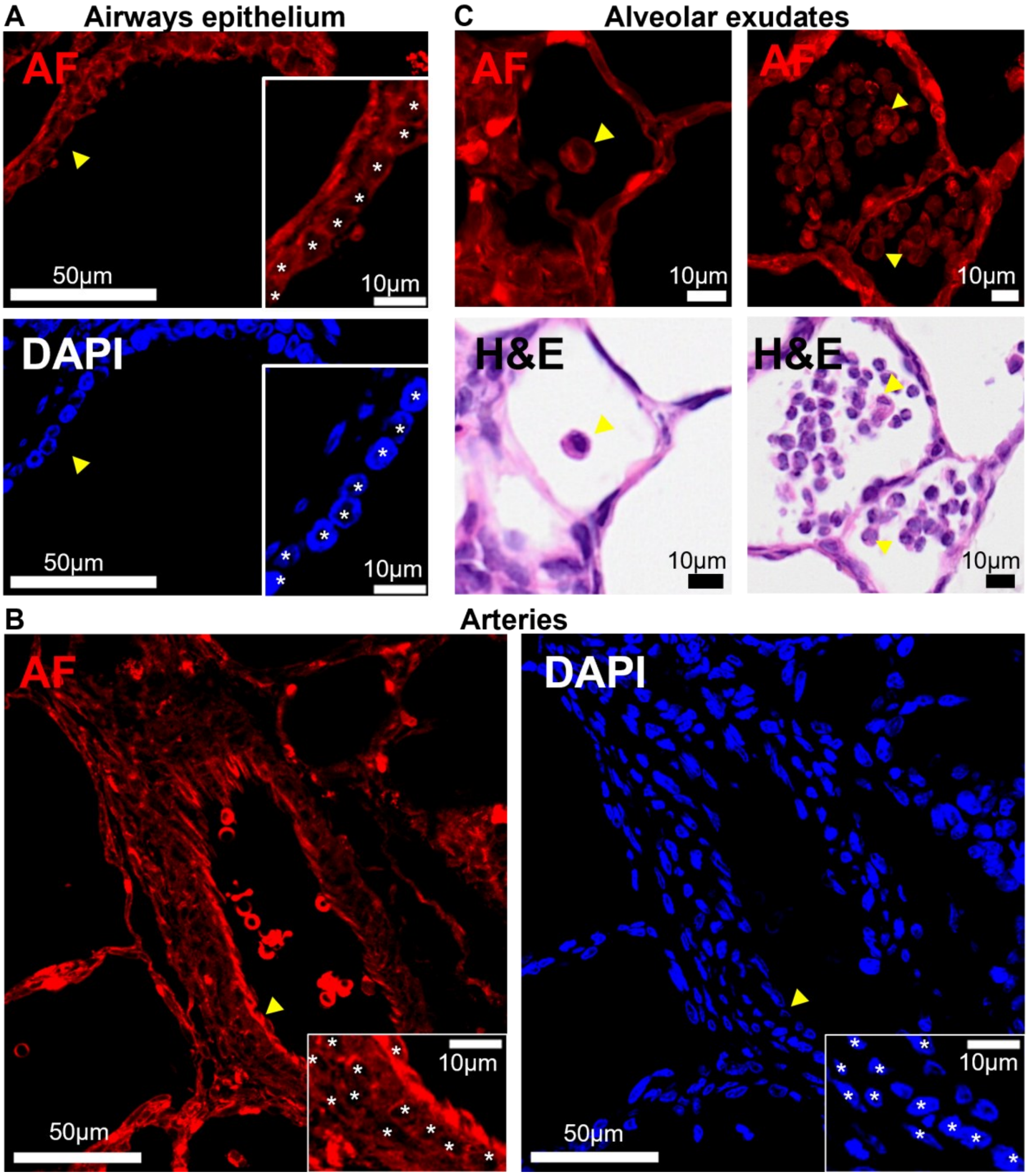

Figure 4.3 The combination of cytoplasmic autofluorescence and the dark nuclei enables the visualization of cells along with their distinctive features. Representative images of tissue autofluorescence and DAPI staining of the same slice demonstrating the label-free ability to visualize cells and their nuclear and cytoplasmic features in **(A)** airways epithelium and **(B)** arteries. Asterisks are used to label the corresponding cells. **(C)** Representative images of tissue autofluorescence and H&E staining of the same slice showing the label-free potential to visualize cells, along with their nuclear and cytoplasmic features in alveolar exudates. These peculiar cytoplasmic and nuclear morphologies may support the identification of specific cell types. Magnified regions **(in A-B)** or cells of interest **(in C)** are indicated with yellow arrowheads.

4.2.1 Hyperoxia induces an increase in alveolar exudates

During inflammation, alveolar spaces become filled with immune-cell infiltrates, primarily neutrophils with fewer macrophages, as well as proteinaceous debris, including fibrin strands and hyaline membranes[177]. Qualitative observations of tissue autofluorescence signal showed a general increase of alveolar exudates in hyperoxic lung tissues compared to the normoxic condition (**Figure 4.4 A**). Moreover, the autofluorescence signal of alveolar exudates in both normoxic and hyperoxic tissues varied, suggesting the presence of a heterogeneous mixture of components (**Figure 4.4 B-D)**. To quantitatively confirm the observed increase of alveolar exudates, I manually measured the area of these alveolar exudates in each mosaic (for more details, see "Density of alveolar exudates" in 3.2 d). This analysis revealed a trend toward increased alveolar exudates in the hyperoxic group (**Figure 4.4 E**). Notably, these potential inflammatory signs showed substantial variability within the group and were patchily distributed across lung sections (**Figure 4.4 F**).

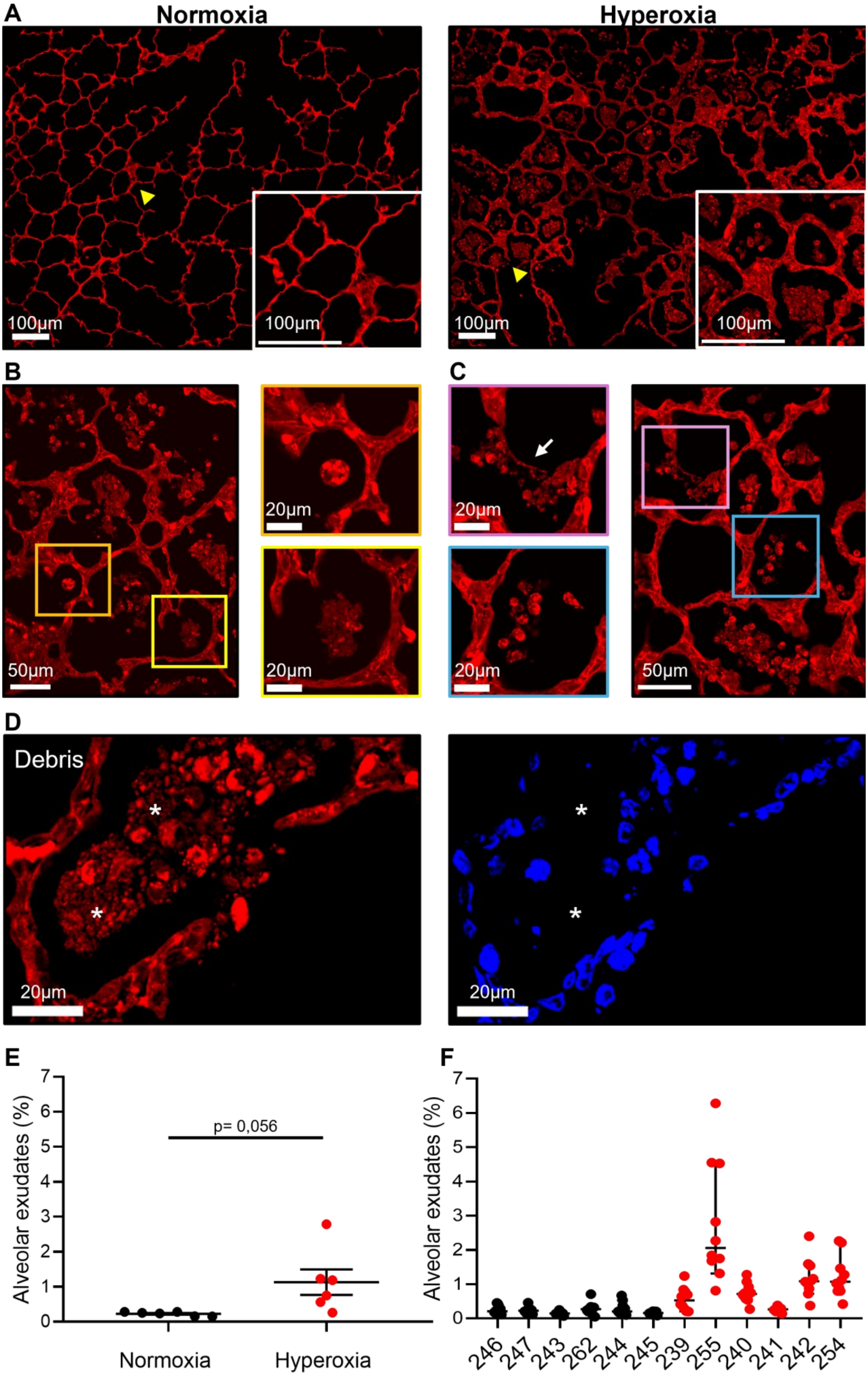
A
Normoxia
Hyperoxia
100µm
100µm
100µm
100µm
B
C
50µm
20µm
20µm
20µm
20µm
50µm
D
Debris
*
*
*
*
20µm
20µm
E
F
Alveolar exudates (%)
0
1
2
3
4
5
6
7
p= 0,056
Normoxia
Hyperoxia
Alveolar exudates (%)
246
247
243
262
244
245
239
255
240
241
242
254

Figure 4.4 Autofluorescence imaging reveals increased alveolar exudates with compositional and spatial variability in hyperoxia-exposed lungs. (A) Representative images of tissue autofluorescence signal from normoxia **(left)** and hyperoxia **(right)** preterm rabbits showing hyperoxia-induced increase of alveolar exudates. Yellow arrowheads indicate the magnified regions**. (B-C)** Representative images of alveolar exudate autofluorescence in hyperoxia lung sections reveal distinct signals, suggesting heterogeneous components within the exudates. Based on these signals, speculations about the composition of the alveolar exudates could be made (orange, yellow, blue, and pink boxes). To evaluate the presence of debris, autofluorescence images were compared with corresponding DAPI-stained slices **(D)** revealing regions (asterisks) without nuclear components. **(E)** Scatter plot of alveolar exudate density (%), measured on tissue autofluorescence in lung sections from n = 6 normoxia and n = 6 hyperoxia preterm rabbits. Welch t-test; Mean ± SEM. **(F)** Scatter plot of alveolar exudate density (%), measured on tissue autofluorescence from ten mosaics per lung section in n = 6 normoxia (black dots) and n = 6 hyperoxia preterm rabbits (red dots) lung sections. Numbers on X-axis identified the Rabbits. Numeration was initially used for blinded analysis. Mean ± SD. The normoxia group showed limited variability, whereas the hyperoxia group exhibited high variability.

4.2.2 Hyperoxia induces an increase in tissue density

During lung development, thick alveolar septa with double capillary layers mature into thin septa containing a single capillary network, thereby improving gas exchange[3]. Autofluorescence imaging revealed increased septal thickness in hyperoxia-exposed lungs compared to normoxic controls as corroborated by H&E- stained slices (**Figure 4.5**).

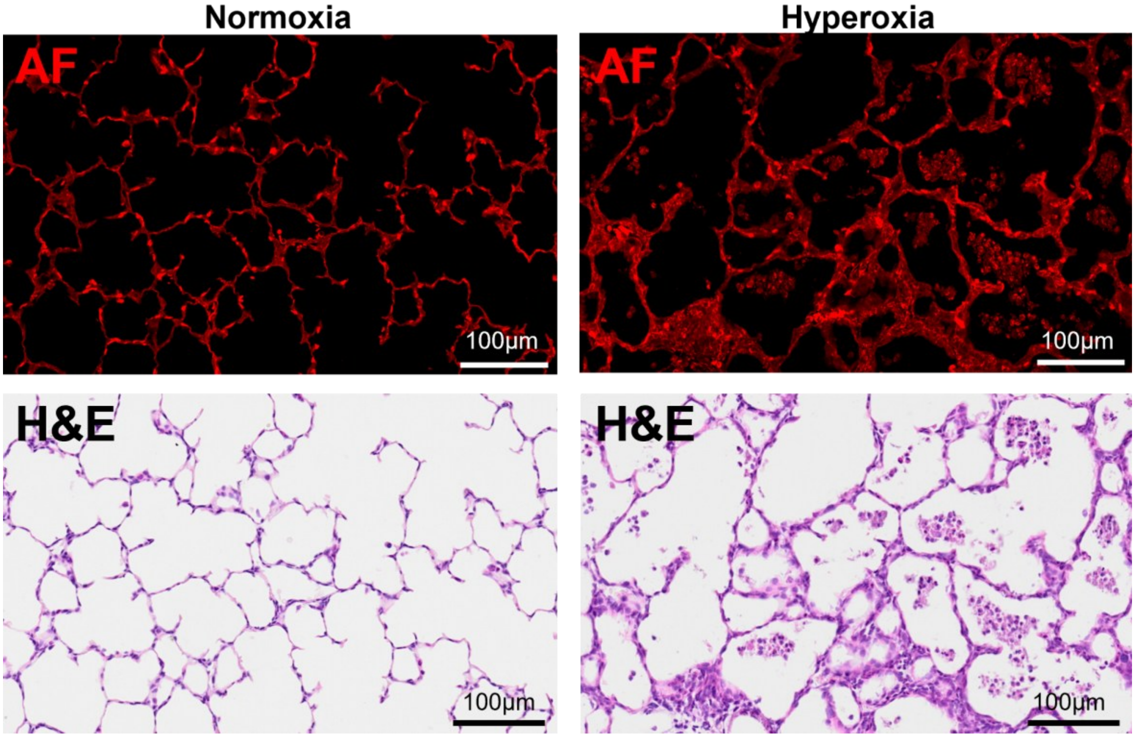

Figure 4.5 Autofluorescence imaging reveals septal thickening in hyperoxic lungs, as corroborated by H&E staining. (top) Representative autofluorescence images of lung sections under normoxia and hyperoxia, showing septal thickening in hyperoxia condition. **(bottom)** H&E staining of the same sections, confirming septal thickening.

To quantitatively validate this observation, I developed a semi-automated, autofluorescence-based method for quantifying tissue density, as a surrogate marker of septal thickening. Several thresholding algorithms were evaluated for tissue segmentation, including Otsu[230], Huang[227], and Percentile methods, applied to both normoxic and hyperoxic lung sections. Otsu's threshold tended to under-segment the tissue, resulting in discontinuous selection, while the Percentile method led to over-segmentation (**Figure 4.6 A**). Among these, the Huang method produced the most accurate and consistent tissue segmentation (**Figure 4.6 A**). However, all thresholding approaches indiscriminately identified autofluorescent structures, including alveolar exudates, thereby inflating tissue area measurements (**Figure 4.6 B**). To correct this, alveolar exudate areas were subtracted from total tissue measurements. Using this refined approach, tissue density was found to be increased under hyperoxic condition (**Figure 4.6 C**).

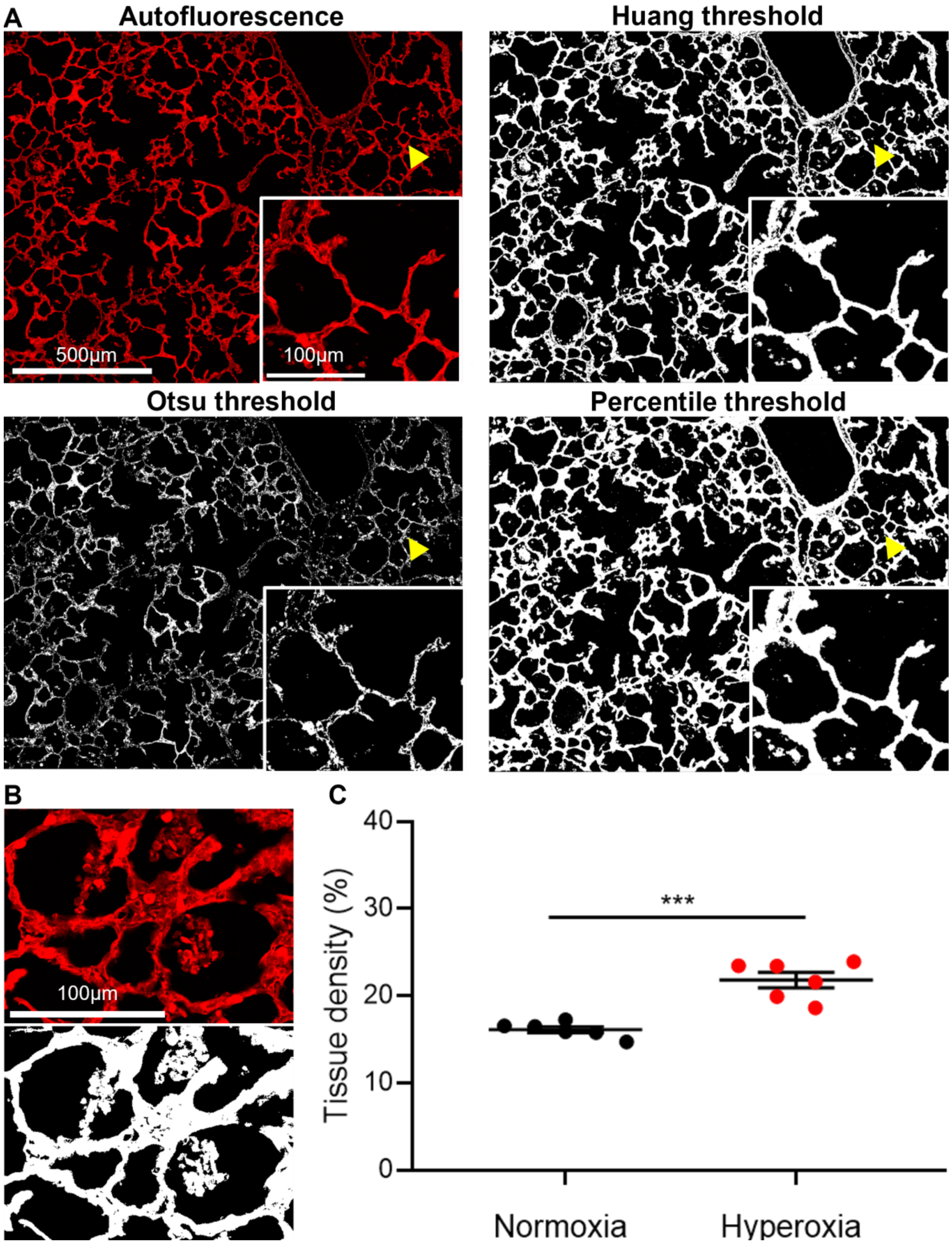

Figure 4.6 Autofluorescence-based assessment of tissue density reveals increased values under hyperoxic exposure. (A) Comparison between three different thresholding methods including Huang **(top right),** Otsu **(bottom left)**, and Percentile **(bottom right)** for selecting tissue segments. Unlike the Huang thresholding method, Otsu's threshold tended to under-segment the tissue while Percentile's threshold tended to over-segment it. **(B)** Representative images of autofluorescent alveolar exudates **(top)** and their inclusion during tissue segmentation using the thresholding method **(bottom)**. To avoid overestimation, exudate areas were subsequently excluded from the calculation of tissue area. **(C)** Scatter plot of tissue density (%) calculated from tissue autofluorescence signal in lung sections from n = 6 normoxia and n = 6 hyperoxia preterm rabbits. Unpaired t-test; Mean ± SEM.

4.2.3 Hyperoxia induces an attenuation of autofluorescence intensity

Autofluorescence intensity depends on the composition and the intrinsic fluorescence properties of endogenous molecules that are excited and emit within the considered spectral range. Therefore, variations in autofluorescence intensity may serve as intrinsic indicators of compositional changes characteristic of disease states[187]. To measure tissue autofluorescence intensity, the automated Huang thresholding method, previously described, was used to segment the tissue. Under identical acquisition settings, hyperoxic lung tissue exhibited an approximately 2-unit lower autofluorescence intensity compared to normoxic tissue (**Figure 4.7**). The reason for this alteration needs further investigation.

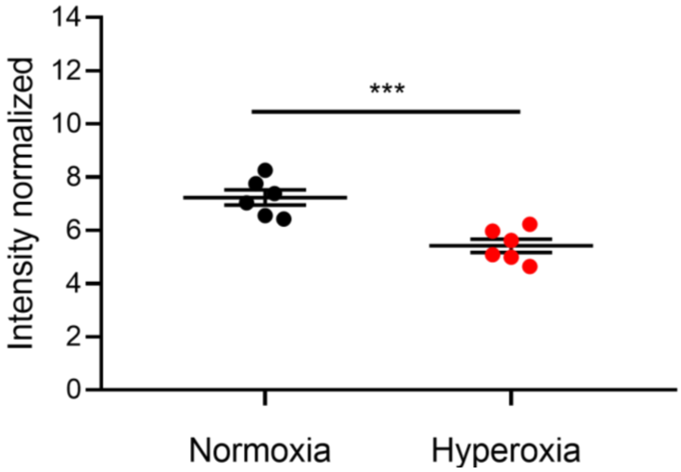

Figure 4.7 Hyperoxia exposure induces an attenuation of autofluorescence intensity. Scatter plot of the intensity of autofluorescence calculated in lung sections from n = 6 normoxia and n = 6 hyperoxia preterm rabbits. Unpaired t-test; Mean ± SEM were presented for both conditions.

4.3 SHG-based contrast reveals mild fibrosis in hyperoxic lungs

Altered collagen deposition was observed in both neonates with BPD and animal models[54,88,149,162,231,232]. To evaluate collagen fiber deposition following hyperoxia exposure, a dedicated imaging channel was employed to acquire SHG signals produced by the collagen fibers. Specifically, the SHG signal was collected in the 380-410 nm range following excitation at 780 nm, which corresponds to the expected emission range for SHG[194]. To confirm that the collected signal specifically originated from collagen, tissue sections were stained with PSR, a well-established histological and fluorescent marker for fibrillar collagen[233–235]. Since PSR fluorescence has been shown to provide a stronger and more specific signal for collagen than brightfield microscopy[234], fluorescence imaging of PSR-stained sections was used as a reference. A consistent qualitative correspondence between the SHG signal and PSR fluorescence was observed (**Figure 4.8**), thereby supporting the reliability of the procedure.

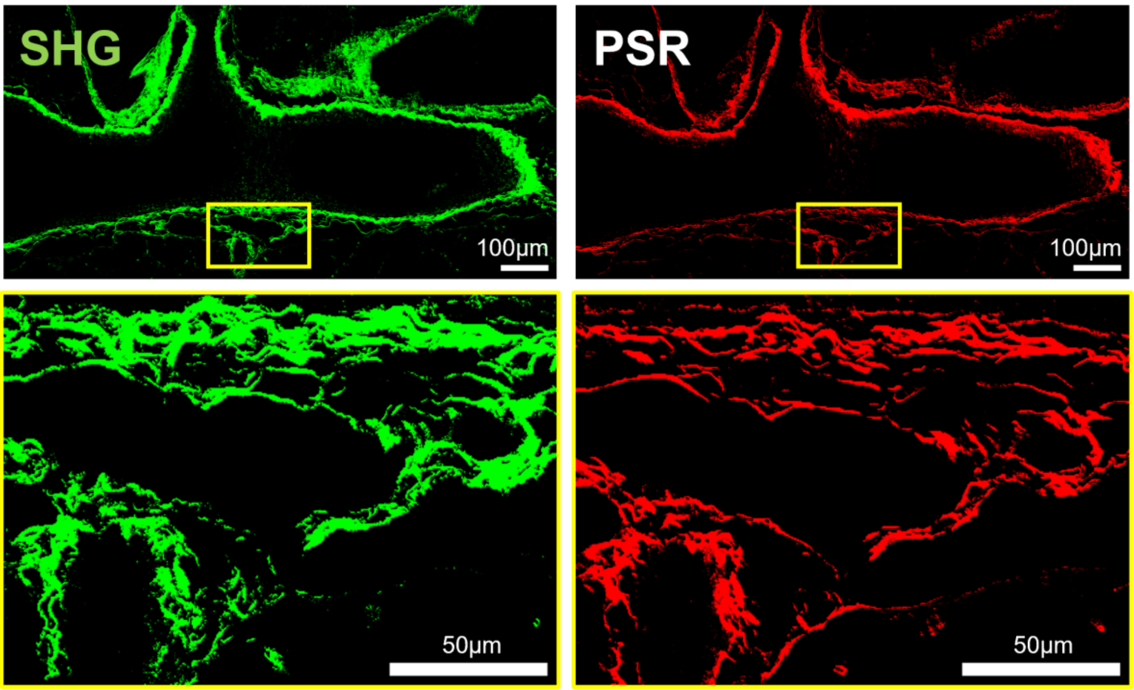

Figure 4.8 The SHG signal reveals a consistent qualitative association with PSR staining. Representative images comparing SHG signal **(left)** and PSR fluorescence **(right)** on the same lung section. Yellow rectangles for magnified regions.

However, highly autofluorescent structures, such as RBCs and other spot-like features, were found to potentially interfere with the SHG signal from collagen. These structures emitted broadly across the spectrum, including within the SHG detection range (**Figure 4.9 A**), and did not produce true SHG signals, as their emissions persisted at 380-410 nm under excitation at 720 and 840 nm (**Figure 4.9 B**), confirming they are not fibrillar collagen.

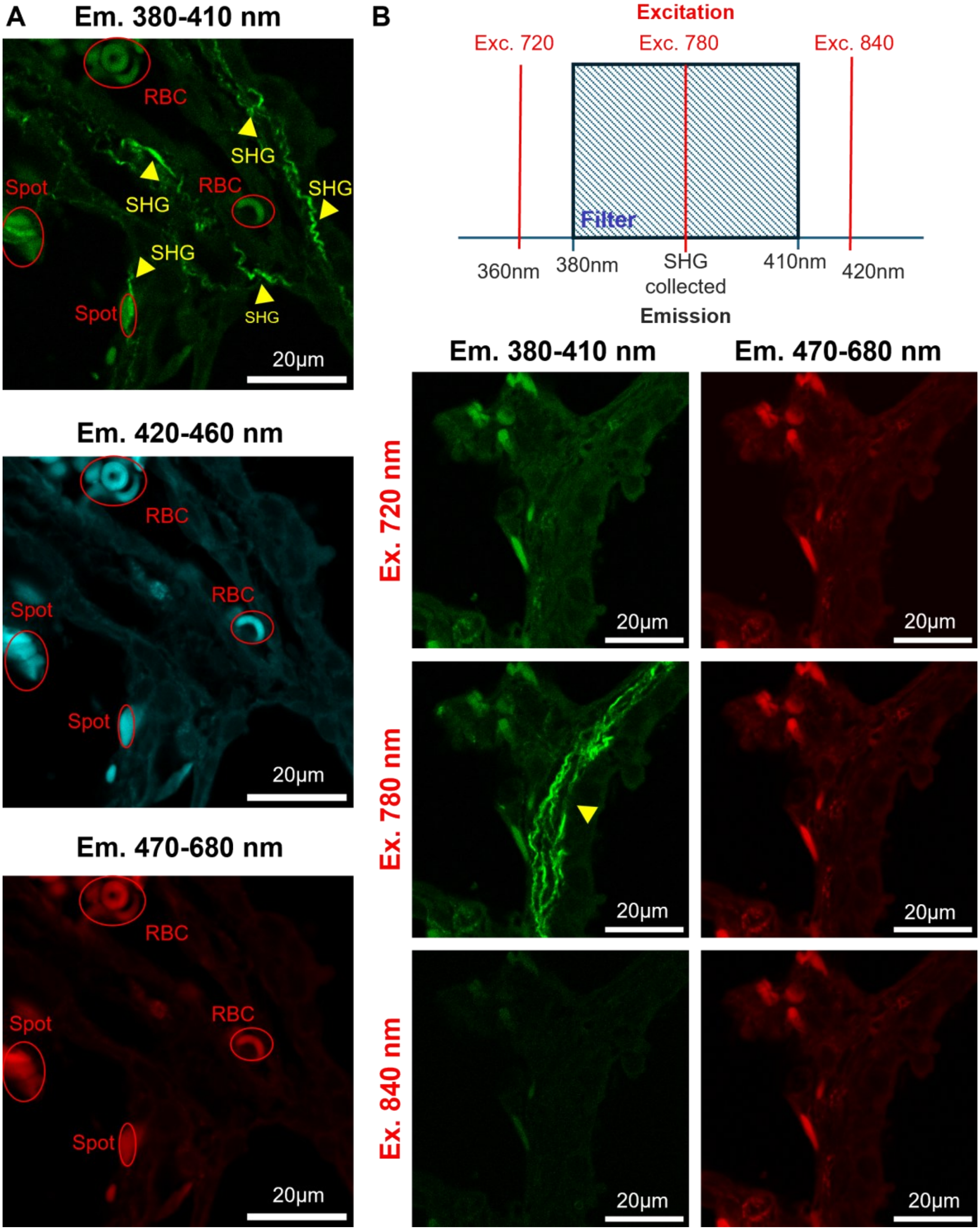

Figure 4.9 Autofluorescence artifacts from RBCs and spot-like features in SHG channel. (A) Representative images of lung sections excited at 780 nm, with emissions recorded at 380-410 nm (green), 420-460 nm (cyan), and 470-680 nm (red). The autofluorescence of spots and RBCs was ubiquitous across the emission spectrum (red circles) and exhibited higher intensity compared to other tissue components in all channels. In the 380-410 nm range, it interfered with SHG signals (yellow arrowheads) primarily those with weaker signals. **(B) (top)** Schematic representation of the experimental procedure used to verify the true SHG signal. Three wavelengths (red line) (720 - 780 - 840 nm) were used to excite the lung sections. A 380-410 nm bandpass filter was placed in front of the detector to isolate half of the illumination wavelength of our tool (780 nm), corresponding to the SHG signal wavelength by definition[194]. Finally, autofluorescence was collected in the 470-680 nm range. **(bottom)** Representative images showing that spot signals remained present in the 380-410 nm range when excited at 720 nm and 840 nm, demonstrating that they did not exhibit a true SHG signal, unlike the one marked by the arrowhead.

Spectral and FLIM analyses showed similar profiles for both RBCs and the spot-like features, suggesting a common origin and supporting the hypothesis that these spots may represent capillaries containing trapped RBCs (**Figure 4.10**).

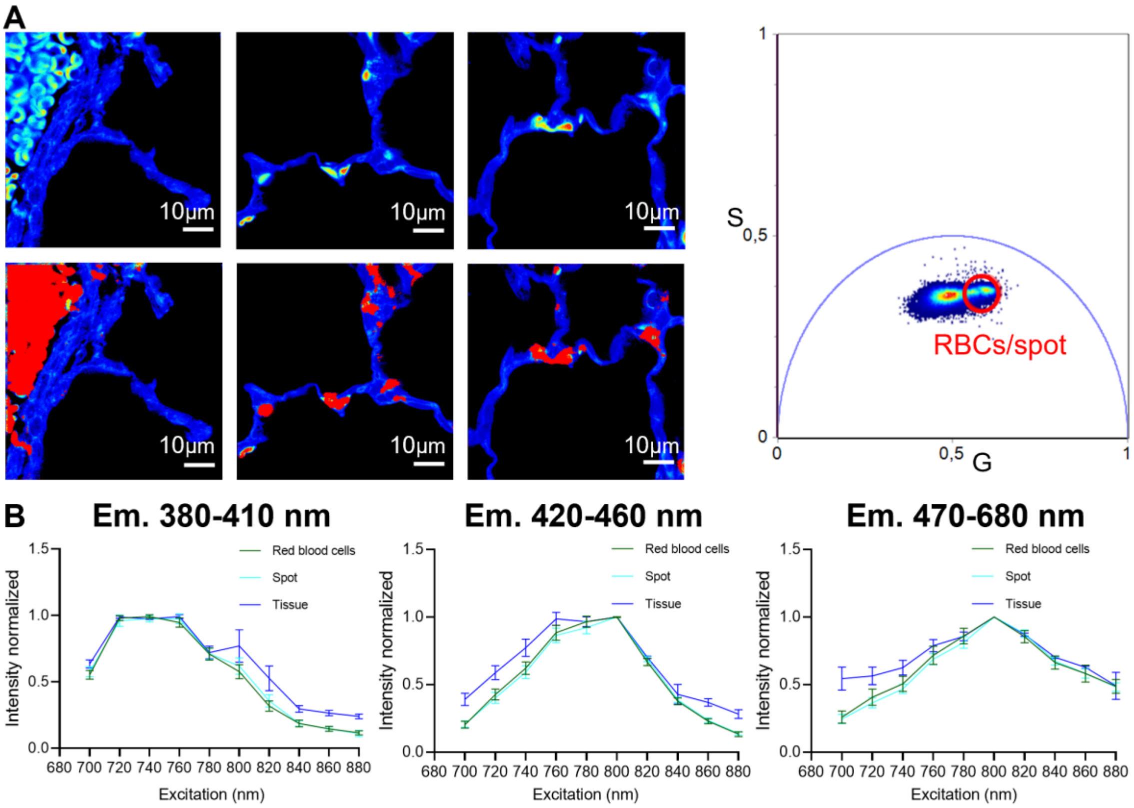

Figure 4.10 Highly autofluorescent, spot-like structures exhibit spectral and lifetime properties consistent with those of RBCs. (A) FLIM of tissue autofluorescence in the 420-460 nm range revealed similar lifetimes between RBCs and spot-like structures. By highlighting clusters of pixels in the right part of the phasor plot (which corresponds to shorter lifetimes), pixels corresponding to RBCs and spot-like structures were marked (in red) in the fluorescence intensity images. **(B)** Spectral analysis was performed manually by varying the excitation wavelength between 700 and 880 nm, while simultaneously collecting signals at fixed intervals in the following ranges: 380-410 nm **(left)**, 420-460 nm **(middle)**, and 470-680 nm **(right)**. For each excitation wavelength and acquisition range, the autofluorescence intensity was measured in ROIs drawn around RBCs, spots, and other tissue regions, with the same ROIs maintained across all setup changes. The intensities were then normalized to the maximum value observed within each emission range. The spectra of RBCs (green) and spots (light blue) overlapped but differed from those of ROIs taken from other tissue regions (blue) across all ranges.

To address potential interference from RBCs and spots, image preprocessing was performed prior to collagen analysis. Specifically, autofluorescence was subtracted to eliminate signal contributions from RBCs and other autofluorescent artifacts. Compared to normoxic controls, lungs exposed to hyperoxia exhibited increased deposition of fibrillar collagen, suggesting mild fibrosis (**Figure 4.11 A).** Under normoxia, collagen appeared to be primarily localized at secondary septal tips (**Figure 4.11 A**), consistent with areas of active alveolarization (**Figure 4.11 B**). A similar pattern was observed in consecutive sections by IHC with an anti-Col1a1 antibody, detecting type I collagen, the most abundant fibrillar collagen (**Figure 4.11 C**), and by PSR staining **(Figure 4.11D).**

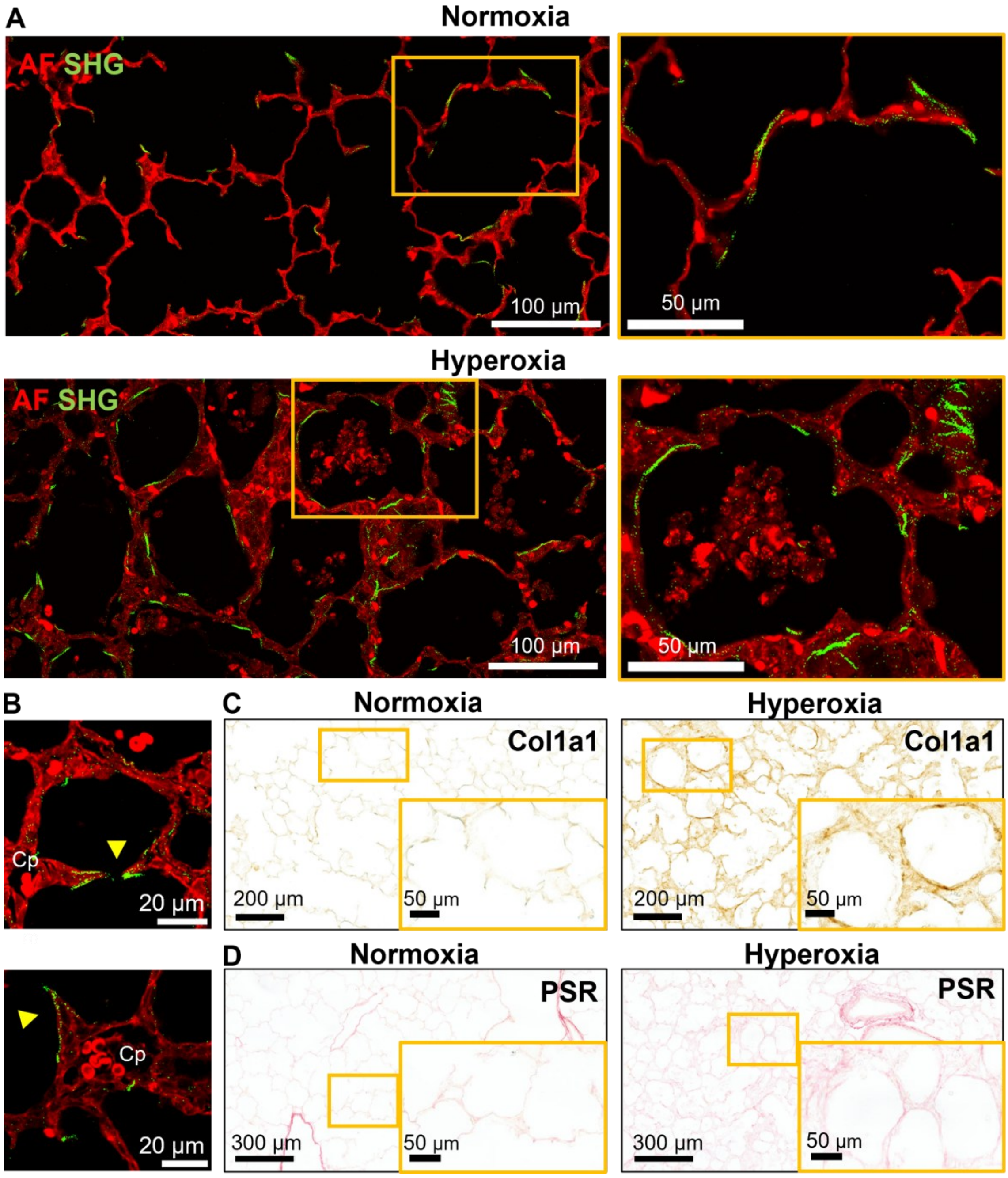

Figure 4.11 Fibrillar collagen content and localization. (A) Representative images of SHG (green) and autofluorescence (red) showing an increased collagen content under hyperoxia. In normoxia **(top)**, fibrillar collagen was mainly localized at secondary septa tips, while in hyperoxic lungs **(bottom)**, it was extensively deposited throughout alveolar septa and interstitial spaces. **(B)** Representative images of the secondary crests with capillaries ("Cp") and the characteristic collagen pattern (yellow arrowhead). Images of SHG signal were presented after autofluorescence subtraction as detailed in section 3.2 d "density of total and parenchymal collagen %". Representative images of Col1a1 antibody staining **(C)** and PSR staining **(D)** in lung sections from normoxic **(left)** and hyperoxic **(right)** animals, showing increased deposition of fibrillar collagen under hyperoxia, and predominant localization at the tips of secondary septa under normoxia.

To quantify fibrillar collagen deposition, I developed and optimized, a semi-automated image analysis workflow based on SHG imaging. Several filtering techniques previously employed for collagen quantification[229], such as CLAHE[236], median filtering[237], and the Frangi vesselness filter[228], were systematically evaluated for their effectiveness in enhancing SHG signal and enabling accurate segmentation. Among these, the combination of the Frangi vesselness filter with Otsu thresholding emerged as the most reliable approach for collagen fiber segmentation (**Figure 4.12 A**). For details, see section 3.2 d "Density of total and parenchymal collagen %".

The total fibrillar collagen area was quantified in each SHG mosaic, normalized to the acquisition area, and averaged to obtain a mean value per rabbit. This analysis revealed an overall increase in collagen deposition under hyperoxic conditions (**Figure 4.12 B**). To verify that this increase was not biased by the presence of large airways or vascular structures, known to contain higher levels of collagen, a focused analysis of parenchymal regions was performed. Using the autofluorescence channel, areas devoid of airways and vessels were carefully identified within the same mosaics. Within these regions, the corresponding collagen fiber area in the SHG channel was quantified, normalized to the selected area, and averaged to yield a mean value per rabbit. This refined quantification confirmed the previously observed increase in fibrillar collagen deposition under hyperoxic conditions (**Figure 4.12 C**)

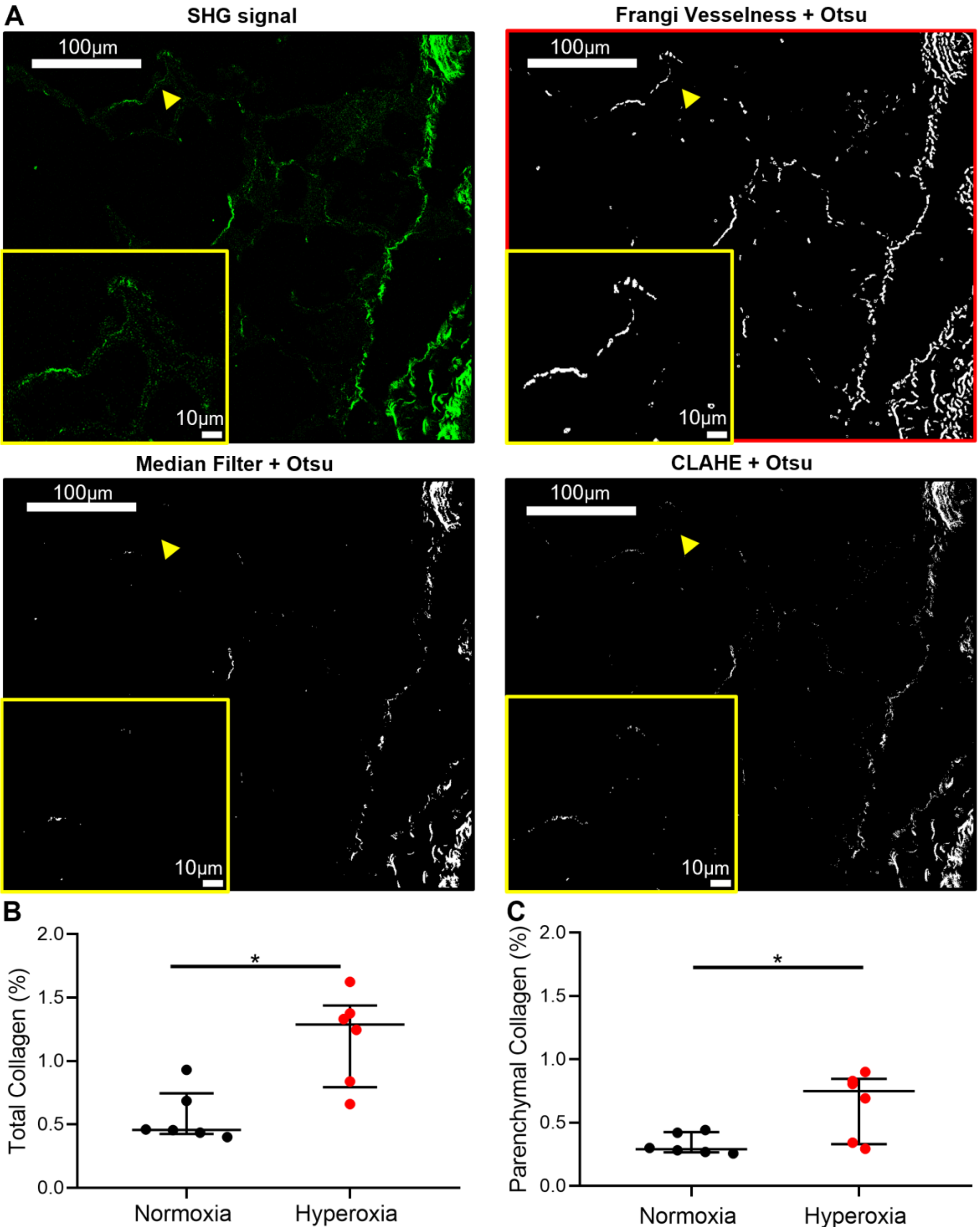

Figure 4.12 SHG quantification method based on the Frangi vesselness filter and Otsu's thresholding reveals an increase in fibrillar collagen deposition in hyperoxia. **(A)** Representative images illustrating the application of different image-processing techniques for selection and enhancement of SHG-detected collagen, specifically in regions without airways and vessels (yellow arrowheads). **(top left)** SHG signal after autofluorescence subtraction. Otsu thresholding, applied after (**bottom left**) median filtering or (**bottom right**) CLAHE resulted in suboptimal collagen segmentation due to under-selection. In contrast, combining Otsu thresholding with **(top right)** the Frangi vesselness filter yielded more accurate fiber selection and enhanced signal. **(B)** Scatter plot of density of total fibrillar collagen (%) measured on lung sections from n=6 Normoxia and n=6 Hyperoxia preterm rabbits. Mann-Whitney test; Median ± IQR. **(C)** Scatter plot of density of parenchymal collagen (%) measured on lung sections from n=6 Normoxia and n=6 by excluding collagen from airways and vessels. Hyperoxia preterm rabbits show significantly higher deposition of parenchymal collagen in hyperoxia. Mann-Whitney test; Median ± IQR.

4.4 Features based on autofluorescence and SHG contrast: arterial media thickness and alveolar density

4.4.1 Hyperoxia induces an increase in MT%

Vascular impairment is a clinical and experimental hallmark of BPD[88,95,96,164,176,238]. The combination of SHG and autofluorescence signals enabled identification of larger vessels, (i.e., >50 μm), as verified by CD31/PECAM-1 immunolabelling (**Figure 4.13 A**) and H&E staining **(Figure 4.13 B**). However, in vessels where the collagen layer is extremely thin or lacking (e.g., capillaries), structural identification becomes challenging.

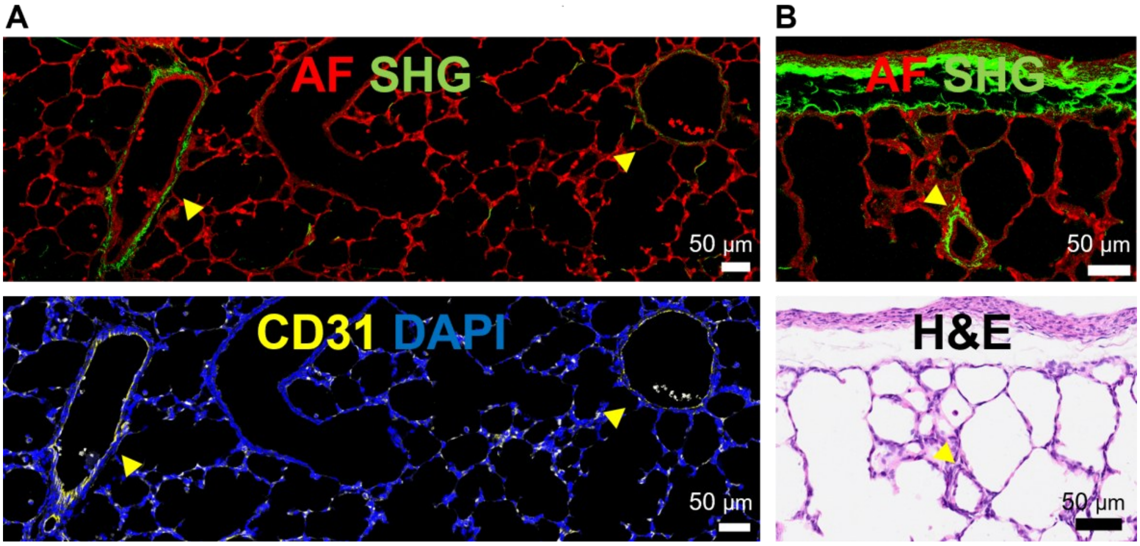

Figure 4.13 Combination of autofluorescence and SHG allows for vessels identification. (A) (top) Representative image of autofluorescence and SHG signals. **(bottom)** The same section stained with CD31/PECAM1 and DAPI. **(B) (top)** Representative image of autofluorescence and SHG signals. **(bottom)** The same section stained with H&E. Notably, images of SHG signal were presented after autofluorescence subtraction as detailed in section 3.2 d "density of total and parenchymal collagen %,". Yellow arrowheads indicate vessels.

As illustrated in **Figure 4.14 A**, arteries displayed an outer layer with a strong SHG signal, likely corresponding to the collagen-rich *tunica adventitia*[187]. This interpretation is further supported by the Col1a1 staining shown in **Figure 4.14 B**, which highlights a similar structure. In contrast, the inner layers showed autofluorescence attributable to cellular components and elastin, characteristic of the *tunica media and intima* (**Figure 4.14 A**). RBCs were sometimes present within the lumen (**Figure 4.14 A)**. In the tunica media, layers of smooth muscle were distinguishable due to their autofluorescent cytoplasm and dark, elongated nuclei (**Figure 4.14 A**). Smooth muscle cells were identified by immunostaining with an anti- α-SMA antibody (**Figure 4.14 C**). When present, the internal elastic membrane of the *tunica intima* appeared clearly visible, displaying higher autofluorescence intensity compared to the surrounding structures[187] (**Figure 4.14 A)**. Endothelial cells were occasionally identifiable within the *tunica intima* (**Figure 4.14 A**), as confirmed by anti CD31/PECAM-1 staining (**Figure 4.14 D)**.

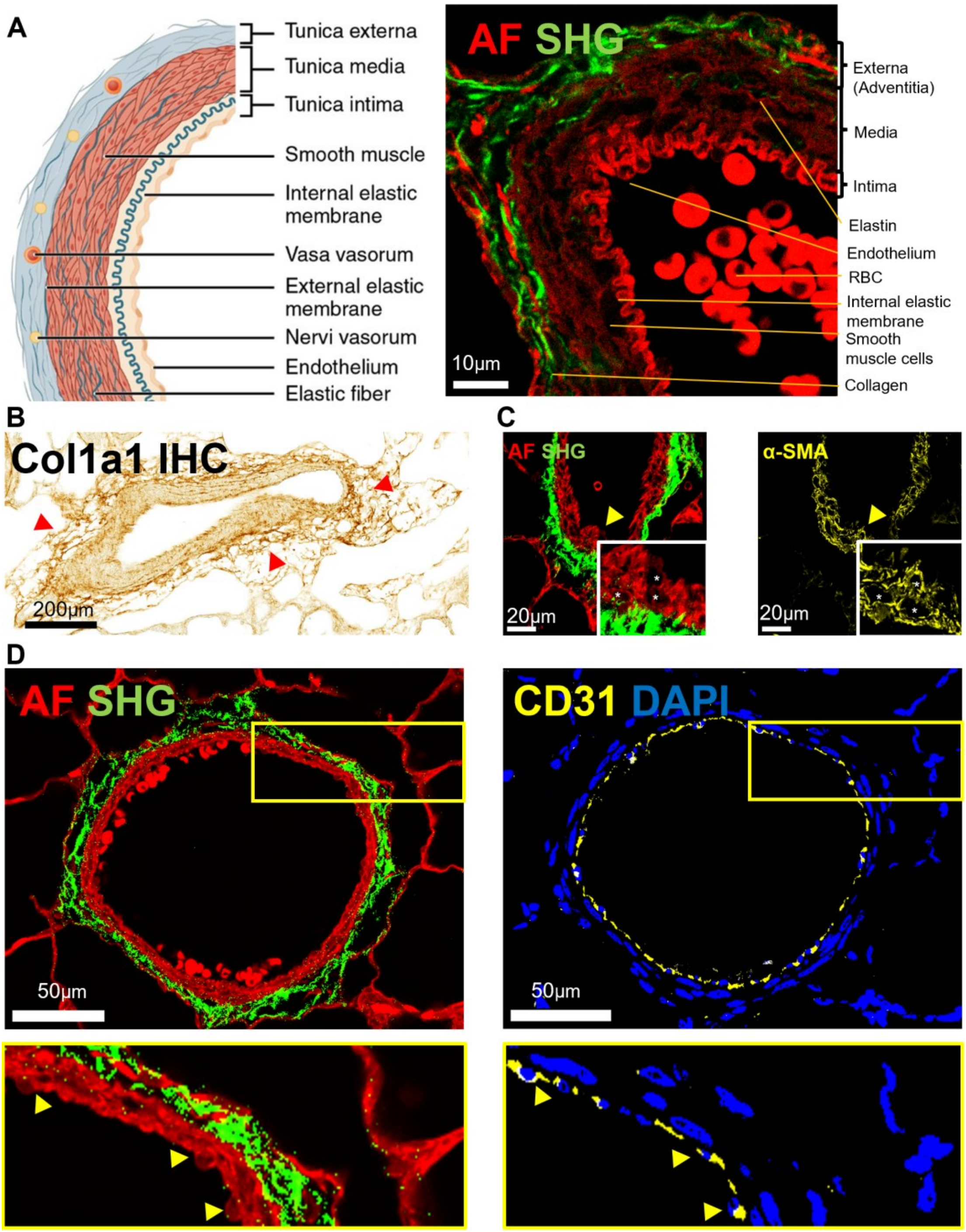

Figure 4.14 Label-free visualization and composition of arterial layers (A) (left) Schematic representation of artery. Image adapted from OpenStax College, Anatomy and Physiology. OpenStax CNX. **(right)** Representative image of the label-free appearance of arteries by combining autofluorescence (red) and SHG (green). Each line corresponds to a different component listed in the figure. **(B)** Representative image showing collagen I deposition in the tunica adventitia (red arrowheads). Collagen was detected by IHC using an anti-Col1a1 antibody. **(C)** Smooth muscle cells in the tunica media were identified label-free based on their autofluorescent cytoplasm and elongated, non-fluorescent nuclei **(left)**, and confirmed by immunofluorescence with anti-αSMA antibody on the same lung section **(right)**. The yellow arrowhead indicates the region shown at higher magnification. **(D)** Representative image of endothelial cells in the tunica intima, identified label-free by their thin autofluorescent cytoplasm and small, non-fluorescent nuclei (yellow arrowheads, **left**). Immunofluorescence using an anti-CD31/PECAM-1 antibody on the same lung section confirmed their identity (yellow arrowheads, **right**). Notably, SHG images are presented after autofluorescence subtraction as detailed in 3.2 d "density of total and parenchymal collagen %"

Muscularized vessels were classified as arteries for the purpose of medial thickness assessment. A qualitative comparison between normoxic and hyperoxic lungs revealed an increase in wall thickness (**Figure 4.15 A**). Further confirmed by the label-free based quantification of MT% (**Figure 4.15 B**), a well-established indicator of vascular impairment in BPD[164,166,176]. In contrast, no significant difference was found by measuring adventitial thickness on the same vessels (**Figure 4.15 C**).

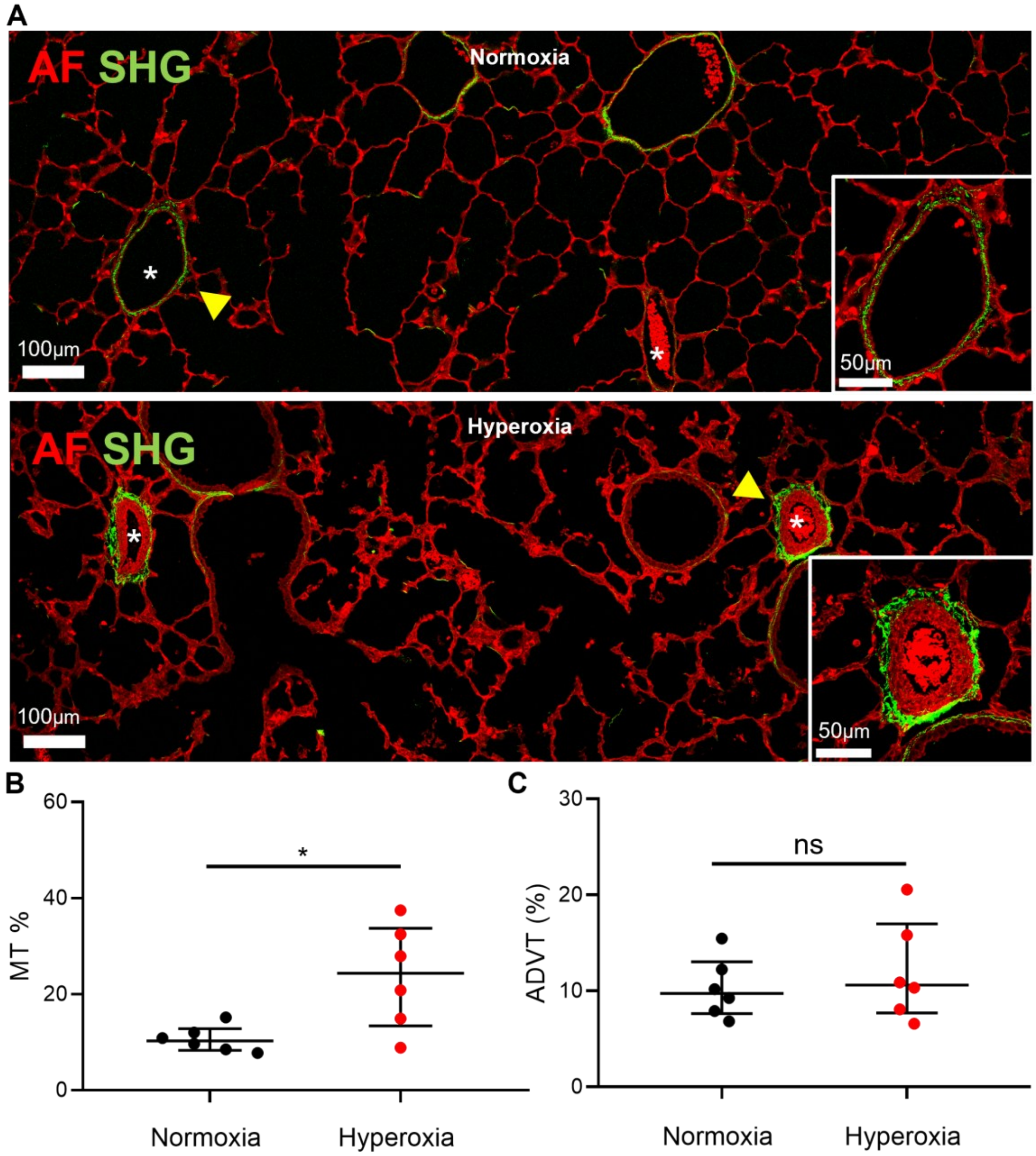

Figure 4.15 Hyperoxia exposure induces an increased MT%. (A) Representative comparison between normoxia **(top)** and hyperoxia **(bottom)**: Autofluorescence in red, and SHG, in green. Asterisks indicate vessels with ED between 50 and 100 µm. Arrowheads indicate the location of magnified region. **(B)** Scatter plot shows the MT% measured on lung sections from n=6 Normoxia and n=6 Hyperoxia preterm rabbits. Mann-Whitney test; Median ± IQR are presented. **(C)** Scatter plot shows the percentage of adventitia thickness (ADVT%) measured on lung sections from n=6 Normoxia and n=6 Hyperoxia preterm rabbits. Mann-Whitney test and Median ± IQR are presented. Notably, SHG presented after autofluorescence subtraction as detailed in 3.2 d "density of total and parenchymal collagen %"

4.4.2 Hyperoxia induces a decrease in alveolar density

Alveolar simplification is a key feature of BPD and its reproduction in animal models is essential for the study of the disease[87]. To assess whether hyperoxia induced impairment in alveolar development, an alveolar density metric was established by identifying and counting all air spaces within a defined region of each mosaic, excluding airways, vessels and alveolar sacs (for more details, see "alveolar density" in 3.2 d). Lungs exposed to hyperoxia exhibited alveolar simplification, characterized by an approximately 22% reduction in alveolar density (**Figure 4.16**).

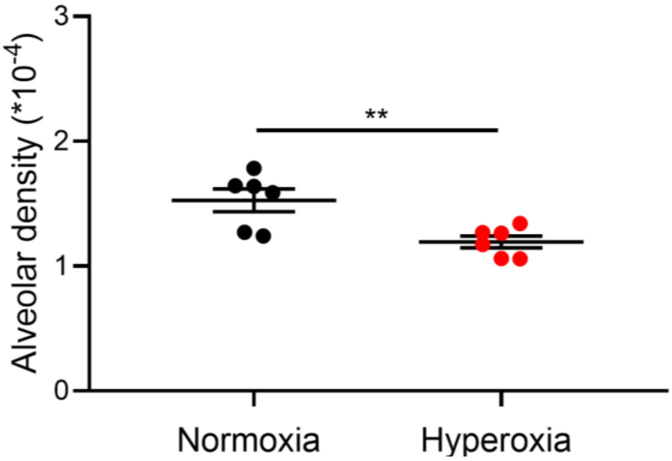

Figure 4.16 Hyperoxia exposure induces a reduction in alveolar density. Scatter plot of alveolar density measured on lung sections from n=6 normoxia and n=6 hyperoxia preterm rabbits. Unpaired t-test; mean ± SEM. Notably, the number of enclosed spaces was divided by the measured area (in μm^2), and then arbitrarily multiplied for 10^4 for visual representation.

4.5 Autofluorescence lifetime-based contrast reveals a shift toward longer lifetime in hyperoxia

A further analysis was conducted using FLIM to identify tissue autofluorescence lifetime of lung sections under normoxia and hyperoxia conditions. Fluorescence lifetime, like fluorescence intensity, is a property that depends on the composition of endogenous fluorophores within the tissue. Unlike intensity, autofluorescence lifetime is independent of the concentrations of fluorophores, making it more sensitive to tissue molecular composition, and it also reflects the local microenvironment[209]. Consequently, tissue autofluorescence lifetime provides an additional layer of contrast to distinguish between hyperoxic and normoxic tissues. The measured lifetimes, upon phasor transformation (for details, see section 3.1.2.1), showed an elongated distribution within the universal semi-circle in both conditions with phasor centroids shifted toward longer lifetime in hyperoxia

(**Figure 4.17 A**). This observation was confirmed by measuring the G coordinate of the phasor cluster centroids in both conditions (**Figure 4.17 B**). This shift, by itself, reflects intrinsic molecular differences that can be exploited for diseased tissue classification without prior knowledge.

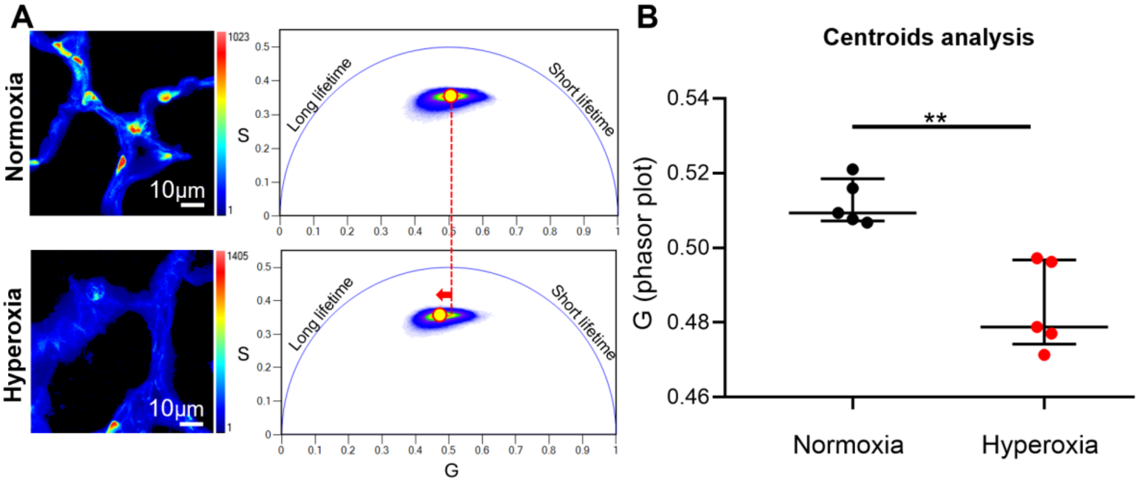

Figure 4.17. Hyperoxia induces a shift toward longer autofluorescence lifetime (A) Representative FLIM images of normoxia **(top)** and hyperoxia **(bottom)** lung sections depicted the distribution of fluorescence intensity with each pixel having a corresponding point in their phasor plots. Shifts in autofluorescence lifetime can be modeled using phasor centroids (yellow dots) and their movement between the two conditions. **(B)** Quantitative measurements of centroid shifts along G axis. Scatter plot of the G coordinates of the centroids measured for each cluster of points in the phasor plot for each of the n = 5 normoxia rabbits and n = 5 hyperoxia rabbits. Mann-Whitney test; Median ± IQR (Δ median = 0.031). The S coordinate of the phasor plot was not considered because it did not differ significantly.

4.6 Label-free analysis correlates with H&E-based histomorphology and lung functions

To validate the reliability and outcomes of the label-free analytical approach, correlation analyses were performed between label-free measurements including alveolar density, alveolar exudates, and MT%, and established histopathological parameters obtained from H&E-stained sections of the same rabbit lungs. These reference metrics, namely RAC, ALI score, and MT% are widely recognized indicators of alveolar development, inflammation, and vascular remodelling, respectively. Notably, all three label-free parameters showed strong and statistically significant correlations with the conventional BPD-related histomorphometric measurements (**Figure 4.18 A-C**), supporting the validity of the method. Specifically, alveolar density correlated with RAC (r = 0.85; **Figure 4.18 A**), alveolar exudates correlated with the ALI score (r = 0.82; **Figure 4.18 B**), and MT% values from label-free imaging correlated with those from H&E sections (r = 0.87; **Figure 4.18 C**).

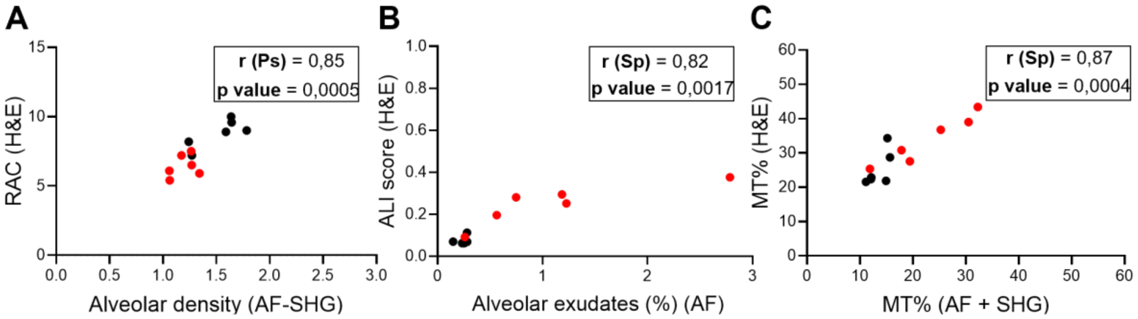

Figure 4.18 Label-free histomorphological features correlate with H&E-based findings. Black dots were normoxia rabbits, while red dots were hyperoxia rabbits. **(A)** Pearson correlation test between alveolar density measured from label-free signals and RAC calculated in H&E-stained lung sections from the same rabbits. **(B)** Spearman correlation test between the percentage of alveolar exudates measured on the autofluorescence signal, and the ALI score measured in H&E-stained lung sections from the same rabbits. **(C)** Spearman correlation test between the MT% measured on label-free signals and those calculated in H&E-stained lung sections from the same rabbits.

Moreover, to determine whether the histological alterations detected through the label-free approach also correlated with functional impairments, prior to lung sections collection, selected functional parameters were measured in live animals using the Flexivent system (For details, see section 3.2 e-f "Lung function measurements"). These included inspiratory capacity (IC), tissue damping (G), tissue elastance (H) and static compliance (Cst). The results showed a decrease in IC and Cst (**Figure 4.19 A-B**), and an increase in H and G (**Figure 4.19 C-D**). Subsequently, two PCA were performed. The first PCA incorporated all label-free features obtained from each sample: tissue and alveolar density, alveolar exudate, autofluorescence intensity and lifetime, fibrillar collagen content and MT%. In this analysis the two groups were well separated: normoxic rabbits formed a relatively tight cluster, whereas hyperoxic rabbits were more widely dispersed, reflecting greater heterogeneity in histological alterations (**Figure 4.19 E**). The second PCA was performed using the four lung function parameters. Similar to the first analysis, hyperoxic rabbits exhibited greater variability than normoxic controls, suggesting a range of functional impairments within the hyperoxic group (**Figure 4.19 F**). To assess the overall relationship between lung parenchyma damage detected label-free and lung functions impairments, we performed a correlation analysis using the principal component scores derived from the histological and functional PCAs already calculated **(Figure 4.19 G)**. The first principal component (PC1) from each analysis, which captured the largest portion of variation in the histological and functional data, was used as an overall *Histological Score* and *Functional Score*, respectively (lower PC1 score = greater severity). This analysis revealed a strong and significant positive correlation between the two scores (Pearson's r = 0.85, p = 0.0004), indicating that the overall histological and functional profiles were tightly coupled. The resulting plot clearly separated the normoxia and hyperoxia groups into distinct clusters at opposite ends of a shared linear trend ($R^2 = 0,72$). This relationship demonstrated that the magnitude of the pathological alteration was proportional: animals positioned along this regression line exhibited a close correspondence between histological and functional severity.

Taken together, the strong and consistent correlations observed between label-free parameters and both classical histological metrics and lung function measurements provided compelling evidence for the robustness and reliability of the label-free analytical tool. These findings demonstrated the tool's capacity to accurately identify and quantify key structural alterations associated with hyperoxic lung injury.

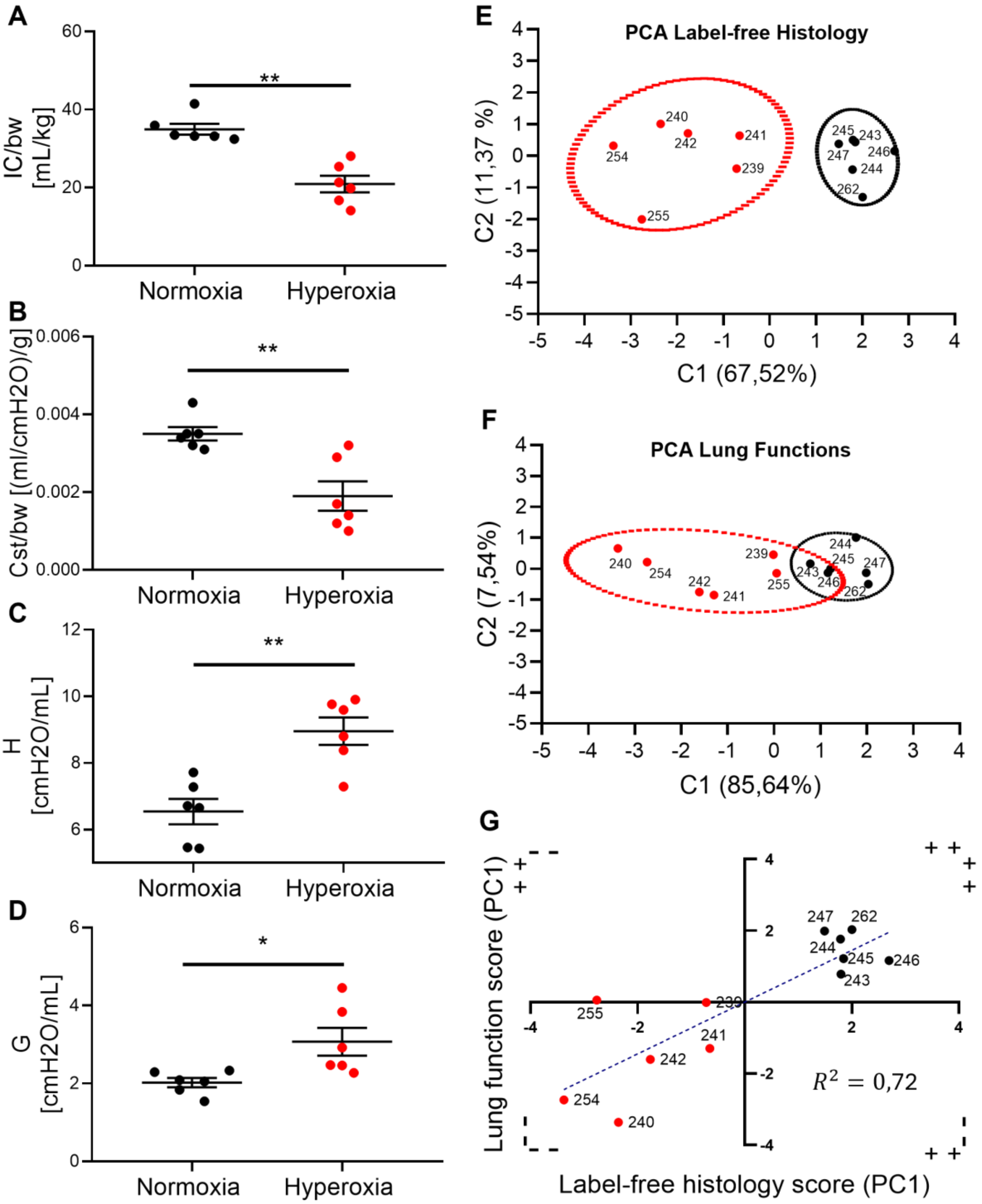

Figure 4.19 Label-free histomorphological features correlate with lung function metrics. (A) Inspiratory capacity, **(B)** static compliance, both normalized to body weight, **(C)** lung tissue elastance, **(D)** lung tissue damping, measured with Flexivent at PND7 in preterm rabbit managed with normoxia 21% O$_2$ or hyperoxia 95% O$_2$. Statistical tests for differences between conditions were chosen based on the results of the Shapiro-Wilk test for normality and the F-test for variance: **(A)** Mann-Whitney test; Median ± IQR **(B-C)** Unpaired t test; Mean ± SEM **(D)** Welch's test; Mean ± SEM. **(E)** PCA based on label-free histological parameters obtained from each sample, comparing normoxia (black dots) and hyperoxia (red dots). All parameters were included, except ADVT%, which was not relevant to BPD. For collagen, the parenchymal measurement was used. **(F)** PCA based on lung function parameters from the Flexivent analysis, comparing normoxia (black dots) and hyperoxia (red dots) conditions. **(G)** Correlation between the overall histological and functional profiles. The Histological Score (PC1) and Functional Score (PC1) were derived from the first principal component of standardized label-free histological and functional data, respectively. Pearson's r = 0.85, p = 0.0004. Linear regression: Y = 0,7245*X - 7,735e^{-8}, R^2 = 0,72.

5 - DISCUSSION

This work presents a label-free, multimodal imaging approach that integrates TPEF, SHG, and FLIM to qualitatively and quantitatively assess lung parenchymal alterations in a preterm rabbit model of hyperoxia-induced BPD. By leveraging tissue's intrinsic signals, including autofluorescence intensity and lifetime, as well as SHG of collagen, this tool effectively highlights key pathological features associated with hyperoxia. These include increased TD, alveolar exudates, fibrillar collagen accumulation, vascular remodeling, and alveolar simplification. Additionally, it reveals changes in fluorescence properties that reflect tissue's molecular composition and its response to hyperoxic injury. The method provides a robust, non-destructive, high-resolution integrative approach to conventional histology and immunolabeling for lung tissue characterization in preclinical BPD research.

BPD is a chronic lung disease affecting extremely preterm infants[17] causing long-term respiratory complications[54,86,239]. Despite advances in neonatal care, its incidence remains high[141], and current treatments have limited efficacy[112], underscoring the need for a deeper understanding and novel therapies. Ethical constraints and improved survival have reduced access to human tissue, making animal models crucial for studying BPD and testing new interventions[93].

The rabbit model offers a valuable compromise between small and large animals, combining practical advantages with human-like lung development and the ability to mimic prematurity[149,162]. Moreover, exposing preterm rabbits (28 GA) to 95% oxygen for seven days effectively reproduces the histopathological features of human BPD, including impaired alveolar and vascular development, inflammation, and ECM remodeling[87].

However, rabbit models have some limitations, such as the scarcity of validated antibodies[87], which restricts analyses mainly to functional and histological endpoints, with the latter often requiring multiple staining and tissue sections to detect key features of BPD.

Here, I propose a non-destructive, label-free method leveraging two-photon excitation and multichannel optical system to simultaneously study BPD relevant features in a single unlabeled tissue slice. By exciting at 780 nm and detecting tissue autofluorescence in the

470-570 nm range, the tool revealed lung morphology comparable to H&E staining, without the need for external dyes. Moreover, it highlighted distinctive cellular features in airways epithelium, vessels, and exudates through intrinsic nuclear-cytoplasmic contrast.

Through an optimized analysis of autofluorescence signal, the method showed an increased tissue density associated with septal thickening, as well as elevated alveolar exudates in hyperoxia-exposed lungs. These observations align with findings from H&E-stained sections and prior reports of hyperoxic lung injury in preterm rabbits[149,164,166].

Moreover, alveolar exudates exhibited distinct label-free signatures that may reflect their composition and allow for speculative identification. However, since immunostaining was not performed to confirm their identity, the analysis focused on the exudate-occupied area as a histological marker of inflammation. The strong correlation between autofluorescence-based quantification of alveolar exudates and ALI scores from H&E sections supports the robustness of this method, even though quantifying alveolar exudates reflects only a subset of the parameters in the full ALI score. Notably, alveolar exudate's area varied widely across hyperoxic samples and within individual tissue sections, reflecting a heterogeneous inflammatory pattern.

Autofluorescence intensity decreased in lungs exposed to high oxygen, reflecting molecular changes, since the signal depends on the biochemical composition and intrinsic fluorescence of endogenous molecules. Therefore, intensity variations may serve as fingerprints of oxygen-induced injury[187], although further studies are needed to clarify the molecular basis.

Fibrillar collagens, particularly types I and III, are key ECM components that support lung structure and regulate tissue stiffness[240]. During normal development, collagen increases to support septation[241], but in BPD this process is disrupted, resulting in thickened saccular walls and increased interstitial collagen, consistent with mild fibrosis[241]. These features have been reported in both human[54,88,241] and animal BPD models, including hyperoxia-exposed preterm rabbits[149,162,169,232]. The SHG signal, validated by PSR fluorescence for collagen specificity[235], revealed increased fibrillar collagen deposition in alveolar septa and interstitial spaces in hyperoxia-exposed rabbits. In normoxic animals, SHG signals were mostly localized to secondary crests, indicating an active role of fibrillar collagen in alveolarization. These findings were supported by qualitative evaluation of Col1a1 immunohistochemistry and PSR staining on consecutive sections. Semi-automated SHG analysis confirmed the accumulation of both total and parenchymal collagen in hyperoxic lungs. Notably, SHG detects only fibrillar collagens, not non-fibrillar types such as type IV[187] which is prominent in the basement membrane.

Lung development depends on a coordinated interplay between alveolarization and vascularization[3,94]. In BPD, this regulation is disrupted, leading to simplified alveolar structures and marked vascular defects that contribute to long-term respiratory morbidity[88,95,96]. Abnormal angiogenesis and vascular remodeling, including increased arterial muscularization and tone[238], contribute to pulmonary arterial hypertension, a serious BPD complication associated with increased infant morbidity and mortality[101]. Autofluorescence and SHG enabled identification of blood vessels and their structural layers, validated by CD31 and α-SMA immunofluorescence in corresponding sections. The tool revealed significantly increased MT% in hyperoxia-exposed lungs, matching values from conventional histology and previous studies[164,165,169]. No difference was found in tunica adventitia thickness. Notably, microvessels like capillaries cannot be visualized due to their lack of fibrillar collagen. Interestingly, spectral and lifetime similarities between RBCs and certain autofluorescent spots suggest these may represent capillaries containing erythrocytes. If validated, these could serve as surrogate markers of capillary density.

The combined autofluorescence and SHG signals also revealed significantly reduced alveolar density in hyperoxic lungs, consistent with previously described alveolar simplification[164,165]. Notably, this label-free metric strongly correlated with RAC measured from H&E-stained sections, an independent parameter of alveolar development, further validating the approach.

FLIM provided an additional contrast layer, revealing a shift toward longer autofluorescence lifetimes in hyperoxic lungs. This change represents a sensitive intrinsic signature of hyperoxia's effects, which could be used to distinguish between hyperoxic and normoxic lungs, especially in case of automated analysis. In our case, measurements were performed using a bandpass filter to select emission wavelengths in the 420-460 range, where mainly NAD(P)H fluorescence was expected[196]. NAD(P)H fluorescence lifetime is a well-established marker of metabolism and redox state in cells and tissues[195–198,223]. Traditionally, the observed shift toward longer lifetime is interpreted as a relative increase in the enzyme-bound fraction of NAD(P)H compared to the free fraction, as a consequence of enhanced OXPHOS activity (For details, see section 3.1.2.2). However, interpreting NAD(P)H fluorescence lifetimes within the Glycolysis/OXPHOS framework in complex biological systems requires caution and thorough investigation. It is important to rule out potential contamination from ECM components[224], to account for the variable expression of NAD(P)H-binding enzymes with distinct lifetimes, and to consider the contribution of NADPH, which is primarily involved in ROS production and antioxidant mechanisms. Therefore, at this stage, fluorescence lifetime represents an additional intrinsic feature that reflects molecular changes and allows for distinguishing normoxic from hyperoxic tissue, whose biological significance requires careful interpretation from a biophysical perspective.

Importantly, using all optimized label-free features, the tool successfully discriminated between normoxic and hyperoxic preterm rabbits and revealed varying histological severity among hyperoxic animals. A correlation was found between histological severity and lung function impairment measured with FlexiVent, confirming the method's robustness even at the individual animal level.

This label-free imaging approach offers several advantages, including high-resolution visualization of lung structures without staining or immunolabeling, and simultaneous access to cellular, extracellular, and molecular features. It also allows for re-analysis of the same tissue sections by using H&E and immunolabelling, providing a more comprehensive view of lung pathology. Moreover, from the outset, the quantitative approach was designed for future optimization, favoring signal-based metrics that rely on intensity contrasts and combinations of autofluorescence and SHG signals over pathologist-dependent recognition, while maintaining validation against expert pathological assessments. This strategy aims to support future automation and broader usability in preclinical studies. Eventually, this method could be adapted for live tissues and 3D imaging.

Despite these strengths, the approach has limitations. While it yields valuable quantitative data on tissue structure, it lacks the molecular specificity of immunolabeling. Additionally, autofluorescence-based measurements can be affected by highly fluorescent components like RBCs and spots, requiring careful signal processing. Future improvements could include hyperspectral imaging or complementary molecular probes to enhance specificity. Expanded use of FLIM may also help, as this technique has been applied for collagen type discrimination[211], oxidative stress detection[242], and inflammation characterization[243]. Another limitation may concern the acquisition system, which, although optimized for high resolution mosaic scanning to ensure representative tissue coverage, does not encompass the entire section.

The use of fixed tissues may be considered another limitation, as fixation can alter intrinsic signals, especially relevant in clinical contexts[244,245]. While label-free methods do not require fixed and paraffin-embedded tissues, these formats offer practical benefits like structural preservation and compatibility with histology. This facilitates multimodal analyses and was crucial for validation during early tool development. Future work will explore applications to live tissue imaging.

6 - FUTURE PERSPECTIVES

This research can be further developed along four key directions:

- Broader applicability: The imaging tool could be extended to characterize additional animal models used in pharmacological studies of BPD, thereby enhancing its utility in preclinical research. Furthermore, this method can be used for the comprehensive assessment of drug effects on both specific features and the overall phenotype, as all components are simultaneously analyzed within the same tissue. PCA readouts offer a visual means to detect potential phenotype reversion or attenuation of disease severity.

- Optimization of the acquisition system to enable automatic scanning of the entire tissue section: Implementing an autofocus system would facilitate automatic acquisition of larger mosaic images, potentially covering the entire tissue section. To make this feasible, the setup must be optimized to reduce scanning time (currently, it takes approximately 1 hour to acquire ten mosaics covering 2.7 mm^2 per sample).

- Automation of analysis: Automating the analysis workflow would significantly accelerate data processing and reduce operator dependence. In this context, integration with Visiopharm, a software platform powered by AI for digital histological image analysis, represents a promising avenue for improvement.

- Application to viable and thick tissue samples: the tool could be adapted for use in live or thick tissue specimens, such as Precision-Cut Lung Slices (PCLS). This 3D ex-vivo model is valuable for preclinical drug screening and may contribute to reducing animal usage.

Preliminary progress has already been made along the first of these directions. In the final phase of my research, Chiesi Farmaceutici S.p.A. generously provided lung slices from a recently developed and validated preterm rabbit model, with the aim of further characterizing this system. This model was specifically designed to better replicate the phenotype of mild BPD by using less invasive oxygen exposure protocols, which more closely mirror those applied in NICUs, while also enabling the study of long-term outcomes. Lung slices were obtained from rabbit pups delivered preterm at 28 GA and subsequently exposed to 70% oxygen (hyperoxia) for 14 days. Two control conditions were included: exposure to normoxia (21% O_2 for 14 days) to isolate the effects of hyperoxia, and age-matched term-born rabbits to evaluate the long-term impact of prematurity (**Figure 6.1 A**). At this stage, the label-free tool has been applied to characterize n = 4-5 rabbits per condition, and preliminary data appears promising.

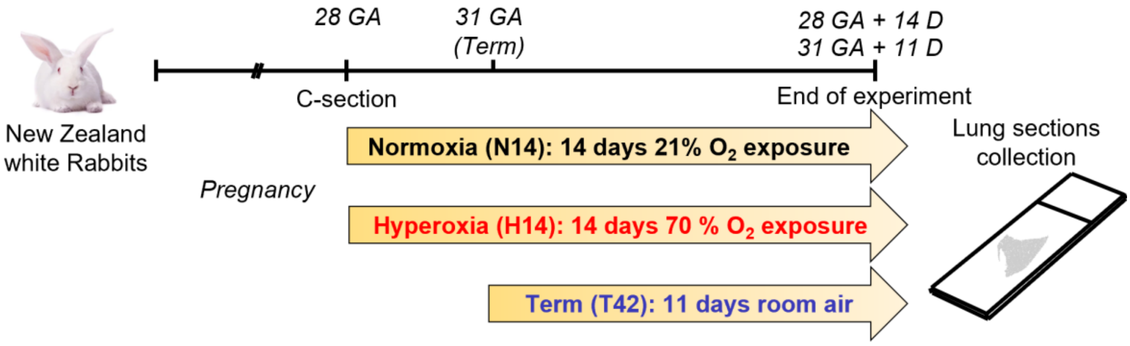

Figure 6.1 Application of the label-free tool to preliminary characterize mild BPD model (A) Lung sections were obtained from prematurely delivered rabbits at 28 GA and subsequently exposed to either normoxia (21% O_2, n=5) or hyperoxia (70% O_2, n=5) for 14 days to mimic mild BPD or from a full term rabbit (31 days) and maintained at room air for 11 days (n=4).

BIBLIOGRAPHY

1. Smith, L. J., McKay, K. O., van Asperen, P. P., Selvadurai, H. & Fitzgerald, D. A. Normal development of the lung and premature birth. *Paediatr Respir Rev* **11**, (2010).
2. Kajekar, R. Environmental factors and developmental outcomes in the lung. *Pharmacol Ther* **114**, (2007).
3. Schittny, J. C. Development of the lung. *Cell Tissue Res* **367**, (2017).
4. Burri, P. H. Fetal and postnatal development of the lung. *Annu Rev Physiol* **46**, (1984).
5. Cardoso, W. V. & Lü, J. Regulation of early lung morphogenesis: Questions, facts and controversies. *Development* **133** (2006).
6. Burri, P. H. Development and Growth of the Human Lung. in *Compr Physiol* (1985).
7. Kitaoka, H., Burri, P. H. & Weibel, E. R. Development of the human fetal airway tree: Analysis of the numerical density of airway endtips. *Anat Rec* **244**, (1996).
8. Zeltner, T. B., Caduff, J. H., Gehr, P., Pfenninger, J. & Burri, P. H. The postnatal development and growth of the human lung. I. Morphometry. *Respir Physiol* **67**, (1987).
9. Burri, P. H. Postnatal Growth and Maturation of the Lung. *Chest* **67**, (1975).
10. Burri, P. H. The postnatal growth of the rat lung III. Morphology. *Anat Rec* **180**, (1974).
11. Lindahl, P. *et al.* Alveogenesis failure in PDGF-A-deficient mice is coupled to lack of distal spreading of alveolar smooth muscle cell progenitors during lung development. *Development* **124**, (1997).
12. Narayanan, M. *et al.* Alveolarization continues during childhood and adolescence: New evidence from helium-3 magnetic resonance. *Am J Respir Crit Care Med* **185**, (2012).
13. Herring, M. J., Putney, L. F., Wyatt, G., Finkbeiner, W. E. & Hyde, D. M. Growth of alveoli during postnatal development in humans based on stereological estimation. *Am J Physiol Lung Cell Mol Physiol* **307**, (2014).
14. Hyde, D. M. *et al.* Alveoli increase in number but not size from birth to adulthood in rhesus monkeys. *Am J Physiol Lung Cell Mol Physiol* **293**, (2007).
15. Schittny, J. C., Mund, S. I. & Stampanoni, M. Evidence and structural mechanism for late lung alveolarization. *Am J Physiol Lung Cell Mol Physiol* **294**, (2008).
16. Rippa, A. L., Alpeeva, E. V., Vasiliev, A. V. & Vorotelyak, E. A. Alveologenesis: What governs secondary septa formation. *Int J Mol Sci* **22**, (2021).
17. Thébaud, B. *et al.* Bronchopulmonary dysplasia. *Nat Rev Dis Primers* **5**, (2019).

18. Goldenberg, R. L., Culhane, J. F., Iams, J. D. & Romero, R. Epidemiology and causes of preterm birth. *Lancet* **371**, (2008).

19. Doyle, L. W. *et al.* Ventilation in Extremely Preterm Infants and Respiratory Function at 8 Years. *N Engl J Med* **377**, (2017).

20. Bacha, L. T., Hailu, W. B. & Tesfaye Geta, E. Clinical outcome and associated factors of respiratory distress syndrome among preterm neonates admitted to the neonatal intensive care unit of Adama Hospital and Medical College. *SAGE Open Med* **10**, (2022).

21. Behnke, J. *et al.* Non-Invasive Ventilation in Neonatology. *Dtsch Arztebl Int* **116**, (2019).

22. Jobe, A. H. & Bancalari, E. Bronchopulmonary dysplasia. in *Am J Respir Crit Care Med* **163**, (2001).

23. De Winter, J. P., De Vries, M. A. G. & Zimmermann, L. J. I. Clinical practice: Noninvasive respiratory support in newborns. *Eur J Pediatr* **169**, (2010).

24. Carvalho, C. G., Silveira, R. C. & Procianoy, R. S. Ventilator-induced lung injury in preterm infants. *Rev Bras Ter Intensiva* **25**, (2013).

25. Sweet, D. G. *et al.* European Consensus Guidelines on the Management of Respiratory Distress Syndrome: 2022 Update. *Neonatology* **120**, (2023).

26. Subramaniam, P., Ho, J. J. & Davis, P. G. Prophylactic or very early initiation of continuous positive airway pressure (CPAP) for preterm infants. *Cochrane Database Syst Rev* **10**, (2021).

27. Morley, C. J. *et al.* Nasal CPAP or Intubation at Birth for Very Preterm Infants. *N Engl J Med* **358**, (2008).

28. Dunn, M. S. *et al.* Randomized trial comparing 3 approaches to the initial respiratory management of preterm neonates. *Pediatrics* **128**, (2011).

29. Lemyre, B., Laughon, M., Bose, C. & Davis, P. G. Early nasal intermittent positive pressure ventilation (NIPPV) versus early nasal continuous positive airway pressure (NCPAP) for preterm infants. *Cochrane Database Syst Rev* **12**, (2016).

30. Lemyre, B., Davis, P. G., De Paoli, A. G. & Kirpalani, H. Nasal intermittent positive pressure ventilation (NIPPV) versus nasal continuous positive airway pressure (NCPAP) for preterm neonates after extubation. *Cochrane Database Syst Rev* **2**, (2017).

31. Yang, J. *et al.* Efficacy and safety of different noninvasive ventilation strategies for postextubation respiratory support in Neonatal Respiratory Distress Syndrome: a systematic review and network meta-analysis. *Front Pediatr* **12**, (2024).

32. Hodgson, K. A., Wilkinson, D., De Paoli, A. G. & Manley, B. J. Nasal high flow therapy for primary respiratory support in preterm infants. *Cochrane Database Syst Rev* **2023**, (2023).

33. Fujiwara, T. *et al.* Artificial surfactant therapy in hyaline-membrane disease. *Lancet* **315**, (1980).

34. Principi, N., Di Pietro, G. M. & Esposito, S. Bronchopulmonary dysplasia: Clinical aspects and preventive and therapeutic strategies. *J Transl Med* **16**, (2018).

35. Kribs, A., Roberts, K. D., Trevisanuto, D., O'Donnell, C. & Dargaville, P. A. Surfactant delivery strategies to prevent bronchopulmonary dysplasia. *Semin Perinatol* **47**, (2023).

36. De Luca, D., Shankar-Aguilera, S. & Bancalari, E. LISA/MIST: Complex clinical problems almost never have easy solutions. *Semin Fetal Neonatal Med* **26**, (2021).

37. Abdel-Latif, M. E., Davis, P. G., Wheeler, K. I., De Paoli, A. G. & Dargaville, P. A. Surfactant therapy via thin catheter in preterm infants with or at risk of respiratory distress syndrome. *Cochrane Database Syst Rev* **5**, (2021).

38. Yeung, T. Y. *et al.* Surfactant delivery via thin catheter in preterm infants: A systematic review and meta-analysis. *PLoS One* **18**, (2023).

39. De Luca, D. & de Winter, J. P. Less invasive surfactant administration: all that glitters is not gold. *Eur J Pediatr* **179**, (2020).

40. N.N., Finer. *et al.* An open label, pilot study of aerosurf® combined with nCPAP to prevent RDS in preterm neonates. *J Aerosol Med Pulm Drug Deliv* **23**, (2010).

41. Roberts, K. D. *et al.* Laryngeal Mask Airway for Surfactant Administration in Neonates: A Randomized, Controlled Trial. *J Pediatr* **193**, (2018).

42. Jobe, A. H., Kemp, M. W., Kamath-Rayne, B. & Schmidt, A. F. Antenatal corticosteroids for low and middle income countries. *Semin Perinatol* **43**, (2019).

43. McGoldrick, E., Stewart, F., Parker, R. & Dalziel, S. R. Antenatal corticosteroids for accelerating fetal lung maturation for women at risk of preterm birth. *Cochrane Database Syst Rev* **12**, (2020).

44. Roberts, D., Brown, J., Medley, N. & Dalziel, S. R. Antenatal corticosteroids for accelerating fetal lung maturation for women at risk of preterm birth. *Cochrane Database Syst Rev* **3**, (2017).

45. Ninan, K., Liyanage, S. K., Murphy, K. E., Asztalos, E. V. & McDonald, S. D. Evaluation of Long-term Outcomes Associated With Preterm Exposure to Antenatal Corticosteroids. *JAMA Pediatr* **176**, (2022).

46. Bonadies, L., Cavicchiolo, M. E., Priante, E., Moschino, L. & Baraldi, E. Prematurity and BPD: what general pediatricians should know. *Eur J Pediatr* **182**, (2023).

47. Gibson, A. M. & Doyle, L. W. Respiratory outcomes for the tiniest or most immature infants. *Semin Fetal Neonatal Med* **19**, (2014).

48. Northway, W. H., Rosan, R. C. & Porter, D. Y. Pulmonary Disease Following Respirator Therapy of Hyaline-Membrane Disease. *N Engl J Med* **276**, (1967).

49. Abman, S. H., Bancalari, E. & Jobe, A. The evolution of bronchopulmonary dysplasia after 50 years. *Am J Respir Crit Care Med* **195**, (2017).

50. Brick, J., Moreira, A. & Bierwirth, N. Rates of bronchopulmonary dysplasia in very low birth weight neonates: a systematic review and meta-analysis. *Am J Med Sci* **367**, (2024).

51. Di Filippo, P. *et al.* Pulmonary Outcomes in Children Born Extremely and Very Preterm at 11 Years of Age. *Front Pediatr* **9**, (2021).

52. Gilfillan, M., Bhandari, A. & Bhandari, V. Diagnosis and management of bronchopulmonary dysplasia. *The BMJ* **375**, (2021).

53. Jobe, A. H. & Bancalari, E. NICHD / NHLBI / ORD Workshop Summary. *Am J Respir Crit Care Med* **163**, (2001).

54. Kalikkot Thekkeveedu, R., Guaman, M. C. & Shivanna, B. Bronchopulmonary dysplasia: A review of pathogenesis and pathophysiology. *Respir Med* **132**, (2017).

55. Morrow, L. A. *et al.* Antenatal determinants of bronchopulmonary dysplasia and late respiratory disease in preterm infants. *Am J Respir Crit Care Med* **196**, (2017).

56. Isayama, T. *et al.* Adverse Impact of Maternal Cigarette Smoking on Preterm Infants: A Population-Based Cohort Study. *Am J Perinatol* **32**, (2015).

57. Sharma, D., Shastri, S. & Sharma, P. Intrauterine Growth Restriction: Antenatal and Postnatal Aspects. *Clin Med Insights Pediatr* **10**, (2016).

58. Bose, C. *et al.* Fetal growth restriction and chronic lung disease among infants born before the 28th week of gestation. *Pediatrics* **124**, (2009).

59. Gortner, L., Reiss, I. & Hilgendorff, A. Bronchopulmonary dysplasia and intrauterine growth restriction. *Lancet* **368**, (2006).

60. Bhandari, V. *et al.* Familial and genetic susceptibility to major neonatal morbidities in preterm twins. *Pediatrics* **117**, (2006).

61. Parker, R. A., Lindstrom, D. P. & Cotton, R. B. Evidence from twin study implies possible genetic susceptibility to bronchopulmonary dysplasia. *Semin Perinatol* **20**, (1996).

62. Dankhara, N., Holla, I., Ramarao, S. & Kalikkot Thekkeveedu, R. Bronchopulmonary Dysplasia: Pathogenesis and Pathophysiology. *J Clin Med* **12**, (2023).

63. Czikk, M. J., McCarthy, F. P. & Murphy, K. E. Chorioamnionitis: From pathogenesis to treatment. *Clin Microbiol Infect* **17**, (2011).

64. Bo Hyun Yoon *et al.* Amniotic fluid cytokines (interleukin-6, tumor necrosis factor-α, interleukin-1β, and interleukin-8) and the risk for the development of bronchopulmonary dysplasia. *Am J Obstet Gynecol* **177**, (1997).

65. Villamor-Martinez, E. *et al.* Association of Chorioamnionitis with Bronchopulmonary Dysplasia among Preterm Infants: A Systematic Review, Meta-analysis, and Metaregression. *JAMA Netw Open* **2**, (2019).

66. Ballard, A. R., Mallett, L. H., Pruszynski, J. E. & Cantey, J. B. Chorioamnionitis and subsequent bronchopulmonary dysplasia in very-low-birth weight infants: A 25-year cohort. *J Perinatol* **36**, (2016).

67. Van Marter, L. J. *et al.* Chorioamnionitis, mechanical ventilation, and postnatal sepsis as modulators of chronic lung disease in preterm infants. *J Pediatr* **140**, (2002).

68. Lahra, M. M., Beeby, P. J. & Jeffery, H. E. Intrauterine inflammation, neonatal sepsis, and chronic lung disease: A 13-year hospital cohort study. *Pediatrics* **123**, (2009).

69. Jobe, A. H. Effects of chorioamnionitis on the fetal lung. *Clin Perinatol* **39**, (2012).

70. Collaco, J. M. & McGrath-Morrow, S. A. Respiratory phenotypes for preterm infants, children, and adults: Bronchopulmonary dysplasia and more. *Ann Am Thorac Soc* **15**, (2018).

71. Binet, M. E., Bujold, E., Lefebvre, F., Tremblay, Y. & Piedboeuf, B. Role of gender in morbidity and mortality of extremely premature neonates. *Am J Perinatol* **29**, (2012).

72. Jensen, E. A. & Schmidt, B. Epidemiology of bronchopulmonary dysplasia. *Birth Defects Res A Clin Mol Teratol* **100**, (2014).

73. Balany, J. & Bhandari, V. Understanding the impact of infection, inflammation, and their persistence in the pathogenesis of bronchopulmonary dysplasia. *Front Med* **2**, (2015).

74. Kolls, J. K. Commentary: Understanding the impact of infection, inflammation and their persistence in the pathogenesis of bronchopulmonary dysplasia. *Front Med* **4**, (2017).

75. Asikainen, T. M. & White, C. W. Antioxidant defenses in the preterm lung: Role for hypoxia-inducible factors in BPD? *Toxicol Appl Pharmacol* **203**, (2005).

76. Viña, J. *et al.* L-cysteine and glutathione metabolism are impaired in premature infants due to cystathionase deficiency. *Am J Clin Nutr* **61**, (1995).

77. Choi, Y. *et al.* Oxygen toxicity to the immature lung—part i: Pathomechanistic understanding and preclinical perspectives. *Int J Mol Sci* **22**, (2021).

78. Basha, S., Surendran, N. & Pichichero, M. Immune responses in neonates. *Expert Rev Clin Immunol* **10**, (2014).

79. Klinger, G. *et al.* Outcome of early-onset sepsis in a national cohort of very low birth weight infants. *Pediatrics* **125**, (2010).

80. Massaro, G. D., McCoy, L. & Massaro, D. Postnatal undernutrition slows development of bronchiolar epithelium in rats. *Am J Physiol Regul Integr Comp Physiol* **255**, (1988).

81. Gaultier, C. Malnutrition and lung growth. *Pediatr Pulmonol.* **10**, (1991).

82. Mataloun, M. M. G. B., Rebello, C. M., Mascaretti, R. S., Dohlnikoff, M. & Leone, C. R. Pulmonary responses to nutritional restriction and hyperoxia in premature rabbits. *J Pediatr (Rio J)* **82**, (2006).

83. Goldberg, D. L. *et al.* Identifying Malnutrition in Preterm and Neonatal Populations: Recommended Indicators. *J Acad Nutr Diet* **118**, (2018).

84. Speer, C. P. Inflammation and bronchopulmonary dysplasia: A continuing story. *Semin Fetal Neonatal Med* **11**, (2006).

85. Shahzad, T., Radajewski, S., Chao, C.-M., Bellusci, S. & Ehrhardt, H. Pathogenesis of bronchopulmonary dysplasia: when inflammation meets organ development. *Mol Cell Pediatr* **3**, (2016).

86. Hilgendorff, A. & O'Reilly, M. A. Bronchopulmonary dysplasia early changes leading to long-term consequences. *Front Med* **2**, (2015).

87. Salaets, T., Gie, A., Tack, B., Deprest, J. & Toelen, J. Modelling Bronchopulmonary Dysplasia in Animals: Arguments for the Preterm Rabbit Model. *Curr Pharm des* **23**, (2017).

88. Coalson, J. J. Pathology of new bronchopulmonary dysplasia. *Semin Neonatol* **8**, (2003).

89. Husain, A. N., Siddiqui, N. H. & Stocker, J. T. Pathology of arrested acinar development in postsurfactant bronchopulmonary dysplasia. *Hum Pathol* **29**, (1998).

90. Hislop, A. A., Wigglesworth, J. S., Desai, R. & Aber, V. The effects of preterm delivery and mechanical ventilation on human lung growth. *Early Hum Dev* **15**, (1987).

91. Van Velzen, D. & Van Velzen, D. Ventilator-related pathology in the extremely immature lung. *Pathology* **21**, (1989).

92. Margraf, L. R., Tomashefski, J. F., Bruce, M. C. & Dahms, B. B. Morphometric analysis of the lung in bronchopulmonary dysplasia. *Am Rev Respir Dis* **143**, (1991).

93. Jobe, A. H. The New BPD. *Neoreviews* **7**, (2006).

94. Lignelli, E., Palumbo, F., Myti, D. & Morty, R. E. Recent advances in our understanding of the mechanisms of lung alveolarization and bronchopulmonary dysplasia. *Am J Physiol Lung Cell Mol Physiol* **317**, (2019).

95. De Paepe, M. E. *et al.* Growth of pulmonary microvasculature in ventilated preterm infants. *Am J Respir Crit Care Med* **173**, (2006).

96. Bhatt, A. J. *et al.* Disrupted pulmonary vasculature and decreased vascular endothelial growth factor, Flt-1, and TIE-2 in human infants dying with bronchopulmonary dysplasia. *Am J Respir Crit Care Med* **164**, (2001).

97. Mosca, F., Colnaghi, M. & Fumagalli, M. BPD: Old and new problems. *J Matern Fetal Neonatal Med* **24**, (2011).

98. Thibeault, D. W., Truog, W. E. & Ekekezie, I. I. Acinar Arterial Changes with Chronic Lung Disease of Prematurity in the Surfactant Era. *Pediatr Pulmonol* **36**, (2003).

99. Hislop, A. A. & Haworth, S. G. Pulmonary vascular damage and the development of cor pulmonale following hyaline membrane disease. *Pediatr Pulmonol* **9**, (1990).

100. Davidson, L. M. & Berkelhamer, S. K. Bronchopulmonary dysplasia: Chronic lung disease of infancy and long-term pulmonary outcomes. *J Clin Med* **6**, (2017).

101. Schmidt, A. R. & Ramamoorthy, C. Bronchopulmonary dysplasia. *Paediatr Anaesth* **32**, (2022).

102. Greenough, A. & Pahuja, A. Updates on functional characterization of bronchopulmonary dysplasia - the contribution of lung function testing. *Front Med* **2**, (2015).

103. Baraldi, E., Filippone, M., Trevisanuto, D., Zanardo, V. & Zacchello, F. Pulmonary function until two years of life in infants with bronchopulmonary dysplasia. *Am J Respir Crit Care Med* **155**, (1997).

104. Vendettuoli, V. *et al.* Positional effects on lung mechanics of ventilated preterm infants with acute and chronic lung disease. *Pediatr Pulmonol* **50**, (2015).

105. May, C. *et al.* Lung function abnormalities in infants developing bronchopulmonary dysplasia. *Arch Dis Child* **96**, (2011).

106. Smith, V. C. *et al.* Rehospitalization in the first year of life among infants with bronchopulmonary dysplasia. *J Pediatr* **144**, (2004).

107. Collaco, J. M., Eldredge, L. C. & McGrath-Morrow, S. A. Long-term pulmonary outcomes in BPD throughout the life-course. *J Perinatol* (2024).

108. Islam, J. Y., Keller, R. L., Aschner, J. L., Hartert, T. V. & Moore, P. E. Understanding the short- and long-term respiratory outcomes of prematurity and bronchopulmonary dysplasia. *Am J Respir Crit Care Med* **192**, (2015).

109. Natarajan, G. *et al.* Outcomes of extremely low birth weight infants with bronchopulmonary dysplasia: Impact of the physiologic definition. *Early Hum Dev* **88**, (2012).

110. Singer, L., Yamashita, T., Lilien, L., Collin, M. & Baley, J. A longitudinal study of developmental outcome of infants with bronchopulmonary dysplasia and very low birth weight. *Pediatrics* **100**, (1997).

111. Short, E. J. *et al.* Cognitive and academic consequences of bronchopulmonary dysplasia and very low birth weight: 8-year-old outcomes. *Pediatrics* **112**, (2003).

112. Durlak, W. & Thébaud, B. BPD: Latest Strategies of Prevention and Treatment. *Neonatology* **121**, (2024).

113. Michael, Z., Spyropoulos, F., Ghanta, S. & Christou, H. Bronchopulmonary Dysplasia: An Update of Current Pharmacologic Therapies and New Approaches. *Clin Med Insights Pediatr* **12**, (2018).

114. Oluwole-Ojo, T., Harris, C. & Greenough, A. Advances in the pharmacological management of bronchopulmonary dysplasia: an update of the literature. *Expert Opin Pharmacother* **25**, (2024).

115. Schmidt, B. *et al.* Caffeine Therapy for Apnea of Prematurity. *N Engl J Med* **354**, (2006).

116. Schmidt, B. *et al.* Long-Term Effects of Caffeine Therapy for Apnea of Prematurity. *N Engl J Med* **357**, (2007).

117. Davis, P. G. *et al.* Caffeine for Apnea of Prematurity Trial: Benefits May Vary in Subgroups. *J Pediatr* **156**, (2010).

118. Tyson, J. E. *et al.* Vitamin A supplementation for extremely-low-birth-weight infants. National Institute of Child Health and Human Development Neonatal Research Network. *N Engl J Med* **340**, (1999).

119. Rakshasbhuvankar, A. A. *et al.* Enteral vitamin A for reducing severity of bronchopulmonary dysplasia: A randomized trial. *Pediatrics* **147**, (2021).

120. Meyer, S. *et al.* Early postnatal high-dose fat-soluble enteral vitamin A supplementation for moderate or severe bronchopulmonary dysplasia or death in extremely low birthweight infants (NeoVitaA): a multicentre, randomised, parallel-group, double-blind, placebo-controlled, investigator-initiated phase 3 trial. *Lancet Respir Med* **12**, (2024).

121. Strueby, L. & Thébaud, B. Novel therapeutics for bronchopulmonary dysplasia. *Curr Opin Pediatr* **30** (2018).

122. Doyle, L. W., Cheong, J. L., Ehrenkranz, R. A. & Halliday, H. L. Early (< 8 days) systemic postnatal corticosteroids for prevention of bronchopulmonary dysplasia in preterm infants. *Cochrane Database Syst Rev* **10**, (2017).

123. Doyle, L. W. *et al.* Low-dose dexamethasone facilitates extubation among chronically ventilator-dependent infants: A multicenter, international, randomized, controlled trial. *Pediatrics* **117**, (2006).

124. Doyle, L. W., Cheong, J. L., Hay, S., Manley, B. J. & Halliday, H. L. Late (≥ 7 days) systemic postnatal corticosteroids for prevention of bronchopulmonary dysplasia in preterm infants. *Cochrane Database Syst Rev* **2025**, (2021).

125. van de Loo, M. *et al.* Corticosteroids for the prevention and treatment of bronchopulmonary dysplasia: an overview of systematic reviews. *Cochrane Database Syst Rev* **2024**, (2024).

126. Gilfillan, M. A., Kiladejo, A. & Bhandari, V. Current and Emerging Therapies for Prevention and Treatment of Bronchopulmonary Dysplasia in Preterm Infants. *Pediatric Drugs* **27**, (2025).

127. Shinwell, E. S., Portnov, I., Meerpohl, J. J., Karen, T. & Bassler, D. Inhaled corticosteroids for bronchopulmonary dysplasia: A meta-analysis. *Pediatrics* **138**, (2016).

128. Bassler, D. *et al.* Long-Term Effects of Inhaled Budesonide for Bronchopulmonary Dysplasia. *N Engl J Med* **378**, (2018).

129. Bassler, D. *et al.* Early Inhaled Budesonide for the Prevention of Bronchopulmonary Dysplasia. *N Engl J Med* **373**, (2015).

130. Manley, B. J. *et al.* Intratracheal Budesonide Mixed With Surfactant for Extremely Preterm Infants. *JAMA* **332**, (2024).

131. Zhang, S., Mulder, C., Riddle, S., Song, R. & Yue, D. Mesenchymal stromal/stem cells and bronchopulmonary dysplasia. *Front Cell Dev Biol* **11**, (2023).

132. Brown, C. *et al.* Mesenchymal stem cells: Cell therapy and regeneration potential. *J Tissue Eng Regen Med* **13** (2019).

133. Ahn, S. Y. *et al.* Stem cells for bronchopulmonary dysplasia in preterm infants: A randomized controlled phase II trial. *Stem Cells Transl Med* **10**, (2021).

134. Augustine, S. *et al.* Mesenchymal Stromal Cell Therapy in Bronchopulmonary Dysplasia: Systematic Review and Meta-Analysis of Preclinical Studies. *Stem Cells Transl Med* **6**, (2017).

135. Xi, Y., Ju, R. & Wang, Y. Mesenchymal Stem Cell-Derived Extracellular Vesicles for the Treatment of Bronchopulmonary Dysplasia. *Front Pediatr* **10**, (2022).

136. Mandell, E. W., Kratimenos, P., Abman, S. H. & Steinhorn, R. H. Drugs for the Prevention and Treatment of Bronchopulmonary Dysplasia. *Clin Perinatol* **46**, (2019).

137. Hellström, A. *et al.* Role of Insulinlike Growth Factor 1 in Fetal Development and in the Early Postnatal Life of Premature Infants. *Am J Perinatol* **33**, (2016).

138. Ley, D. *et al.* rhIGF-1/rhIGFBP-3 in Preterm Infants: A Phase 2 Randomized Controlled Trial. *J Pediatr* **206**, (2019).

139. Green, E. A. *et al.* Anakinra Pilot – a clinical trial to demonstrate safety, feasibility and pharmacokinetics of interleukin 1 receptor antagonist in preterm infants. *Front Immunol* **13**, (2022).

140. Alonso-Ojembarrena, A. *et al.* A phase 1b randomized, multicenter, dose determination trial of zelpultide alfa (recombinant human surfactant protein D) in preterm neonates at high risk of developing bronchopulmonary dysplasia. *Front Pediatr* **13**, (2025).

141. Gilfillan, M. & Bhandari, V. Moving bronchopulmonary dysplasia research from the bedside to the bench. *Am J Physiol Lung Cell Mol Physiol* **322**, (2022).

142. Giusto, K., Wanczyk, H., Jensen, T. & Finck, C. Hyperoxia-induced bronchopulmonary dysplasia: Better models for better therapies. *DMM Dis Model Mech* **14**, (2021).

143. Berger, J. & Bhandari, V. Animal models of bronchopulmonary dysplasia. The term mouse models. *Am J Physiol Lung Cell Mol Physiol* **307**, (2014).

144. O'Reilly, M. & Thébaud, B. Animal models of bronchopulmonary dysplasia. The term rat models. *Am J Physiol Lung Cell Mol Physiol* **307**, (2014).

145. Albertine, K. H. Utility of large-animal models of BPD: chronically ventilated preterm lambs. *Am J Physiol Lung Cell Mol Physiol* **308**, (2015).

146. Yoder, B. A. & Coalson, J. J. Animal models of bronchopulmonary dysplasia. The preterm baboon models. *Am J Physiol Lung Cell Mol Physiol* **307**, (2014).

147. Reyburn, B. *et al.* Nasal ventilation alters mesenchymal cell turnover and improves alveolarization in preterm lambs. *Am J Respir Crit Care Med* **178**, (2008).

148. Thomson, M. A. *et al.* Delayed extubation to nasal continuous positive airway pressure in the immature baboon model of bronchopulmonary dysplasia: Lung clinical and pathological findings. *Pediatrics* **118**, (2006).

149. Richter, J. *et al.* Functional assessment of hyperoxia-induced lung injury after preterm birth in the rabbit. *Am J Physiol Lung Cell Mol Physiol* **306**, (2014).

150. D'Angio, C. T. & Ryan, R. M. Animal models of bronchopulmonary dysplasia. The preterm and term rabbit models. *Am J Physiol Lung Cell Mol Physiol* **307**, (2014).

151. Davis, A. J., Jobe, A. H., Häfner, D. & Ikegami, M. Lung function in premature lambs and rabbits treated with a recombinant SP-C surfactant. *Am J Respir Crit Care Med* **157**, (1998).

152. DiGeronimo, R. J. *et al.* Mechanical ventilation down-regulates surfactant protein A and keratinocyte growth factor expression in premature rabbits. *Pediatr Res* **62**, (2007).

153. Oba, K., Yamashita, H., Waragai, A. & Kawano, T. NF-kappaB in the lungs of premature rabbits during mechanical ventilation - Comparison between conventional mechanical ventilation (CMV) and high-frequency oscillation (HFO). *Pediatr Pulmonol* **42**, (2007).

154. Ahmed, M. N., Codipilly, C., Hogg, N. & Auten, R. L. The protective effect of overexpression of extracellular superoxide dismutase on nitric oxide bioavailability in the lung after exposure to hyperoxia stress. *Exp Lung Res* **37**, (2011).

155. Horowitz, S. *et al.* Changes in gene expression in hyperoxia-induced neonatal lung injury. *Am J Physiol Lung Cell Mol Physiol* **258**, (1990).

156. Polak, M. J., Knight, M. E., Andresen, T. L. & Desena, C. Effects of hyperoxia and beta-adrenergic stimulation on pulmonary surfactant in neonatal rabbits. *Exp Lung Res* **18**, (1992).

157. Sherman, M. P. & Condiotti, R. Hyperoxia damages phagocytic defenses of neonatal rabbit lung. *J Appl Physiol* **62**, (1987).

158. D'Angio, C. T., LoMonaco, M. B., Chaudhry, S. A., Paxhia, A. & Ryan, R. M. Discordant pulmonary proinflammatory cytokine expression during acute hyperoxia in the newborn rabbit. *Exp Lung Res* **25**, (1999).

159. Frank, L. & Ilene Sosenko, R. S. Prenatal development of lung antioxidant enzymes in four species. *J Pediatr* **110**, (1987).

160. Ross, G. F., Ikegami, M., Steinhilber, W. & Jobe, A. H. Surfactant protein C in fetal and ventilated preterm rabbit lungs. *Am J Physiol Lung Cell Mol Physiol* **277**, (1999).

161. Mascaretti, R. S., Mataloun, M. M. G. B., Dolhnikoff, M. & Rebello, C. M. Lung morphometry, collagen and elastin content: Changes after hyperoxic exposure in preterm rabbits. *Clinics* **64**, (2009).

162. Manzano, R. M. *et al.* A hyperoxic lung injury model in premature rabbits: The influence of different gestational ages and oxygen concentrations. *PLoS One* **9**, (2014).

163. Salaets, T. *et al.* Transcriptome analysis of the preterm rabbit lung after seven days of hyperoxic exposure. *PLoS One* **10**, (2015).

164. Jiménez, J. *et al.* Progressive vascular functional and structural damage in a bronchopulmonary dysplasia model in preterm rabbits exposed to hyperoxia. *Int J Mol Sci* **17**, (2016).

165. Mühlfeld, C. *et al.* Design-Based Stereology of the Lung in the Hyperoxic Preterm Rabbit Model of Bronchopulmonary Dysplasia. *Oxid Med Cell Longev* **2021**, (2021).

166. Salaets, T. *et al.* Simvastatin attenuates lung functional and vascular effects of hyperoxia in preterm rabbits. *Pediatr Res* **87**, (2020).

167. Aquila, G. *et al.* Daily Intraperitoneal Administration of Rosiglitazone Does Not Improve Lung Function or Alveolarization in Preterm Rabbits Exposed to Hyperoxia. *Pharmaceutics* **14**, (2022).

168. Rößler, G. *et al.* Prematurity and Hyperoxia Have Different Effects on Alveolar and Microvascular Lung Development in the Rabbit. *J Histochem Cytochem* **71**, (2023).

169. Gie, A. G. *et al.* Intratracheal budesonide/surfactant attenuates hyperoxia-induced lung injury in preterm rabbits. *Am J Physiol Lung Cell Mol Physiol* **319**, (2020).

170. Catozzi, C. *et al.* Single, double, and triple-hit strategies to establish a long-term premature rabbit model of bronchopulmonary dysplasia. *Respir Res* **26**, 35 (2025).

171. Cooney T P & Thurlbeck, W. M. The radial alveolar count method of Emery and Mithal: A reappraisal 2-Intrauterine and early postnatal lung growth. *Thorax* **37**, (1982).

172. Emery, J. L. & Mithal, A. The number of alveoli in the terminal respiratory unit of man during late intrauterine life and childhood. *Arch Dis Child* **35**, (1960).

173. Roubliova, X. I. *et al.* Morphologic changes and methodological issues in the rabbit experimental model for diaphragmatic hernia. *Histol Histopathol* **25**, (2010).

174. Dunnill, M. S. Quantitative methods in the study of pulmonary pathology. *Thorax* **17**, (1962).

175. Salaets, T. *et al.* Local pulmonary drug delivery in the preterm rabbit: Feasibility and efficacy of daily intratracheal injections. *Am J Physiol Lung Cell Mol Physiol* **316**, (2019).

176. Storti, M. *et al.* Time-resolved transcriptomic profiling of the developing rabbit's lungs: impact of premature birth and implications for modelling bronchopulmonary dysplasia. *Respir Res* **24**, (2023).

177. Matute-Bello, G. *et al.* An official american thoracic society workshop report: Features and measurements of experimental acute lung injury in animals. in *Am J Resp Cell Mol Biol* **44**, (2011).

178. Fischer, A. H., Jacobson, K. a, Rose, J. & Zeller, R. Hematoxylin and Eosin (H & E) staining. *CSH Protoc* **2008**, (2005).

179. Salaets, T. *et al.* Preterm birth impairs postnatal lung development in the neonatal rabbit model. *Respir Res* **21**, (2020).

180. Du Plessis, A., Broeckhoven, C., Guelpa, A. & le Roux, S. G. Laboratory x-ray micro-computed tomography: A user guideline for biological samples. *GigaScience* **6**, (2017).

181. Ritman, E. L. Micro-Computed Tomography of the Lungs and Pulmonary-Vascular System. in *Proc Am Thorac Soc* **2**, (2005).

182. Low, F. N. The pulmonary alveolar epithelium of laboratory mammals and man. *Anat Rec* **117**, (1953).

183. Crapo, J. D., Barry, B. E., Gehr, P., Bachofen, M. & Weibel, E. R. Cell number and cell characteristics of the normal human lung. *Am Rev Respir Dis* **126**, (1982).

184. Ochs, M. The closer we look the more we see? quantitative microscopic analysis of the pulmonary surfactant system. *Cell Physiol Biochem* **25**, (2010).

185. Mokhtar, D. M., Hussein, M. T., Hussein, M. M., Abd-Elhafez, E. A. & Kamel, G. New Insight into the Development of the Respiratory Acini in Rabbits: Morphological, Electron Microscopic Studies, and TUNEL Assay. *Microsc Microanal* **25**, (2019).

186. Hristu, R. *et al.* Influence of hematoxylin and eosin staining on the quantitative analysis of second harmonic generation imaging of fixed tissue sections. *Biomed Opt Express* **12**, (2021).

187. Zipfel, W. R. *et al.* Live Tissue Intrinsic Emission Microscopy Using Multiphoton-Excited Native Fluorescence and Second Harmonic Generation. *Proc Natl Acad Sci U S A* **100**, (2003).

188. Benninger, R. K. P. & Piston, D. W. Two-Photon Excitation Microscopy for the Study of Living Cells and Tissues. *Curr Protoc Cell Biol* **59**, (2013).

189. Ávila, F. J., Gambín, A., Artal, P. & Bueno, J. M. In vivo two-photon microscopy of the human eye. *Sci Rep* **9**, (2019).

190. Kröger, M., Schleusener, J., Jung, S. & Darvin, M. E. Characterization of collagen i fiber thickness, density, and orientation in the human skin in vivo using second-harmonic generation imaging. *Photonics* **8**, (2021).

191. Yeh, A. T., Nassif, N., Zoumi, A. & Tromberg, B. J. Selective corneal imaging using combined second-harmonic generation and two-photon excited fluorescence. *Opt Lett* **27**, (2002).

192. Chen, X. *et al.* Prognostic significance of collagen signatures in pancreatic ductal adenocarcinoma obtained from second-harmonic generation imaging. *BMC Cancer* **24**, (2024).

193. Perry, S. W., Burke, R. M. & Brown, E. B. Two-photon and second harmonic microscopy in clinical and translational cancer research. *Ann Biomed Eng* **40**, (2012).

194. Mostaço-Guidolin, L., Rosin, N. L. & Hackett, T. L. Imaging collagen in scar tissue: Developments in second harmonic generation microscopy for biomedical applications. *Int J Mol Sci* **18**, (2017).

195. Ferri, G. *et al.* Metabolic response of Insulinoma 1E cells to glucose stimulation studied by fluorescence lifetime imaging. *FASEB Bioadv* **2**, (2020).

196. Azzarello, F. *et al.* Single-cell imaging of α and β cell metabolic response to glucose in living human Langerhans islets. *Commun Biol* **5**, (2022).

197. Stringari, C. *et al.* Phasor approach to fluorescence lifetime microscopy distinguishes different metabolic states of germ cells in a live tissue. *Proc Natl Acad Sci U S A* **108**, (2011).

198. Skala, M. C. *et al.* In vivo multiphoton microscopy of NADH and FAD redox states, fluorescence lifetimes, and cellular morphology in precancerous epithelia. *Proc Natl Acad Sci U S A* **104**, (2007).

199. Pugliese, L. A. *et al.* Unveiling nanoscale optical signatures of cytokine-induced β-cell dysfunction. *Sci Rep* **13**, (2023).

200. Leben, R., Köhler, M., Radbruch, H., Hauser, A. E. & Niesner, R. A. Systematic enzyme mapping of cellular metabolism by phasor-analyzed label-free NAD(P)H fluorescence lifetime imaging. *Int J Mol Sci* **20**, (2019).

201. Göppert-Mayer, M. Über Elementarakte mit zwei Quantensprüngen. *Ann Phys* **401**, (1931).

202. Kaiser, W. & Garrett, C. G. B. Two-photon excitation in CaF2: Eu2+. *Phys Rev Lett* **7**, (1961).

203. Microscopy, F., Denk, W., Strickler, J. H. & Webb, W. W. Two-Photon Laser Scanning. *New Series* **248**, (1990).

204. Denk, W., Piston, D. W. & Webb, W. W. Two-Photon Molecular Excitation in Laser-Scanning Microscopy. in *Handbook of Biological Confocal Microscopy* (1995).

205. Roth, S. & Freund, I. Optical second-harmonic scattering in rat-tail tendon. *Biopolymers* **20**, (1981).

206. Pena, A. M. *et al.* Three-dimensional investigation and scoring of extracellular matrix remodeling during lung fibrosis using multiphoton microscopy. *Microsc Res Tech* **70**, (2007).

207. Abraham, T. & Hogg, J. Extracellular matrix remodeling of lung alveolar walls in three dimensional space identified using second harmonic generation and multiphoton excitation fluorescence. *J Struct Biol* **171**, (2010).

208. Datta, R., Heaster, T. M., Sharick, J. T., Gillette, A. A. & Skala, M. C. Fluorescence lifetime imaging microscopy: fundamentals and advances in instrumentation, analysis, and applications. *J Biomed Opt* **25**, (2020).

209. Berezin, M. Y. & Achilefu, S. Fluorescence lifetime measurements and biological imaging. *Chem Rev* **110**, (2010).

210. Digman, M. A., Caiolfa, V. R., Zamai, M. & Gratton, E. The phasor approach to fluorescence lifetime imaging analysis. *Biophys J* **94**, (2008).

211. Ranjit, S., Malacrida, L., Jameson, D. M. & Gratton, E. Fit-free analysis of fluorescence lifetime imaging data using the phasor approach. *Nat Protoc* **13**, (2018).

212. Xiao, W., Wang, R. S., Handy, D. E. & Loscalzo, J. NAD(H) and NADP(H) Redox Couples and Cellular Energy Metabolism. *Antioxid Redox Signal* **28**, (2018).

213. Blacker, T. S., Duchen, M. R. & Bain, A. J. NAD(P)H binding configurations revealed by time-resolved fluorescence and two-photon absorption. *Biophys J* **122**, (2023).

214. Blacker, T. S. & Duchen, M. R. Investigating mitochondrial redox state using NADH and NADPH autofluorescence. *Free Radic Biol Med* **100**, (2016).

215. Wang, J. & Dong, W. Oxidative stress and bronchopulmonary dysplasia. *Gene* **678**, (2018).

216. Griffith, B. *et al.* NOX enzymes and pulmonary disease. *Antioxid redox Signal* **11**, (2009).

217. Chance, B. & Thorell, B. Localization and kinetics of reduced pyridine nucleotide in living cells by microfluorometry. *J Biol Chem* **234**, (1959).

218. Chance, B., Cohen, P., Jobsis, F. & Schoener, B. Intracellular Oxidation-Reduction States in Vivo: The microfluorometry of pyridine nucleotide gives a continuous measurement of the oxidation state. *Science (1979)* **137**, (1962).

219. Piston, D. W., Masters, B. R. & Webb, W. W. Three-dimensionally resolved NAD(P)H cellular metabolic redox imaging of the in situ cornea with two-photon excitation laser scanning microscopy. *J Microsc* **178**, (1995).

220. Bennett, B. D., Jetton, T. L., Ying, G., Magnuson, M. A. & Piston, D. W. Quantitative subcellular imaging of glucose metabolism within intact pancreatic islets. *J Biol Chem* **271**, (1996).

221. Bird, D. K. *et al.* Metabolic mapping of MCF10A human breast cells via multiphoton fluorescence lifetime imaging of the coenzyme NADH. *Cancer Res* **65**, (2005).

222. Guo, H.-W. *et al.* Reduced nicotinamide adenine dinucleotide fluorescence lifetime separates human mesenchymal stem cells from differentiated progenies. *J Biomed Opt* **13**, (2008).

223. Stringari, C. *et al.* Metabolic trajectory of cellular differentiation in small intestine by Phasor Fluorescence Lifetime Microscopy of NADH. *Sci Rep* **2**, (2012).

224. Schaefer, P. M., Kalinina, S., Rueck, A., von Arnim, C. A. F. & von Einem, B. NADH Autofluorescence—A Marker on its Way to Boost Bioenergetic Research. *Cytometry A* **95**, (2019).

225. Chance, B., Schoener, B., Oshino, R., Itshak, F. & Nakase, Y. Oxidation-reduction ratio studies of mitochondria in freeze-trapped samples. NADH and flavoprotein fluorescence signals. *J Biol Chem* **254**, (1979).

226. Schindelin, J. *et al.* Fiji: An open-source platform for biological-image analysis. *Nat Methods* **9**, (2012).

227. Huang, L. K. & Wang, M. J. J. Image thresholding by minimizing the measures of fuzziness. *Pattern Recognit* **28**, (1995).

228. Frangi, A. F., Niessen, W. J., Vincken, K. L. & Viergever, M. A. Multiscale vessel enhancement filtering. *Med. Image Comput. Comput. Assist. Interv.* **1496**, (1998).

229. Nejim, Z., Navarro, L., Morin, C. & Badel, P. Quantitative analysis of second harmonic generated images of collagen fibers: a review. *Res Biomed Eng* **39** (2023).

230. Otsu, N. A Threshold Selection Method from Gray-Level Histograms. *IEEE Trans Syst Man Cybern* **9**, (1979).

231. Mižíková, I. *et al.* Collagen and elastin cross-linking is altered during aberrant late lung development associated with hyperoxia. *Am J Physiol Lung Cell Mol Physiol* **308**, (2015).

232. Kumarasamy, A. *et al.* Lysyl oxidase activity is dysregulated during impaired alveolarization of mouse and human lungs. *Am J Respir Crit Care Med* **180**, (2009).

233. Junqueira, L. C. U., Bignolas, G. & Brentani, R. R. Picrosirius staining plus polarization microscopy, a specific method for collagen detection in tissue sections. *Histochem J* **11**, (1979).

234. Dolber, P. C. & Spach, M. S. Conventional and Confocal Fluorescence Microscopy of Collagen Fibers in the Heart. *J Histochem Cytochem.* **41** (1993).

235. Wegner, K. A., Keikhosravi, A., Eliceiri, K. W. & Vezina, C. M. Fluorescence of Picrosirius Red Multiplexed With Immunohistochemistry for the Quantitative Assessment of Collagen in Tissue Sections. *J Histochem Cytochem* **65**, (2017).

236. Pisano, E. D. *et al.* Contrast limited adaptive histogram equalization image processing to improve the detection of simulated spiculations in dense mammograms. *J Digit Imaging* **11**, (1998).

237. Huang, T. S., Yang, G. J. & Tang, G. Y. A Fast Two-Dimensional Median Filtering Algorithm. *IEEE Trans Acoust* **27**, (1979).

238. Alvira, C. M. Aberrant pulmonary vascular growth and remodeling in bronchopulmonary dysplasia. *Front Med* **3**, (2016).

239. Baraldi, E., Carraro, S. & Filippone, M. Bronchopulmonary dysplasia: Definitions and long-term respiratory outcome. *Early Hum Dev* **85**, (2009).

240. Mereness, J. A. & Mariani, T. J. The critical role of collagen VI in lung development and chronic lung disease. *Matrix Biol Plus* **10**, (2021).

241. Thibeault, D. W., Mabry, S. M., Ekekezie, I. I., Zhang, X. & Truog, W. E. Collagen scaffolding during development and its deformation with chronic lung disease. *Pediatrics* **111**, (2003).

242. Datta, R., Alfonso-Garciá, A., Cinco, R. & Gratton, E. Fluorescence lifetime imaging of endogenous biomarker of oxidative stress. *Sci Rep* **5**, (2015).

243. Da Silva, F. A. B., Racanelli, A. P., Lorand-Metze, I. & Metze, K. Fluorescence lifetime imaging is able to recognize different hematopoietic precursors in unstained routine bone marrow films. *Cytometry A* **99**, (2021).

244. Markus, M. A., Ferrari, D. P., Alves, F. & Ramos-Gomes, F. Effect of tissue fixation on the optical properties of structural components assessed by non-linear microscopy imaging. *Biomed Opt Express* **14**, (2023).

245. Sánchez-Hernández, A., Polleys, C. M. & Georgakoudi, I. Formalin fixation and paraffin embedding interfere with the preservation of optical metabolic assessments based on endogenous NAD(P)H and FAD two-photon excited fluorescence. *Biomed Opt Express* **14**, (2023).